

Twist-Programmable Superconductivity in Spin-Orbit Coupled Bilayer Graphene

Yiran Zhang^{1,2,3†}, Gal Shavit^{2,3,4}, Huiyang Ma^{5,6}, Youngjoon Han^{2,3}, Chi Wang Siu^{1,2}, Ankan Mukherjee^{1,2}, Kenji Watanabe⁷, Takashi Taniguchi⁷, David Hsieh^{2,3}, Cyprian Lewandowski^{5,6}, Felix von Oppen⁸, Yuval Oreg⁹, and Stevan Nadj-Perge^{1,2†}

¹*T. J. Watson Laboratory of Applied Physics, California Institute of Technology, 1200 East California Boulevard, Pasadena, California 91125, USA*

²*Institute for Quantum Information and Matter, California Institute of Technology, Pasadena, California 91125, USA*

³*Department of Physics, California Institute of Technology, Pasadena, California 91125, USA*

⁴*Walter Burke Institute of Theoretical Physics, California Institute of Technology, Pasadena, California 91125, USA*

⁵*National High Magnetic Field Laboratory, Tallahassee, FL, USA*

⁶*Department of Physics, Florida State University, Tallahassee, FL, USA*

⁷*National Institute for Materials Science, Namiki 1-1, Tsukuba, Ibaraki 305 0044, Japan*

⁸*Dahlem Center for Complex Quantum Systems and Fachbereich Physik, Freie Universität Berlin, 14195 Berlin, Germany*

⁹*Department of Condensed Matter Physics, Weizmann Institute of Science, Rehovot, Israel*

[†]*Correspondence: yzhang7@caltech.edu; s.nadj-perge@caltech.edu*

The relative twist angle between layers of near-lattice-matched van der Waals materials is critical for the emergent phenomena associated with moiré flat bands¹⁻³. However, the concept of angle rotation control is not exclusive to moiré superlattices in which electrons directly experience a twist-angle-dependent periodic potential. Instead, it can also be employed to induce programmable symmetry-breaking perturbations with the goal of stabilizing desired correlated states. Here, we experimentally demonstrate ‘moiréless’ twist-tuning of superconductivity together with other correlated orders in Bernal bilayer graphene proximitized by tungsten diselenide. The precise alignment between the two materials systematically controls the strength of induced Ising spin-orbit coupling (SOC), profoundly altering the phase diagram. As Ising SOC is increased, superconductivity onsets at a higher displacement field and features a higher critical temperature, reaching up to 0.5 K. Within the main superconducting dome and in the strong Ising SOC limit, we find an unusual phase transition characterized by a nematic redistribution of holes among trigonally warped Fermi pockets and enhanced resilience to in-plane magnetic fields. The superconducting behavior is theoretically compatible with the prominent role of interband interactions between symmetry-breaking Fermi pockets. Moreover, we identify two additional superconducting regions, one of which descends from an inter-valley coherent normal state and exhibits a Pauli-limit violation ratio exceeding 40, among the highest for all known superconductors⁴⁻⁷. Our results provide essential insights into ultra-clean graphene superconductors and underscore the potential of utilizing moiréless-twist engineering across a wide range of van der Waals heterostructures.

In a large electrical displacement field, the electronic bands of Bernal bilayer graphene (BLG) flatten out around the corners of the Brillouin zone, giving rise to various correlated phases that spontaneously break BLG symmetries^{4,8,9}. These correlated phases naturally compete with each other and, therefore, are highly sensitive to explicit symmetry-breaking perturbations. One way to induce such perturbations is by placing BLG adjacent to transition metal dichalcogenides such as tungsten diselenide (WSe₂). The SOC perturbations induced by WSe₂^{10–16} alter the phase diagram, remarkably enabling the superconductivity in BLG⁴ to appear at zero magnetic field and boosting the critical temperature significantly^{17–19}. However, the nature and the extent of this enhancement, and more generally, the impact of SOC on the correlated phases of BLG and related graphene systems, remain elusive.

Theoretically, the induced SOC is predicted to depend on the relative twist angle θ between WSe₂ and graphene^{16,20–23} (Fig. 1a). This dependence, however, has not been experimentally studied or utilized with systematic control. Here we employ this novel tuning knob to explore how Ising SOC modifies the correlated phases and emerging superconductivity in BLG. This approach offers several unique opportunities: (i) the strength of the induced Ising SOC in BLG can be precisely quantified; (ii) the induced SOC is much less sensitive to twist-angle variations, allowing for fine control; and (iii) the proximity to WSe₂ does not induce additional disorder, promoting reproducibility. We investigated a series of BLG-WSe₂ devices (Fig. 1b) fabricated from the same BLG and WSe₂ crystals, separating the large BLG flake into multiple pieces²⁴. With the first BLG piece roughly lattice-aligned with WSe₂ ($\theta \approx 0^\circ$), the following ones are sequentially twisted relative to WSe₂ with a $\sim 6^\circ$ increment (see Methods and Extended Data Fig. 1 for device fabrication).

To characterize the SOC in our devices, we first perform high-resolution measurements of Shubnikov–de Haas oscillations (Fig. 1f,g) in regions of the n - D phase diagram (n is the doping density, D is the electrical displacement field) that are well-described by non-interacting theory (Supplementary Information (SI), section 2). When a positive D field $D/\epsilon_0 = 0.2$ V/nm is applied, the hole-carrier wavefunctions are strongly polarized towards the top graphene layer adjacent to WSe₂, which in turn induces Ising SOC in BLG^{14,17–19,25,26} (see Methods and Extended Data Fig. 2 for further discussion). In this regime, we observe a clear beating pattern in longitudinal resistance R_{xx} as a function of out-of-plane magnetic field (B_\perp) at higher doping densities (Fig. 1f), indicating two close oscillation frequencies originating from Fermi pockets of slightly different sizes. The Fermi-surface imbalance is revealed by normalizing the oscillation frequencies of $R_{xx}(1/B_\perp)$ to the Luttinger volume corresponding to the total doping density. The resulting normalized frequency f_ν reveals the fraction of the total Fermi surface area enclosed by a cyclotron orbit. Figure 1h,i shows a comparison of the density-dependent frequencies f_ν from two devices with twist angles $\theta \approx 0^\circ$ and 30° , respectively. In both cases, two frequencies, $f_\nu^{(1)}$ and $f_\nu^{(2)}$, are found satisfying $f_\nu^{(1)} + f_\nu^{(2)} = 1/2$. These frequencies can be understood as a splitting from $f_\nu = 1/4$, which signals the broken four-fold spin-valley symmetry (Fig. 1c,d): Ising SOC separates two pairs of spin-valley locked bands with slightly different Fermi-surface areas (schematics in Fig. 1h,i).

The induced Ising SOC is modulated by the twist angle θ between WSe₂ and BLG. This is evident

from the more pronounced splitting shown in Fig. 1h compared to the one in Fig. 1i. By extracting the sizes of the Fermi pockets corresponding to spin-valley locked bands (see Methods and Extended Data Fig. 2) and comparing them to band-structure calculations, we precisely quantify the Ising SOC strength, $|\lambda_I| \approx 1.6$ meV and 0.4 meV in Fig. 1h,i, respectively. Fig. 1e summarizes systematic measurements across three sets of moiréless twisting BLG-WSe₂ devices (D1-D3; see Methods and SI Fig. 1 to 3), all of which demonstrate robust θ -modulated Ising SOC strengths. Our results are consistent with the picture that virtual interlayer tunneling is responsible for the induced SOC. When the lattices of BLG and WSe₂ are angle-aligned, i.e., $\theta \approx 0^\circ$, the K/K' valleys of BLG couple more effectively to one of the two valleys of WSe₂ (left schematic in Fig. 1e), resulting in a large induced Ising SOC. In contrast, for $\theta \approx 30^\circ$, the inter-valley and intra-valley tunneling between WSe₂ and BLG have the same amplitude due to reflection symmetry (right schematic in Fig. 1e). The induced Ising SOC in BLG vanishes accordingly²⁷. The overall θ dependence and the magnitude of Ising SOC are qualitatively consistent with predictions^{16,20–23}.

Using the exquisite twist-angle control of the Ising SOC strength, we explore the SOC-dependent correlated phase diagrams at large D fields. Devices with various Ising strengths all show characteristic R_{xx} features that are associated with strong correlations and superconductivity stabilized at zero magnetic field^{17–19} (Fig. 2a-d, see Extended Data Fig. 3 for all the n - D phase diagrams). Importantly, the main superconducting pocket, which emerges from a polarized state with a dominant population of two out of the four spin-valley flavors^{17,18}, shows a strong dependence on the strength of Ising SOC. For low Ising SOC ($|\lambda_I| \approx 0.4$ meV; Fig. 2a), the superconducting region occupies a large D field range, starting from $D/\epsilon_0 \approx 0.3$ V/nm and extending up to $D/\epsilon_0 \approx 1.25$ V/nm. For large Ising SOC ($|\lambda_I| \approx 1.5$ meV; Fig. 2d), however, superconductivity onsets only at $D/\epsilon_0 \approx 0.9$ V/nm. Overall, the value D_{onset} marking the onset of the superconducting pocket grows with increasing $|\lambda_I|$ (Fig. 2e).

The observed trend of D_{onset} can be understood in a simple model invoking the *interband* interactions between the majority ($K \uparrow$, $K' \downarrow$) and the minority ($K \downarrow$, $K' \uparrow$) spin-valley flavors; see Fig. 2g,h. Irrespective of the pairing mechanism, superconductivity requires an attractive interaction to overcome the renormalized Coulomb repulsion^{28,29}, commonly quantified by Tolmachev-Anderson-Morel (TAM) pseudopotential^{30,31} μ^* . When μ^* is large, electrons do not form pairs and superconductivity vanishes. The generalized multiband value, which takes into account majority and minority spin-valley flavors, μ_{multi}^* (see Methods and SI, section 3 to 5) is plotted in Fig. 2h for two values of Ising SOC. Remarkably, μ_{multi}^* grows with increasing $|\lambda_I|$ and decreases at higher D fields. Thus, the threshold for superconductivity, as implied by a sufficiently weak μ_{multi}^* , aligns with the experimental D_{onset} trend. The connection between μ_{multi}^* and Ising SOC arises due to interband interactions. These interactions allow scattering of pairs between majority and minority bands (Fig. 2g), greatly enhancing screening of the bare repulsion as compared to the band-decoupled case. A larger density imbalance between the bands, as dictated by stronger Ising SOC, shrinks the phase space where *both bands* have large density of states (DOS) near the Fermi level (right schematic in Fig. 2h). Consequently, the interband interactions are suppressed, μ_{multi}^* grows, and superconductivity diminishes.

Intriguingly, the superconducting critical temperature T_c also shows a striking dependence on $|\lambda_I|$. While D_{onset} is smaller and superconductivity persists over a wide range of D fields for small Ising SOC, the critical temperature remains low throughout and saturates at $T_c \approx 150$ mK (Fig. 2i,j). In contrast, for large Ising SOC, superconductivity onsets only at higher D fields, but T_c quickly increases, reaching $T_c \approx 500$ mK at the optimal D (Fig. 2l,m). This is the highest T_c reported for crystalline (untwisted) graphene systems. Thus, the optimal critical temperature also shows an increasing trend with $|\lambda_I|$ (Fig. 2f; see SI Fig. 4 for $|\lambda_I| \approx 0$ meV). A detailed three-dimensional map of the optimal critical temperature T_c^{optimal} versus D field and $|\lambda_I|$ is plotted in Fig. 2k. These observations motivate further investigations of BLG with even stronger Ising SOC^{32,33}.

Devices with large Ising SOC further reveal two additional superconducting pockets (1.4 meV $\lesssim |\lambda_I| \lesssim 1.6$ meV; see Fig. 3a, Fig. 2c,d, and Extended Data Fig. 3). We refer to the observed superconducting regions as SC_1 , SC_2 , and SC_3 , enumerated from higher to lower hole doping, respectively (with the main superconducting region being SC_2 ; see Extended Data Fig. 4 and SI, section 1 for additional characterizations and discussion). Each superconducting pocket descends from a distinct flavor-symmetry-breaking normal state (Fig. 3b-f) and is terminated by a first-order phase transition (marked by black dashed lines) on the low-doping side. Regions SC_1 , SC_2 , and SC_3 feature optimal critical temperatures $T_c \approx 60$ mK, 500 mK, and 100 mK, respectively (Fig. 3b and Fig. 3d insets). The normal state of SC_1 can be directly related to the non-interacting band structure. Quantum oscillations in this regime ($-9 \lesssim n \lesssim -7.6 \times 10^{11} \text{ cm}^{-2}$, Fig. 3c) show two main frequencies (marked by blue and orange arrows) obeying $2 \cdot f_\nu^{(1)} + 6 \cdot f_\nu^{(2)} \approx 1$. This indicates two Ising-majority Fermi pockets and six Ising-minority trigonal-warping pockets^{18,34} (Fig. 3c left schematic); we denote the flavor-polarized phase as $\text{FP}(2, 6)$ ($\text{FP}(n, m)$ denotes a flavor-polarized phase with n and m degenerate-sized Fermi pockets, from large to small).

Ultrahigh-resolution quantum oscillations reveal the unusual Fermi surfaces in the correlated normal states forming SC_2 and SC_3 . At higher doping of SC_2 ($n \lesssim -8.25 \times 10^{11} \text{ cm}^{-2}$, Fig. 3e), two dominant oscillation frequencies, marked by blue ($f_\nu^{(1)}$) and orange ($f_\nu^{(2)}$) lines in Fig. 3f, satisfy $2 \cdot f_\nu^{(1)} + 4 \cdot f_\nu^{(2)} \approx 1$ (black line). Thus, the flavor-polarized phase hosts two majority and four minority Fermi pockets, denoted as $\text{FP}(2, 4)$. The occupation of two out of the three trigonal-warping pockets for each minority flavor implies a nematic normal state that breaks the C_3 rotational symmetry¹⁸ (Fig. 3f left schematic). Remarkably, we observe a different Fermi-pocket configuration within the same superconducting pocket at $-8.25 \lesssim n \lesssim -7.1 \times 10^{11} \text{ cm}^{-2}$. The lowest third frequency $f_\nu^{(3)}$ is clearly resolved (green line in Fig. 3f; see Methods and Extended Data Fig. 5 to 7). The value of $f_\nu^{(3)}$ rapidly decreases to zero at the low-doping phase boundary, implying that two out of the four minority Fermi pockets shrink considerably in this density range. We denote this phase as $\text{FP}(2, 2, 2)$ given the relation $2 \cdot f_\nu^{(1)} + 2 \cdot f_\nu^{(2)} + 2 \cdot f_\nu^{(3)} \approx 1$. Here, the second and the third 2 imply an additional broken symmetry within the trigonal-warping pockets^{35,36} (orange and green pockets of the middle schematic in Fig. 3f), signaling a nematic redistribution of holes. This continuous transition from $\text{FP}(2, 2, 2)$ to $\text{FP}(2, 4)$ has a significant impact on the in-plane magnetic field response of SC_2 (see Fig. 4).

An exceptional correlated phase denoted FP(1, 3, 1) emerges upon further decreasing the doping ($-7.1 \lesssim n \lesssim -5.7 \times 10^{11} \text{ cm}^{-2}$; Fig. 3e,f). The three Fermi-surface frequencies obey $f_\nu^{(4)} + 3 \cdot f_\nu^{(5)} + f_\nu^{(6)} \approx 1$, with $f_\nu^{(4)}$ being larger than 1/2, ensuring that the largest Fermi pocket is non-degenerate (Methods and Extended Data Fig. 8 to 10). Remarkably, this normal state supports SC₃, although all Fermi pockets have odd multiplicities. The combination of superconductivity and odd multiplicities strongly points at an inter-valley coherent (IVC) state^{37–43} (purple schematic of Fig. 3f). This is further corroborated by the B_\perp -field response of the phase boundaries³⁹ (Methods and Extended Data Fig. 11). The odd multiplicity of all Fermi pockets excludes the possibility of conventional s -wave pairing, suggesting unconventional superconductivity. Moreover, provided that the pockets are intrinsically superconducting, the number of three mid-size Fermi pockets ($f_\nu^{(5)}$) implies time-reversal symmetry breaking regardless of the IVC nature^{41,44–46}. Alternative exotic scenarios are not precluded, e.g., the valleys of FP(1, 3, 1) could still enjoy independence, in which case, the resulting superconductivity would strongly break time-reversal symmetry, promoting chiral finite-momentum pairing.

All three superconducting pockets show extraordinary resilience to in-plane magnetic field B_\parallel . SC₁ has a critical field $B_{c\parallel} \approx 2.5$ T, significantly higher than observed previously¹⁸ (Extended Data Fig. 12). SC₂ and SC₃ show distinct B_\parallel response, reflecting the highly unusual intertwining with the underlying normal states. Fig. 4a,b shows the dependence of R_{xx} on B_\parallel (Fig. 4a) and temperature (Fig. 4b). SC₂ occupies a significantly larger doping range, and its optimal T_c is roughly five times that of SC₃. In comparison, the two superconducting regions show a striking response to B_\parallel . While SC₂ is fully suppressed by $B_\parallel \approx 3$ T, SC₃ persists up to $B_\parallel = 7$ T at the phase boundary. Crucially, the T_c^{optimal} of SC₃ appears to be insensitive to B_\parallel (Fig. 4e and Extended Data Fig. 13), with the superconducting domes at $B_\parallel = 0$ T and 3 T being almost the same (Fig. 4c,d). The Pauli limit B_p is related to the zero-magnetic-field critical temperature $T_c(0)$ as $B_p = 1.86 \text{ T/K} \times T_c(0)$. $T_c(0) = 100$ mK for SC₃ would produce $B_p = 0.186$ T. Thus, the observed $B_{c\parallel} = 7$ T yields a Pauli-limit violation ratio (PVR) $B_{c\parallel}/B_p \sim 40$, placing SC₃ among the superconducting phases with the highest PVR^{4–7}. Note that the exceedingly large PVR only presents in SC₃ with odd Fermi-pocket multiplicities, further reflecting its remarkable nature.

While having a significantly lower PVR, SC₂ features two doping regions with distinct B_\parallel responses (Fig. 4f,g) that are directly intertwined with the continuous transition from FP(2, 2, 2) to FP(2, 4) (Fig. 4h,i). Figure 4f,g shows representative R_{xx} versus temperature and B_\parallel measured in the overdoped and underdoped regions ($n = -8.5$ and $-6.9 \times 10^{11} \text{ cm}^{-2}$, respectively) for $D/\epsilon_0 = 1.2 \text{ V/nm}$. SC₂ exhibits the same $T_c(0) \approx 200$ mK at both doping densities, but the B_\parallel responses are distinct. The overdoped T_c is quickly suppressed by B_\parallel following a conventional quadratic scaling (Fig. 4f). The underdoped T_c , however, is insensitive to B_\parallel for $B_\parallel \leq 1$ T (Fig. 4g), with the depairing at $B_\parallel > 1.5$ T likely due to the Fermi-surface changes induced by B_\parallel .

We fit T_c versus B_\parallel by $T_c(B_\parallel) = T_c(0) - \alpha \cdot B_\parallel^2$, where α quantifies the pair-breaking tendency of B_\parallel . The resulting α shows a striking dependence on doping (Fig. 4h). At higher doping, α plateaus around 0.08 K/T^2 ; at lower doping, α approaches zero, indicating vanishing sensitivity

to B_{\parallel} . Importantly, the qualitative change in α (Fig. 4h) coincides with the redistribution of the trigonal-warped pockets (Fig. 4i). The region with the plateau ($-8.8 \lesssim n \lesssim -7.3 \times 10^{11} \text{ cm}^{-2}$) and the region with the rapidly changing α ($-7.3 \lesssim n \lesssim -6.6 \times 10^{11} \text{ cm}^{-2}$) correspond to the FP(2, 4) and FP(2, 2, 2) phases, respectively. Within the FP(2, 2, 2), both the value of α and the size of the smallest Fermi pockets (green pockets in Fig. 4h) approach zero at the phase boundary ($n \approx -6.6 \times 10^{11} \text{ cm}^{-2}$). These observations suggest that the smallest Fermi pockets determine the B_{\parallel} response (see also Extended Data Fig. 14 to 16).

The disparity in the B_{\parallel} response of the two SC₂ regions may also be attributed to the prominence of majority-minority interband interactions, so that the B_{\parallel} response (Fig. 4f-i) and the observed D_{onset} trend (Fig. 2e) share a common microscopic origin (SI, section 7). The magnetic field causes majority- (minority-) band spins cant towards (away from) the magnetic field direction^{41,47}. As a consequence, Cooper pair scattering between the bands is suppressed, and the applied B_{\parallel} leads to an appreciable decrease in T_c (Fig. 4j,l). Conversely, if minority bands become valley polarized (consistent with FP(2, 2, 2), right schematic in Fig. 4k), one expects the adverse magnetic field effects on the interband interaction to gradually disappear, making the superconductor less field-sensitive (Fig. 4k,m). This coincides with the experimental trend in Fig. 4f-i. The above mechanism is consistent with the PVR hierarchy of SC₁, SC₂, and SC₃ (SI, section 7). The conventional depairing mechanisms within the Ising superconductor framework^{17,48–50}, however, is qualitatively inconsistent with our observations (Methods and SI, section 8).

Unprecedented control over the strength of Ising SOC in BLG allowed us to explore its rich set of superconducting regions systematically. Superconductivity occurs for a diverse set of Fermi-pocket configurations, including for Fermi pockets with odd multiplicity pointing at unconventional superconductivity. Remarkably, all the superconductors exhibit distinctive resilience to in-plane magnetic field. A newly discovered IVC configuration exhibits one of the highest PVR values for any superconductor to date. More generally, the approach of inducing tunable symmetry-breaking fields via moiréless-twisting, can be applied to a broad family of van der Waals materials and extended beyond SOC to include magnetism, charge orders, etc. This opens promising avenues towards tailoring exotic phases of matter on demand.

References:

1. Bistritzer, R. & MacDonald, A. H. Moiré bands in twisted double-layer graphene. *PNAS* **108**, 12233–12237 (2011).
2. Cao, Y. *et al.* Correlated insulator behaviour at half-filling in magic-angle graphene superlattices. *Nature* **556**, 80–84 (2018).
3. Cao, Y. *et al.* Unconventional superconductivity in magic-angle graphene superlattices. *Nature* **556**, 43–50 (2018).

4. Zhou, H. *et al.* Isospin magnetism and spin-polarized superconductivity in Bernal bilayer graphene. *Science* **375**, 774–778 (2022).
5. Ran, S. *et al.* Extreme magnetic field-boosted superconductivity. *Nat. Phys.* **15**, 1250–1254 (2019).
6. Ran, S. *et al.* Nearly ferromagnetic spin-triplet superconductivity. *Science* **365**, 684–687 (2019).
7. Lu, J. *et al.* Full superconducting dome of strong Ising protection in gated monolayer WS₂. *Proceedings of the National Academy of Sciences* **115**, 3551–3556 (2018).
8. de la Barrera, S. C. *et al.* Cascade of isospin phase transitions in Bernal-stacked bilayer graphene at zero magnetic field. *Nat. Phys.* **18**, 771–775 (2022).
9. Seiler, A. M. *et al.* Quantum cascade of correlated phases in trigonally warped bilayer graphene. *Nature* **608**, 298–302 (2022).
10. Wang, Z. *et al.* Origin and magnitude of ‘designer’ spin-orbit interaction in graphene on semiconducting transition metal dichalcogenides. *Phys. Rev. X* **6**, 041020 (2016).
11. Gmitra, M. & Fabian, J. Proximity effects in bilayer graphene on monolayer WSe₂: Field-effect spin valley locking, spin-orbit valve, and spin transistor. *Phys. Rev. Lett.* **119**, 146401 (2017).
12. Khoo, J. Y., Morpurgo, A. F. & Levitov, L. On-demand spin–orbit interaction from which-layer tunability in bilayer graphene. *Nano Lett.* **17**, 7003–7008 (2017).
13. Khoo, J. Y. & Levitov, L. Tunable quantum Hall edge conduction in bilayer graphene through spin-orbit interaction. *Phys. Rev. B* **98**, 115307 (2018).
14. Island, J. O. *et al.* Spin–orbit-driven band inversion in bilayer graphene by the van der Waals proximity effect. *Nature* **571**, 85–89 (2019).
15. Wang, D. *et al.* Quantum Hall effect measurement of spin–orbit coupling strengths in ultra-clean bilayer graphene/WSe₂ heterostructures. *Nano Lett.* **19**, 7028–7034 (2019).
16. Li, Y. & Koshino, M. Twist-angle dependence of the proximity spin-orbit coupling in graphene on transition-metal dichalcogenides. *Phys. Rev. B* **99**, 075438 (2019).
17. Zhang, Y. *et al.* Enhanced superconductivity in spin–orbit proximitized bilayer graphene. *Nature* **613**, 268–273 (2023).
18. Holleis, L. *et al.* Nematicity and Orbital Depairing in Superconducting Bernal Bilayer Graphene with Strong Spin Orbit Coupling. *arXiv:2303.00742 [cond-mat]* (2024). [2303.00742](https://arxiv.org/abs/2303.00742).

19. Li, C. *et al.* Tunable superconductivity in electron- and hole-doped Bernal bilayer graphene. *Nature* 1–7 (2024).
20. Chou, Y.-Z., Wu, F. & Das Sarma, S. Enhanced superconductivity through virtual tunneling in Bernal bilayer graphene coupled to WSe_2 . *Phys. Rev. B* **106**, L180502 (2022).
21. David, A., Rakytá, P., Kormányos, A. & Burkard, G. Induced spin-orbit coupling in twisted graphene–transition metal dichalcogenide heterobilayers: Twistronics meets spintronics. *Phys. Rev. B* **100**, 085412 (2019).
22. Naimer, T., Zollner, K., Gmitra, M. & Fabian, J. Twist-angle dependent proximity induced spin-orbit coupling in graphene/transition metal dichalcogenide heterostructures. *Phys. Rev. B* **104**, 195156 (2021).
23. Zollner, K., João, S. M., Nikolić, B. K. & Fabian, J. Twist- and gate-tunable proximity spin-orbit coupling, spin relaxation anisotropy, and charge-to-spin conversion in heterostructures of graphene and transition metal dichalcogenides. *Phys. Rev. B* **108**, 235166 (2023).
24. Li, H. *et al.* Electrode-Free Anodic Oxidation Nanolithography of Low-Dimensional Materials. *Nano Lett.* **18**, 8011–8015 (2018).
25. Masseroni, M. *et al.* Spin-orbit proximity in MoS_2 /bilayer graphene heterostructures. *arXiv:2403.17120 [cond-mat]* (2024). [2403.17120](#).
26. Seiler, A. M. *et al.* Layer-selective spin-orbit coupling and strong correlation in bilayer graphene. *arXiv:2403.17140 [cond-mat]* (2024). [2403.17140](#).
27. Sun, L. *et al.* Determining spin-orbit coupling in graphene by quasiparticle interference imaging. *Nat Commun* **14**, 3771 (2023).
28. McMillan, W. L. Transition temperature of strong-coupled superconductors. *Phys. Rev.* **167**, 331–344 (1968). URL <https://link.aps.org/doi/10.1103/PhysRev.167.331>.
29. Allen, P. B. & Dynes, R. C. Transition temperature of strong-coupled superconductors re-analyzed. *Phys. Rev. B* **12**, 905–922 (1975). URL <https://link.aps.org/doi/10.1103/PhysRevB.12.905>.
30. Tolmachev, V. V. Logarithmic criterion for superconductivity. *SPhD* **6**, 800 (1962).
31. Morel, P. & Anderson, P. W. Calculation of the Superconducting State Parameters with Retarded Electron-Phonon Interaction. *Phys. Rev.* **125**, 1263–1271 (1962).
32. Yankowitz, M. *et al.* Tuning superconductivity in twisted bilayer graphene. *Science* **363**, 1059–1064 (2019).

33. Kedves, M. *et al.* Stabilizing the Inverted Phase of a WSe₂/BLG/WSe₂ Heterostructure via Hydrostatic Pressure. *Nano Lett.* **23**, 9508–9514 (2023).
34. McCann, E. & Koshino, M. The electronic properties of bilayer graphene. *Rep. Prog. Phys.* **76**, 056503 (2013).
35. Dong, Z., Davydova, M., Ogunnaike, O. & Levitov, L. Isospin- and momentum-polarized orders in bilayer graphene. *Phys. Rev. B* **107**, 075108 (2023).
36. Lin, J.-X. *et al.* Spontaneous momentum polarization and diodicity in Bernal bilayer graphene. *arXiv:2302.04261 [cond-mat]* (2023). [2302.04261](#).
37. Nuckolls, K. P. *et al.* Quantum textures of the many-body wavefunctions in magic-angle graphene. *Nature* **620**, 525–532 (2023).
38. Kim, H. *et al.* Imaging inter-valley coherent order in magic-angle twisted trilayer graphene. *Nature* **623**, 942–948 (2023).
39. Arp, T. *et al.* Intervalley coherence and intrinsic spin–orbit coupling in rhombohedral trilayer graphene. *Nat. Phys.* 1–8 (2024).
40. Chatterjee, S., Wang, T., Berg, E. & Zaletel, M. P. Inter-valley coherent order and isospin fluctuation mediated superconductivity in rhombohedral trilayer graphene. *Nat Commun* **13**, 6013 (2022).
41. Koh, J. M., Thomson, A., Alicea, J. & Lantagne-Hurtubise, É. Symmetry-broken metallic orders in spin-orbit-coupled Bernal bilayer graphene. *arXiv:2407.09612 [cond-mat]* (2024). [2407.09612](#).
42. You, Y.-Z. & Vishwanath, A. Kohn-Luttinger superconductivity and intervalley coherence in rhombohedral trilayer graphene. *Phys. Rev. B* **105**, 134524 (2022).
43. Xie, M. & Das Sarma, S. Flavor symmetry breaking in spin-orbit coupled bilayer graphene. *Phys. Rev. B* **107**, L201119 (2023).
44. Thomson, A., Sorensen, I. M., Nadj-Perge, S. & Alicea, J. Gate-defined wires in twisted bilayer graphene: From electrical detection of intervalley coherence to internally engineered Majorana modes. *Phys. Rev. B* **105**, L081405 (2022).
45. Koh, J. M., Alicea, J. & Lantagne-Hurtubise, É. Correlated phases in spin-orbit-coupled rhombohedral trilayer graphene. *Phys. Rev. B* **109**, 035113 (2024).
46. Zhumagulov, Y., Kochan, D. & Fabian, J. Swapping exchange and spin-orbit induced correlated phases in proximitized Bernal bilayer graphene. *Phys. Rev. B* **110**, 045427 (2024).
47. Dong, Z., Lantagne-Hurtubise, É. & Alicea, J. Superconductivity from spin-canting fluctuations in rhombohedral graphene. *arXiv:2406.17036 [cond-mat]* (2024). [2406.17036](#).

48. Frigeri, P. A., Agterberg, D. F., Koga, A. & Sigrist, M. Superconductivity without Inversion Symmetry: MnSi versus CePt₃Si. *Phys. Rev. Lett.* **92**, 097001 (2004).
49. Lu, J. M. *et al.* Evidence for two-dimensional ising superconductivity in gated MoS₂. *Science* **350**, 1353–1357 (2015).
50. Saito, Y. *et al.* Superconductivity protected by spin-valley locking in ion-gated MoS₂. *Nat Phys* **12**, 144–149 (2016).
51. Seyler, K. L. *et al.* Electrical control of second-harmonic generation in a WSe₂ monolayer transistor. *Nature Nanotech* **10**, 407–411 (2015).
52. Szentpéteri, B. *et al.* Tuning the proximity induced spin-orbit coupling in bilayer graphene/WSe₂ heterostructures with pressure. *ArXiv e-prints* 2409.20062 (2024).
53. Cohen, M. H. & Falicov, L. M. Magnetic Breakdown in Crystals. *Phys. Rev. Lett.* **7**, 231–233 (1961).
54. Jung, J. & MacDonald, A. H. Accurate tight-binding models for the π bands of bilayer graphene. *Phys. Rev. B* **89**, 035405 (2014).
55. Gmitra, M., Kochan, D., Högl, P. & Fabian, J. Trivial and inverted Dirac bands and the emergence of quantum spin Hall states in graphene on transition-metal dichalcogenides. *Phys. Rev. B* **93**, 155104 (2016).
56. Zaletel, M. P. & Khoo, J. Y. The gate-tunable strong and fragile topology of multilayer-graphene on a transition metal dichalcogenide. *arXiv:1901.01294 [cond-mat]* (2019). [1901.01294](#).
57. Shavit, G. & Oreg, Y. Inducing superconductivity in bilayer graphene by alleviation of the Stoner blockade. *Phys. Rev. B* **108**, 024510 (2023).
58. Nagaosa, N. *Quantum Field Theory in Condensed Matter Physics* (Springer, Berlin, Heidelberg, 1999).
59. Chou, Y.-Z., Wu, F., Sau, J. D. & Das Sarma, S. Acoustic-phonon-mediated superconductivity in Bernal bilayer graphene. *Phys. Rev. B* **105**, L100503 (2022).
60. Lian, B., Wang, Z. & Bernevig, B. A. Twisted Bilayer Graphene: A Phonon-Driven Superconductor. *Phys. Rev. Lett.* **122**, 257002 (2019).
61. Kheirabadi, N., McCann, E. & Fal'ko, V. I. Magnetic ratchet effect in bilayer graphene. *Phys. Rev. B* **94**, 165404 (2016).
62. Ma, H., Chichinadze, D. V. & Lewandowski, C. Upper critical in-plane magnetic field in quasi-2D layered superconductors. *In preparation*. (2024).

63. Saint-James, D., Sarma, G., Thomas, E. J. & Silverman, P. *Type II Superconductivity* (Oxford, New York, Pergamon Press, 1969).
64. Zwicknagl, G., Jahns, S. & Fulde, P. Critical Magnetic Field of Ultra-Thin Superconducting Films and Interfaces. *J. Phys. Soc. Jpn.* **86**, 083701 (2017).
65. Zhang, Y. *et al.* Direct observation of a widely tunable bandgap in bilayer graphene. *Nature* **459**, 820–823 (2009).

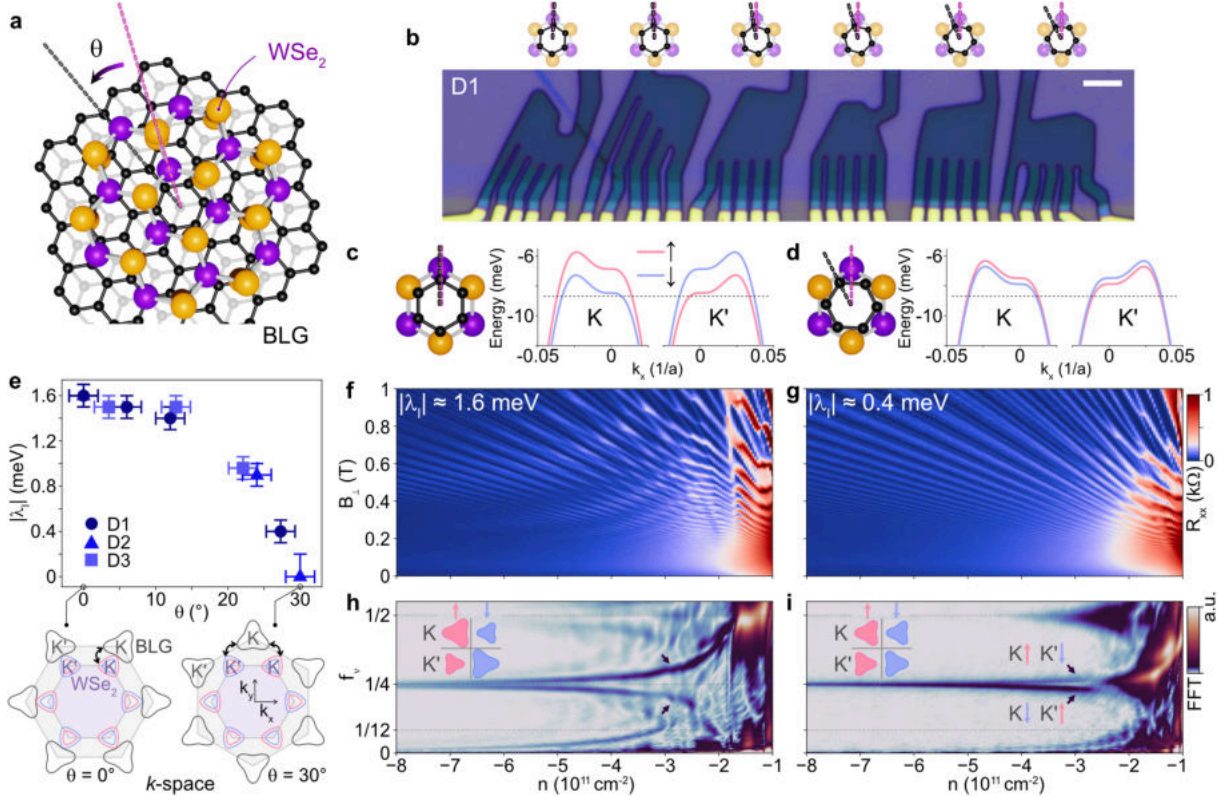


Figure 1 | Programmable Ising SOC by interfacial twisting between BLG and WSe₂. **a**, Schematic showing the twisting of the BLG-WSe₂ interface. **b**, Optical image of the device set D1. Crystal axes of graphene and WSe₂ are rotated relative to each other with angles $\theta \sim 0^\circ$, 6° , 12° , 18° , 24° , and 30° for the six devices, respectively. The scale bar corresponds to $5\mu\text{m}$. **c,d**, Non-interacting valence bands of BLG near the K and K' points of the Brillouin zone at $D/\epsilon_0 = 0.2 \text{ V/nm}$, with proximitized Ising SOC $|\lambda_I| \approx 1.6 \text{ meV}$ (**c**) and 0.4 meV (**d**), respectively. **e**, Ising SOC strength $|\lambda_I|$ versus BLG-WSe₂ interfacial twist angle θ ; data were extracted from three sets of devices D1-D3. The bottom schematics show the relative rotation between the BLG and WSe₂ Brillouin zones. **f,g**, R_{xx} versus B_\perp and doping n measured at $D/\epsilon_0 = 0.2 \text{ V/nm}$ for devices with $|\lambda_I| \approx 1.6 \text{ meV}$ (**f**) and 0.4 meV (**g**), respectively. **h,i**, Fast Fourier transform (FFT) of $R_{xx}(1/B_\perp)$ (using data within $0.05 < B_\perp < 0.8 \text{ T}$) versus n and f_ν . The arrowed FFT splittings reflect the Ising-induced Fermi-surface imbalance, where larger Ising SOC (**h**) features a larger splitting than small Ising SOC (**i**).

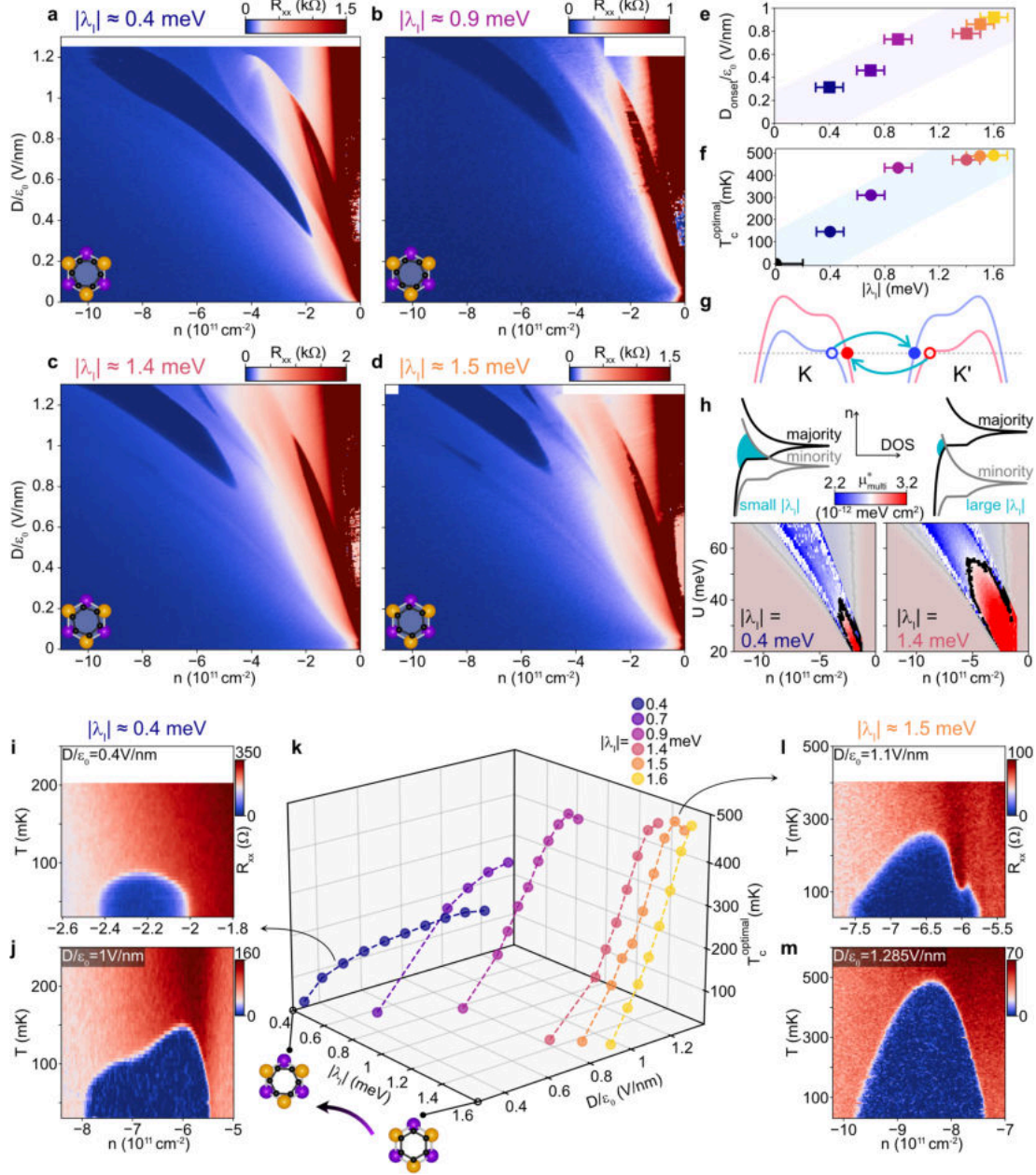


Figure 2 | Twist-programmable superconducting phase diagram. **a–d**, R_{xx} versus n and D for devices with $|\lambda_I| \approx 0.4$ meV (**a**), 0.9 meV (**b**), 1.4 meV (**c**), and 1.5 meV (**d**), respectively. **e,f**, Displacement field at which superconductivity onsets D_{onset} (**e**) and optimal critical temperature T_c^{optimal} (**f**) versus $|\lambda_I|$. The black dot in **f** represents the case at $|\lambda_I| \approx 0$ meV; see also Methods and SI Fig. 4. **g**, Schematic showing the interband interactions (turquoise arrows) between majority and minority flavors. **h**, μ_{multi}^* versus n and interlayer potential difference U for $|\lambda_I| = 0.4$ meV (left) and 1.4 meV (right), respectively. Top schematics show the Ising-imbalanced DOS; turquoise regions indicate where both bands have large DOS. **i,j**, R_{xx} versus n and temperature for a device with $|\lambda_I| \approx 0.4$ meV, measured at $D/\epsilon_0 = 0.4$ V/nm (**i**) and 1 V/nm (**j**), respectively. **k**, Optimal critical temperature T_c^{optimal} versus $|\lambda_I|$ and D . **l,m**, R_{xx} versus n and temperature for a device with $|\lambda_I| \approx 1.5$ meV, measured at $D/\epsilon_0 = 1.1$ V/nm (**l**) and 1.285 V/nm (**m**), respectively.

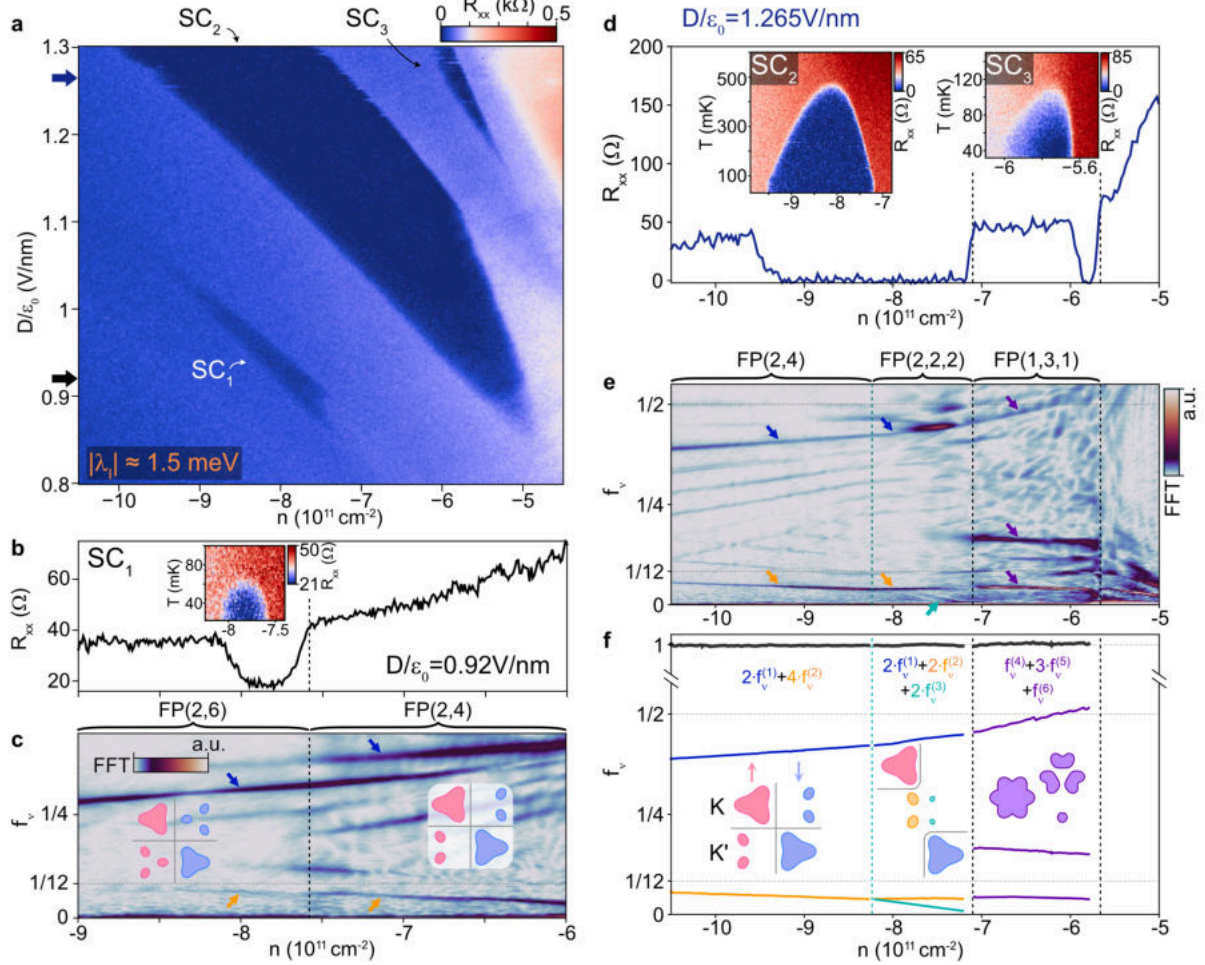


Figure 3 | Superconductivity across nematic redistribution and from inter-valley coherence. **a**, R_{xx} versus n and D for a device with Ising SOC strength $|\lambda_I| \approx 1.5$ meV, focusing around the phase space where the three superconducting regions coexist. **b**, R_{xx} versus n measured at $D/\epsilon_0 = 0.92$ V/nm. The inset shows R_{xx} versus n and temperature for the superconducting dome SC₁. **c**, Frequency-normalized FFT of $R_{xx}(1/B_{\perp})$ (using data within $0.08 < B_{\perp} < 0.4$ T) over the same doping range as in **b**; schematics show the corresponding flavor symmetry-breaking Fermi surfaces. **d**, R_{xx} versus n measured at $D/\epsilon_0 = 1.265$ V/nm. Insets show R_{xx} versus n and temperature for the superconducting domes SC₂ (left) and SC₃ (right), respectively. **e**, Frequency-normalized FFT of $R_{xx}(1/B_{\perp})$ (using data within $0.05 < B_{\perp} < 0.8$ T to resolve $f_{\nu}^{(3)}$) over the same doping range as in **d**. The arrows mark the primary FFT peaks, as shown in **f**. The green dashed line marks the transition from FP(2, 2, 2) to FP(2, 4); black dashed lines mark first-order symmetry-breaking transitions. **f**, Intensity peaks in f_{ν} extracted from **e**. The black solid lines around $f_{\nu} = 1$ indicate the results from the Luttinger sum rule. Schematics from left to right correspond to nematic FP(2, 4), nematic FP(2, 2, 2), and inter-valley coherent FP(1, 3, 1).

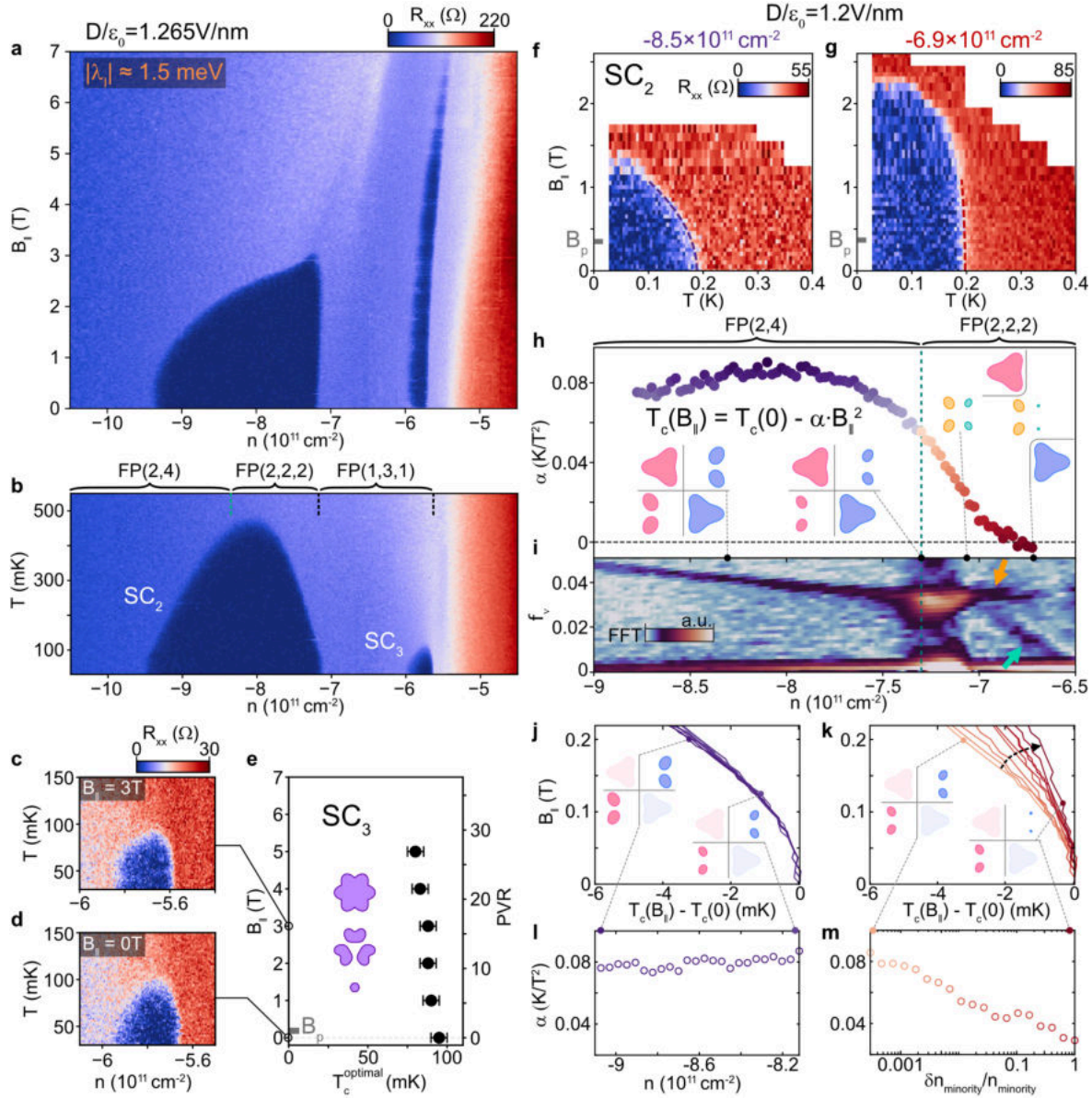


Figure 4 | Ultra-high Pauli-limit violation and nematicity-intertwined B_{\parallel} depairing. **a**, R_{xx} versus n and B_{\parallel} at $D/\epsilon_0 = 1.265$ V/nm for a device with $|\lambda_I| \approx 1.5$ meV. **b**, R_{xx} versus n and temperature at the same D . **c,d**, R_{xx} versus n and temperature for SC₃ measured at $B_{\parallel} = 0$ T (**c**) and 3 T (**d**), respectively. **e**, T_c^{optimal} of SC₃ versus B_{\parallel} . The grey bar marks the Pauli limit. **f,g**, R_{xx} versus temperature and B_{\parallel} at $n = -8.5 \times 10^{11} \text{ cm}^{-2}$ (**f**) and $-6.9 \times 10^{11} \text{ cm}^{-2}$ (**g**), respectively for $D/\epsilon_0 = 1.2$ V/nm. The colored dashed lines are quadratic fitting. **h**, α versus n within the SC₂ at $D/\epsilon_0 = 1.2$ V/nm. **i**, Normalized FFT of $R_{xx}(1/B_{\perp})$ (using data within $0.05 < B_{\perp} < 0.8$ T to resolve $f_{\nu}^{(3)}$) over the same n and D range as in **h**, focusing at low frequencies. Green dashed line marks the nematic redistribution of holes from FP(2, 4) to FP(2, 2, 2). Schematics in **h** show the Fermi-surface evolution versus n . **j,k**, Theoretical B_{\parallel} depairing with the prominent interband pairing (**j**) and the suppressed case by valley polarization (**k**). **l,m**, Theoretical α versus n for FP(2, 4) (**l**) and versus minority imbalance $\delta n_{\text{minority}}/n_{\text{minority}}$ for FP(2, 2, 2) (**m**).

Methods

Device fabrication: The majority of the fabrication processes follow the standard flake transfer and lithography explained in a previous study¹⁷. Here, we focus on the interfacial twisting between BLG and WSe₂. Large flakes of BLG and WSe₂ are exfoliated on SiO₂/Si chips. The crystal orientation of WSe₂ can be identified by second harmonic generation⁵¹ (SHG; Extended Data Fig. 1b), where the polarization of the incident and reflected beams are selected to lie parallel to the scattering plane. The directions with maximized SHG signal correspond to the in-plane crystal orientations along the W-Se direction (armchair direction). BLG is somewhat trickier. We identify flakes with long straight edges forming angles that are multiple of 30°, e.g., three edges form two angles of 150° in Extended Data Fig. 1c. The configuration is consistent with the assignment that the straight edges are along the zigzag- or armchair-edge direction of graphene. We then cut the large BLG flake into small pieces by atomic-force-microscope-actuated cutting²⁴; Extended Data Fig. 1d. First, pick up topmost hBN, top graphite gate, top hBN dielectric, and the large WSe₂ flake using propylene carbonate (PC) film on a polydimethylsiloxane (PDMS). Then, align the straight edge of BLG with the crystal orientation of WSe₂ and control the approach of PC/PDMS stamp so that only one BLG piece is picked up. SiO₂/Si chip was manually rotated by an angle $\theta \sim 6^\circ$, and a second piece of BLG was picked up but not overlapping with the first one. Repeat the same processes for the remaining BLG pieces (Extended Data Fig. 1f,g). Depending on whether the BLG straight edge used for alignment is along the zigzag or armchair direction, the crystal axes of the six BLG pieces are rotated relative to the WSe₂ axis by an angle $\theta \sim 0^\circ, 6^\circ, 12^\circ, 18^\circ, 24^\circ$, and 30° (armchair direction), or vice versa (zigzag direction). The two configurations can be distinguished by measuring the Ising SOC strengths of the devices at the two ends. The large (small) Ising device corresponds to $\sim 0^\circ$ ($\sim 30^\circ$) alignment due to the reflection symmetry^{16,20–22}. A typical finished stack is shown in Extended Data Fig. 1h; a series of different rotation angles between BLG and WSe₂ can be clearly seen from the optical image. The stack went through standard lithographic and etching processes for final device preparation (Extended Data Fig. 1i).

Measurements: All measurements were performed in a dilution refrigerator (Oxford Triton) with a base temperature of ~ 30 mK and an 1T/1T/9T (XYZ) superconducting vector magnet, using standard low-frequency lock-in amplifier techniques. Unless otherwise specified, measurements are taken at the base temperature. Frequencies of the lock-in amplifiers (Stanford Research, models 865a) were kept in the range of 7 – 40 Hz in order to reduce the electronic noise and measure the device’s DC properties. The AC excitation was kept < 5 nA; most measurements were taken at 1 nA to preserve the linearity of the system and to avoid disturbing the fragile states at low temperatures. Each of the DC fridge lines passes through cold filters, including 4 Pi filters that filter out a range from ~ 80 MHz to > 10 GHz, as well as a two-pole RC low-pass filter.

Reproducibility of twist-programmable superconductivity: SI Fig. 1 to 3 show the data measured from three sets of moiréless twisting devices (D1-D3), with the corresponding devices marked by the labels in the optical images. θ -modulated Ising SOC and superconductivity are well reproduced from all the three sets of devices. Within each set, we see a clear trend that su-

perconductivity onsets at a lower D field for the device with low Ising SOC and gradually onsets at a higher D field for the device with large Ising SOC. Accordingly, Ising SOC strength evolves as a function of twist angle θ . The θ -dependent Ising SOC strengths are summarized in Fig. 1e: the magnitude of proximitized Ising SOC is large within a broad angle range, and is quickly suppressed when $\theta = 20 - 30^\circ$. Specially, the first device in the device set D2 (SI Fig. 2a; see also SI Fig. 4) appears to have a minimal Ising SOC, and superconductivity doesn't appear at zero magnetic field. The device is consistent with the scenario that the alignment between BLG and WSe₂ is $\theta \approx 30^\circ$.

Quantifying Ising SOC: One way to quantify the WSe₂-induced Ising SOC $H_I = \frac{1}{2}\lambda_I\tau_zs_z$ (λ_I is the Ising SOC strength in the main text) is to probe the octet zeroth Landau level (LL) in BLG. Note that these LL energies are not sensitive to Rashba SOC¹³. The sets of two Landau levels that cross at filling factors $\nu = \pm 3$ have opposite layer polarizations, so that their energy difference (at zero D field) is given by $\Delta E = E_Z \pm \lambda_I/2$ (E_Z is the Zeeman gap between spin-up and spin-down LLs). Therefore, the critical field B_\perp^* that makes ΔE vanish is $2E_Z = 2g\mu_B B_\perp^* = \lambda_I$ (see SI Fig. 6a-f). However, this method doesn't work when λ_I is negative since the energy-level crossing is not inverted¹⁵.

Independently, $|\lambda_I|$ can also be extracted from the doping-dependent FFT splitting of the quantum oscillations, regardless the sign of λ_I (Fig. 1f-i and Extended Data Fig. 2a). Extended Data Fig. 2b,c shows the doping-dependent FFT splitting B_{split} measured within the non-interacting phase (schematics in Fig. 1h,i) at different D fields and at higher doping densities (i.e., away from the van Hove singularities). Ising-type splitting is suppressed with increasing $|n|$, in contrast to the Rashba-type splitting which increases with increasing $|n|$ ¹⁷. The detailed mapping of B_{split} as a function of n and D enables comparison to single-particle band structure calculation (SI, section 2) that quantifies Ising-induced Fermi surface imbalance. The dashed lines in Extended Data Fig. 2b,c are calculated frequency splittings for $|\lambda_I| \approx 1.4$ meV (Extended Data Fig. 2b) and $|\lambda_I| \approx 0.4$ meV (Extended Data Fig. 2c), respectively. Both cases roughly match the experimental data. The overall trend is that (i) at constant $|\lambda_I|$, higher D features larger B_{split} and (ii) at constant D , higher $|\lambda_I|$ features larger B_{split} . The observed trends put strong constraints on the estimates of the Ising SOC strength.

Note that one single Ising SOC strength provides a good fit to the data at different D fields (from $D/\epsilon_0 = 0.2$ V/nm to 1 V/nm; Extended Data Fig. 2b), suggesting that Ising SOC is already maximal at $D/\epsilon_0 = 0.2$ V/nm and larger D values do not further increase the Ising SOC strength. For Ising extraction, frequency analysis at a finite D field and higher doping (i.e., away from the van Hove singularities) is more accurate in comparison to the zero D case for the following reasons: (i) Ising-induced splitting is significantly suppressed at the zero D limit (SI Fig. 5), which makes it difficult to precisely quantify by comparing to the single-particle band structure (gray dashed line in Extended Data Fig. 2b); and (ii) the effective Rashba SOC is more pronounced⁵² at $D/\epsilon_0 = 0$ V/nm due to reduced sublattice and layer polarizations, which further complicates the analysis; see SI, section 2 and SI Fig. 10. The evolution of the effective Rashba SOC is plotted

in SI Fig. 10. We find that for moderate values of interlayer potential difference ($U > 15$ meV), the microscopic Rashba SOC induced by WSe₂ becomes strongly suppressed, consistent with the experiment.

SI Fig. 6a-f shows the Landau level crossing for $\nu = \pm 3$, while SI Fig. 6g shows the corresponding quantum oscillation frequencies within the non-interacting Ising symmetry-breaking phase. Both methods return $|\lambda_I| \approx 1.6$ meV, validating the quantum oscillation method in the manuscript.

Principles for FFT analysis: Correctly identifying the quantum oscillation frequencies is critical for figuring out the type and the number of Fermi pockets for each flavor-polarized phases. Here, we summarize basic principles for FFT analysis, applying them to FP(2, 2, 2) and FP(1, 3, 1).

1. To identify the intrinsic Fermi-surface frequencies, we want to work on FFT analysis with B_{\perp} range as low as possible. At slightly higher B_{\perp} , magnetic breakdown⁵³ kicks in as B_{\perp} -assisted electron tunneling between different Fermi surfaces. Consequently, the most pronounced frequencies might be a sum (or difference) of two base frequencies instead of the intrinsic ones.
2. Follow the sum rule that all the intrinsic frequencies with their multiplications add up to 1. The multiplications return the number of Fermi pockets for each type. Looking at the doping dependence of f_{ν} , if one frequency $f_{\nu}^{(1)}$ decreases versus doping, it is guaranteed that there is another frequency that evolves reversely. One pocket shrinks while some other pockets grow.
3. We check for the evolution of phase diagram as a function of D fields and doping n . Some FFT frequencies continuously evolve in the n - D phase space, which provides further guidance for the neighboring correlated phases.

Identification of FP(2, 2, 2) phase: Ultrahigh-resolution quantum oscillations at high D fields allow for resolving subtle symmetry-breaking Fermi pockets. Looking carefully at the FFT frequency $f_{\nu}^{(2)}$ in Extended Data Fig. 5b and Extended Data Fig. 6b,d, $f_{\nu}^{(2)}$ decreases monotonically with lowering doping until reaching $n \approx -8.25 \times 10^{11} \text{ cm}^{-2}$ for $D/\epsilon_0 = 1.265 \text{ V/nm}$ ($n \approx -7.2 \times 10^{11} \text{ cm}^{-2}$ for $D/\epsilon_0 = 1.2 \text{ V/nm}$), beyond which the dependence of $f_{\nu}^{(2)}$ is flattened while $f_{\nu}^{(1)}$ keeps increasing throughout. This indicates that the sum rule $2 \cdot f_{\nu}^{(1)} + 4 \cdot f_{\nu}^{(2)} \approx 1$ of the FP(2, 4) phase at higher doping is no longer satisfied for lower dopings, suggesting an altered Fermi-surface structure. Indeed, measuring quantum oscillations to higher B_{\perp} field reveals the emergence of a third very low frequency around the phase boundary as marked by the green arrows in Extended Data Fig. 7. FFT data shown in Extended Data Fig. 5b and Extended Data Fig. 6b,d clearly reveal the third frequency $f_{\nu}^{(3)}$ growing rapidly from zero at the phase boundary to a value matching $f_{\nu}^{(2)}$ at slightly higher doping. The frequencies obey $2 \cdot f_{\nu}^{(1)} + 2 \cdot f_{\nu}^{(2)} + 2 \cdot f_{\nu}^{(3)} \approx 1$,

as discussed in the main text corresponding to an additional symmetry breaking with trigonally warped pockets of two sizes $f_\nu^{(2)}$ and $f_\nu^{(3)}$.

Identification of FP(1, 3, 1) phase: The identification of FP(1, 3, 1) phase is more subtle, involving extensive quantum oscillation measurements. The raw data (Extended Data Fig. 7a,b; $n \approx -6.6 \times 10^{11} \text{ cm}^{-2}$ to $-5.3 \times 10^{11} \text{ cm}^{-2}$ taken at $D/\epsilon_0 \approx 1.2 \text{ V/nm}$) reveal three oscillation frequencies. A high frequency marked $f_\nu^{(4)}$ appears clearly. At really low $B_\perp \sim 0.05 \text{ T}$, a relatively low frequency called $f_\nu^{(6)}$ onsets. Further increasing B_\perp , each $f_\nu^{(6)}$ period splits into four, giving rise to $f_\nu^{(5)}$ which is indeed roughly four times the frequency $f_\nu^{(6)}$ (Extended Data Fig. 7c).

It is natural to ask whether $f_\nu^{(5)}$ is simply a higher (fourth) harmonic of $f_\nu^{(6)}$. This can be answered by the measurements at low D fields in the same phase region (Extended Data Fig. 8 and 9). Frequencies are marked by arrows. When lowering the D fields, $f_\nu^{(4)}$ gradually increases, while $f_\nu^{(5)}$ and $f_\nu^{(6)}$ gradually decrease. At $D/\epsilon_0 = 1 \text{ V/nm}$ (Extended Data Fig. 8b,d,f), $f_\nu^{(5)}$ already deviates from being four times the value of $f_\nu^{(6)}$. Eventually at $D/\epsilon_0 = 0.85 \text{ V/nm}$ (Extended Data Fig. 8a,c,e), the frequency $f_\nu^{(6)}$ completely disappears while $f_\nu^{(5)}$ independently survives. This D evolution of the two frequencies ($f_\nu^{(5)}$ and $f_\nu^{(6)}$) supports their independence. Meanwhile at $D/\epsilon_0 = 0.85 \text{ V/nm}$, the existing two frequencies ($f_\nu^{(4)}$ and $f_\nu^{(5)}$) obey $f_\nu^{(4)} + 3 \cdot f_\nu^{(5)} \approx 1$; we denote the flavor-polarized phase at this D field as FP(1, 3). The above D -field evolution indicates that the FP(1, 3, 1) phase at high D develops from the FP(1, 3) phase at low D as D is increased.

After establishing the existence of three frequencies, we comment on the number of pockets for each type. This relies on the correct identification of intrinsic Fermi-surface frequencies and their harmonics. At slightly higher B_\perp , magnetic breakdown⁵³ kicks in as B_\perp -assisted electron tunneling between different Fermi surfaces. Consequently, the pronounced frequencies might be a sum (or difference) of two base frequencies instead of the intrinsic ones. This is the case for FP(1, 3) and FP(1, 3, 1) phase. Extended Data Fig. 8c shows the normalized FFT from quantum oscillations going up to $B_\perp = 0.45 \text{ T}$. The frequency peak at $f_\nu \sim 0.75$ is stronger than the one at $f_\nu \sim 0.6$ (marked by the arrow). However, the relative intensity changes by reducing the B_\perp range to 0.23 T (Extended Data Fig. 10a). At this condition, the peak at $f_\nu \sim 0.6$ is stronger than the one at $f_\nu \sim 0.75$, suggesting that the one marked by the arrow ($f_\nu \sim 0.6$ in Extended Data Fig. 10a) is the intrinsic frequency; the one at $f_\nu \sim 0.75$ is instead a sum harmonic $f_\nu^{(4)} + f_\nu^{(5)}$. By identifying the intrinsic high frequency $f_\nu^{(4)}$, one obtains $f_\nu^{(4)} + 3 \cdot f_\nu^{(5)} \approx 1$, indicating one large and three small Fermi surfaces, i.e., FP(1, 3). A similar situation holds for the other D fields, such as at $D/\epsilon_0 = 1.2 \text{ V/nm}$ (see Extended Data Fig. 9c and Extended Data Fig. 10c), where we find $f_\nu^{(4)} + 3 \cdot f_\nu^{(5)} + f_\nu^{(6)} \approx 1$.

Inter-valley coherence: The occurrence of superconducting state SC_3 in the symmetry-breaking state FP(1, 3, 1) strongly indicates the inter-valley coherent nature of FP(1, 3, 1). Focusing on the single largest Fermi pocket ($f_\nu^{(4)}$) that is non-degenerate, there are two options: it is either

valley-polarized and therefore breaks time-reversal symmetry, or it is inter-valley coherent. Coherence between the K and K' valleys would restore time reversal symmetry for the largest Fermi pocket, naturally more susceptible to pairing. Note that in moiré graphene, it is established that superconductivity originates from an inter-valley-coherent order^{37,38}.

Independent evidence for inter-valley coherence comes from analyzing the evolution of phase boundaries as a function of B_\perp . An out-of-plane magnetic field B_\perp favors valley-polarized states that are characterized by large orbital moments. As B_\perp field is increased, valley-polarized states with large orbital moments are expected to take over more of the phase space compared to valley-balanced states³⁹. The evolution of the phase boundaries with B_\perp can be clearly identified from quantum oscillations (Extended Data Fig. 11). Here, the lowest doping density range ($n > -3 \times 10^{11} \text{ cm}^{-2}$) corresponds to a spin-valley locked FP(6) phase¹⁷. Within this phase, the K and K' valleys are equally populated with opposite spins, resulting in zero net orbital moment. At the doping density $-3 > n > -4.3 \times 10^{11} \text{ cm}^{-2}$, the oscillation frequency peaks at $f_\nu = 1$ indicating FP(1) phase. The phase space shows a rich evolution: a phase transition develops with increasing B_\perp , consistent with a spin-valley polarized FP(1) (red line in Extended Data Fig. 11b) emerges when B_\perp is applied. Importantly, at the lowest B_\perp ($B_\perp \sim 0 \text{ T}$), the phase boundary between FP(1) and FP(6) (black dashed line at $n \approx -3 \times 10^{11} \text{ cm}^{-2}$) doesn't move with B_\perp , suggesting that the FP(1) at $B_\perp \sim 0 \text{ T}$ is characterized by coherence between the two valleys (over the spin-valley polarized phase), so that the orbital moments cancel. The same logic applies to the other symmetry-breaking phases at slightly higher doping. A large FFT frequency dominates at $f_\nu > 1/2$ while the phase boundaries persist in doping without moving when B_\perp is applied, suggesting the existence of one large Fermi pocket with diminished or no orbital moments and hence inter-valley coherence for FP(1, 3, 1).

Sample alignment with in-plane magnetic field: In-plane-field measurements were performed by mounting the sample vertically with a homemade frame to access $B_\parallel > 1 \text{ T}$. A small B_\perp component is inevitably introduced when B_\parallel is applied due to imperfect vertical sample alignment. The B_x and B_y directions of the vector magnet are used to compensate the B_\perp component. The compensation is crucial for the measurements of large Pauli-limit violation of SC₃, because at $B_\parallel = 7 \text{ T}$ or so, an out-of-plane component $B_\perp \approx 0.1 - 0.2 \text{ mT}$ almost completely suppresses the superconductivity. Additionally, the cancellation of B_\perp gives an accurate R_{xx} dependence on B_\parallel and temperature so that the extraction of α in Fig. 4 is reliable.

Multiband superconductivity analysis: We consider an electronic system with two bands, with an additional (spin) degree of freedom in each band. The mean-field ansatz for the simplest order parameter is a vector form due to the multiband structure,

$$\Delta = \hat{g}_{\text{initial}} \left\langle \left(\frac{1}{\Omega} \sum_{\mathbf{k}} \psi_{-\mathbf{k}1+} \psi_{\mathbf{k}1-} \right) \right\rangle, \quad (1)$$

where Ω is the system volume, $\psi_{\mathbf{k},n,p}$ annihilates an electron with momentum \mathbf{k} , in band $n = 1, 2$, and internal flavor $p = \pm$.

We introduce an energy scale ω^* , below which the pairing interaction is activated. In the path-integral formalism, one integrates out the electrons with energy greater than ω^* , obtaining a renormalized interaction matrix,

$$\hat{g}_{\text{TAM}}(\omega^*) = \left[(\hat{g}_{\text{initial}})^{-1} + \begin{pmatrix} \ell_1 & \\ & \ell_2 \end{pmatrix} \right]^{-1}, \quad (2)$$

where $\ell_n = \left\{ \int_{\omega^*}^{\infty} + \int_{-\infty}^{-\omega^*} \right\} d\xi \frac{\mathcal{N}_n(\xi)}{|\xi|}$, and $\mathcal{N}_n(\xi)$ is the DOS of the n -band at a distance ξ away from the Fermi level.

We define a multiband generalization of the superconducting pseudopotential pseudopotential

$$\mu_{\text{multi}}^* = \sqrt{\det \hat{g}_{\text{TAM}}(\omega^*)}. \quad (3)$$

We note that by setting interband interactions to zero, one simply obtains a diagonal \hat{g}_{TAM} matrix, with the appropriate single-band pseudopotentials $\mu_{1,2}^*$ on its diagonal. Investigation of μ_{multi}^* is motivated by the fact that a superconducting transition is associated with a singularity of the \hat{g} matrix emerging at a $\sim T_c$ energy scale.

Predictions of conventional depairing mechanisms for SC₁, SC₂, and SC₃: Here we summarize the main findings resulting from the conventional depairing mechanisms in the context of SC₁, SC₂, and SC₃, within the Ising superconductor framework^{17,48–50}. For SC₂, we find that experimentally determined values of α are not well reproduced by realistic values of $\lambda_R \lesssim 10$ meV (see SI, section 8). More precisely, conventional depairing theory would predict higher resilience (lower α by almost an order of magnitude) to the in-plane magnetic field. For the case of SC₁, we find that the conventional depairing theory applies well, explaining the large PVR. As such, another mechanism, like the interband-interaction scenario in the main text, must account for the relatively minor PVR in SC₂. The direction of B_{\parallel} can further shed light on the depairing mechanism. Theoretically, SC₁ is not sensitive to the in-plane field direction, as reported previously in Ref. 18. For SC₂, because both FP(2, 4) and FP(2, 2, 2) break the C_3 symmetry, we anticipate a dependence of T_c (or α) as the direction of B_{\parallel} is rotated. Experimentally, however, SC₂ shows no significant variation in T_c as the magnetic field is rotated (Extended Data Fig. 17), suggesting that this simple depairing picture relying on rigid occupancy of the trigonal-warping pockets should be revisited with a self-consistent Hartree-fock (HF) pairing analysis, where the Fermi surfaces adjust in response to the magnetic field. Finally, we also highlight that the mechanism discussed in the main text, the modification of interband and intraband interactions with an in-plane magnetic field, is entirely independent of the field direction. This is in accordance with the experimental observations, yet contrasts with the “conventional” depairing analysis.

Acknowledgments: We thank Jason Alicea, Étienne Lantagne-Hurtubise, Zhiyu Dong, Alex Thomson, Dmitry V. Chichinadze, Andrea Young, and Erez Berg for fruitful discussions.

Funding: This work has been primarily supported by the Office of Naval Research (grant no.

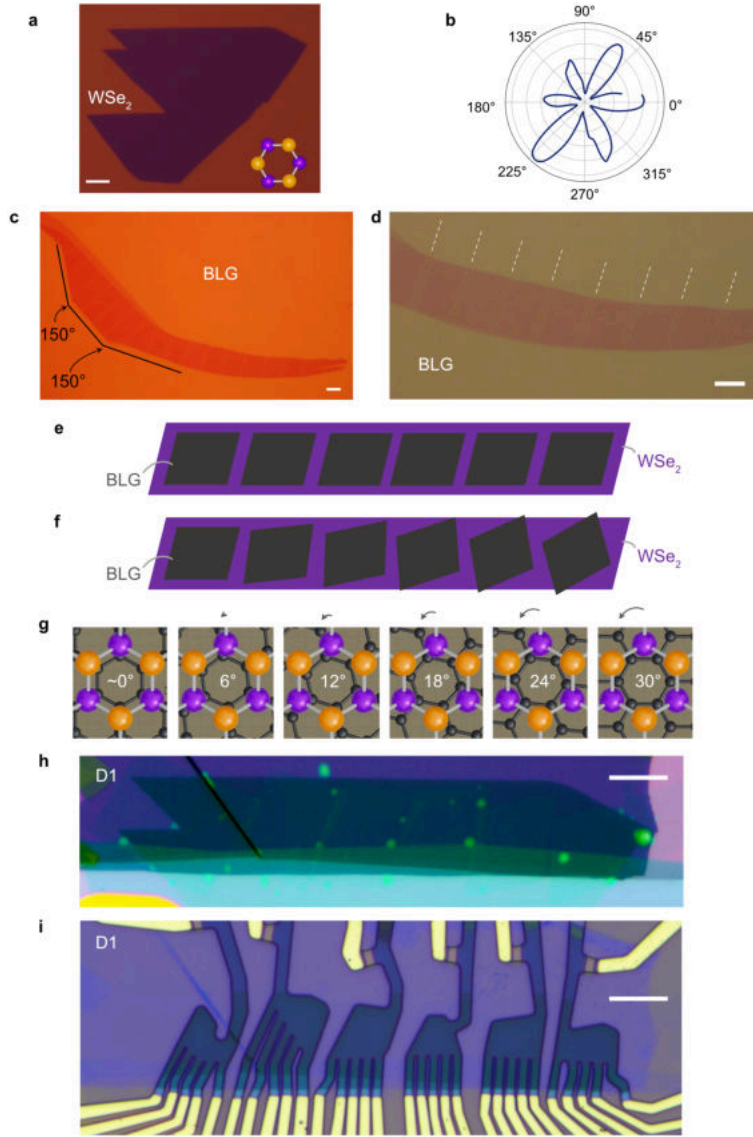
N142112635). S.N.-P. and D.H. also acknowledge the support of the Institute for Quantum Information and Matter, an NSF Physics Frontiers Center (PHY-2317110). G.S. acknowledges support from the Walter Burke Institute for Theoretical Physics at Caltech, and from the Yad Hanadiv Foundation through the Rothschild fellowship. H.M. and C.L. were supported by start-up funds from Florida State University and the National High Magnetic Field Laboratory. The National High Magnetic Field Laboratory is supported by the National Science Foundation through NSF/DMR-2128556 and the State of Florida. Y.O. and F.v.O. acknowledge support by Deutsche Forschungsgemeinschaft through CRC 183 (project C02). F.v.O. was further supported by Deutsche Forschungsgemeinschaft through a joint ANR-DFG project (TWISTGRAPH).

Author Contribution: Y.Z. and S.N.-P. designed the experiment. Y.Z. fabricated the devices, performed the measurements, and analyzed the data. C.W.S. and A.M. helped with the measurements. Y.H. and D.H. performed the SHG measurements. G.S., H.M., C.L., F.v.O., and Y.O. developed theoretical models and performed calculations. K.W. and T.T. provided hBN crystals. S.N.-P. supervised the project. Y.Z., G.S., C.L., F.v.O., Y.O., and S.N.-P. wrote the manuscript with the input of other authors.

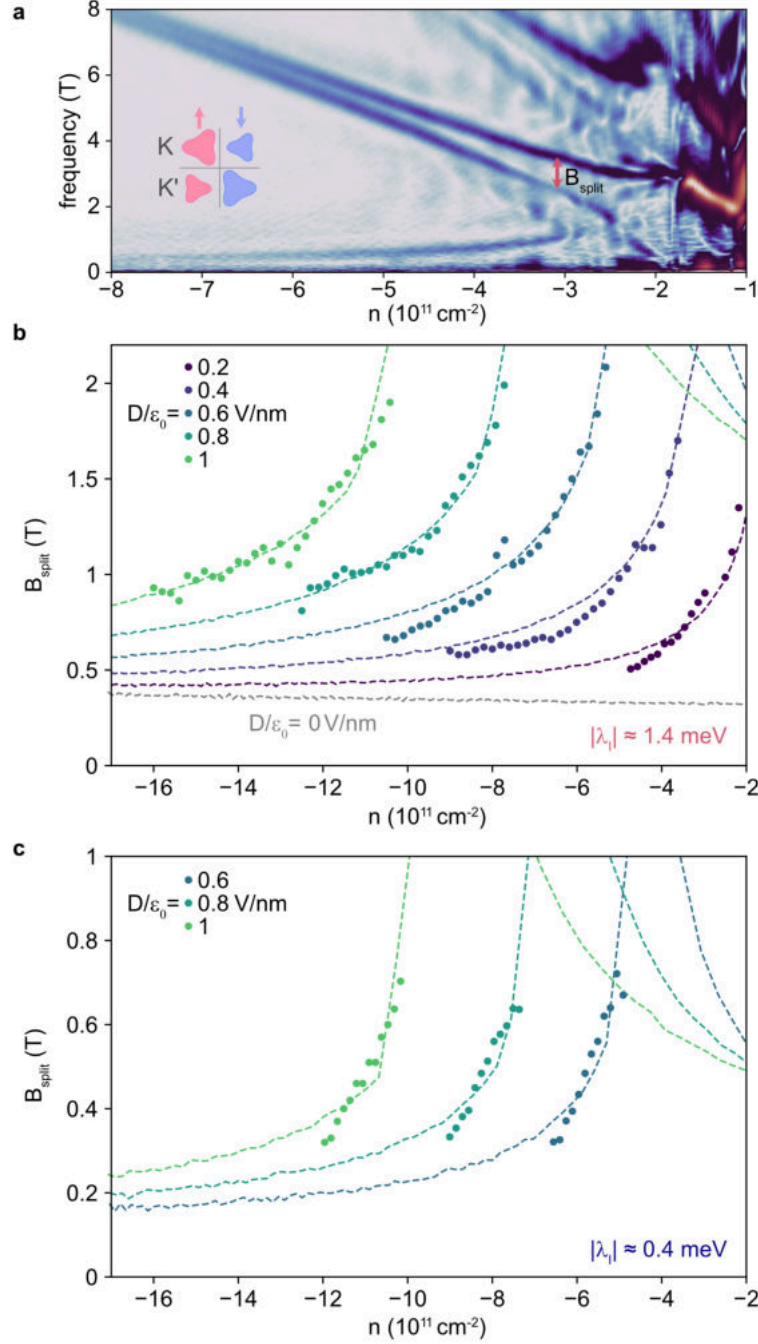
Competing interests: The authors declare no competing interests.

Data availability: The data supporting the findings of this study are available from the corresponding authors on reasonable request.

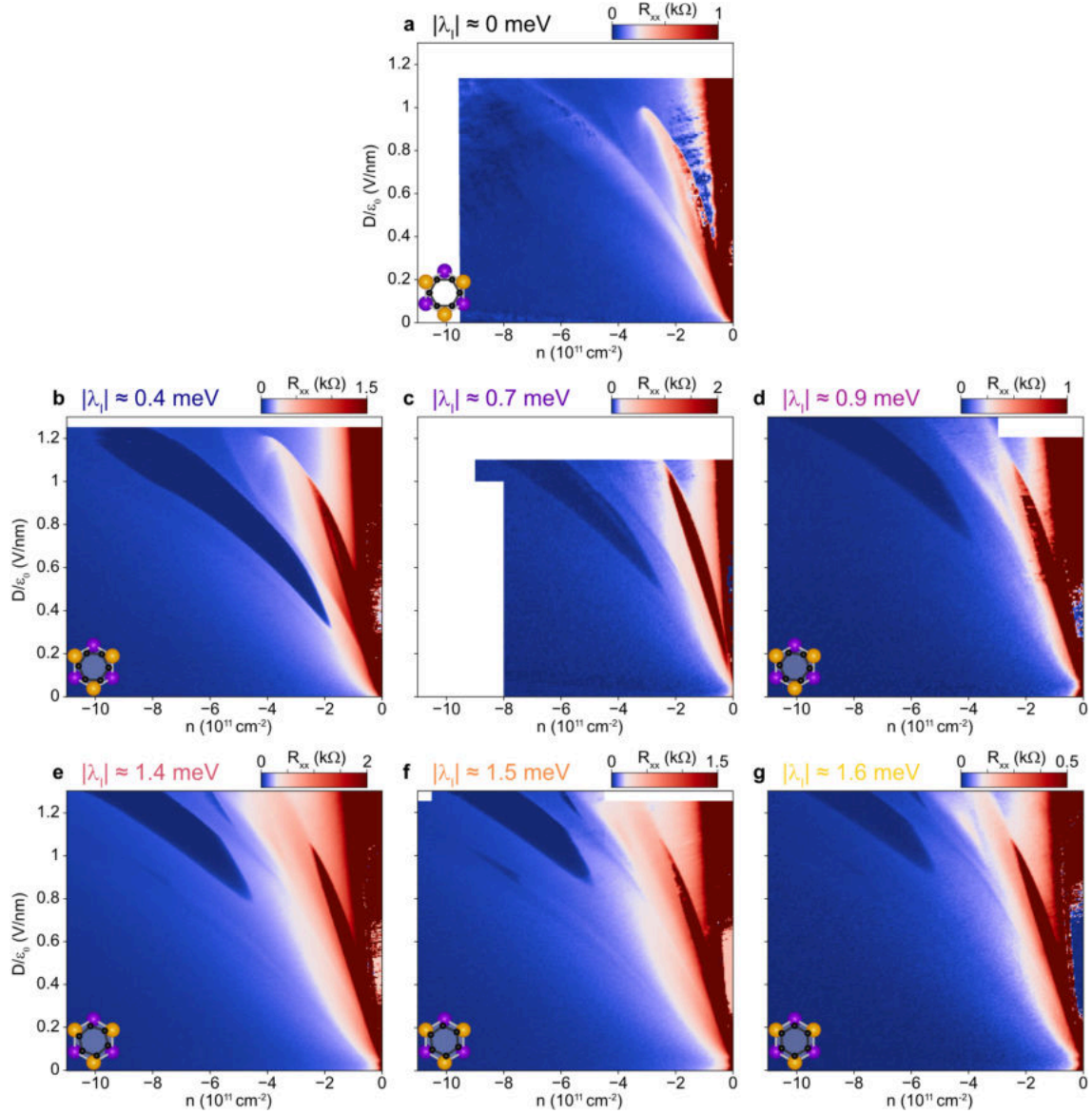
Code availability: All code used in modeling in this study is available from the corresponding authors on reasonable request.



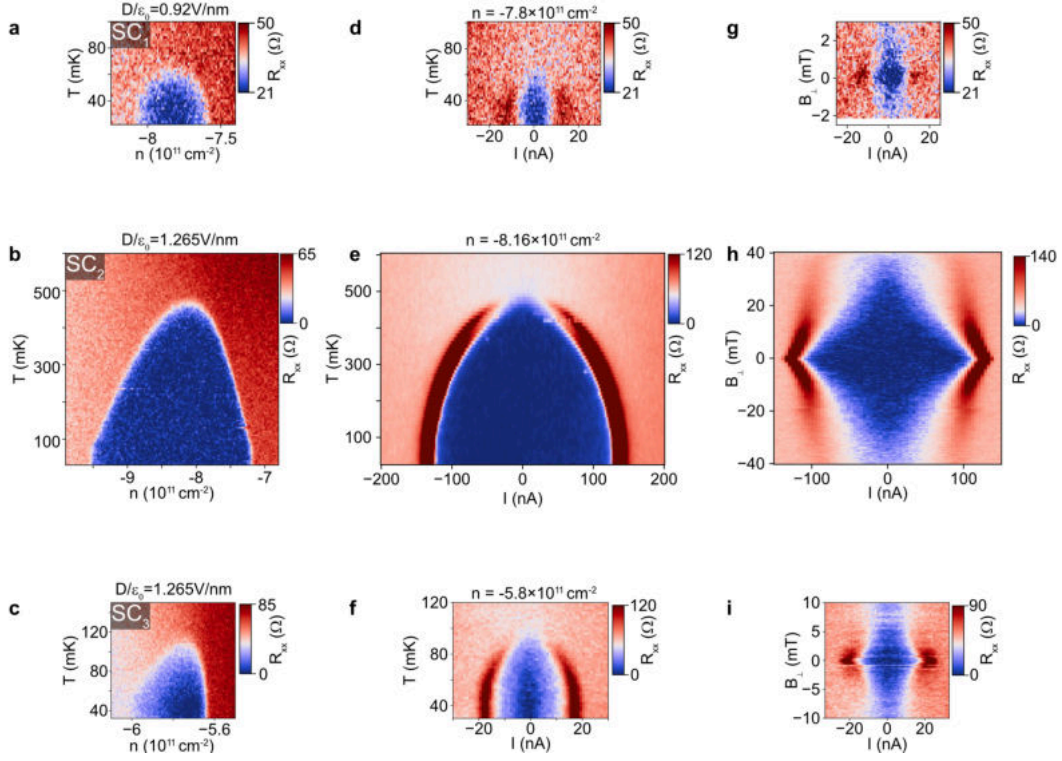
Extended Data Fig. 1 | Device fabrication for BLG-WSe₂ twisting. **a**, Optical image of a WSe₂ crystal. **b**, Second harmonic generation for the WSe₂ flake shown in **a**; the polarization of the incident and reflected beams are selected to lie parallel to the scattering plane. **c**, Optical image of a large BLG flake. Straight edges form angles 150° that are consistent with the three straight edges being along zigzag- or armchair-edge direction. **d**, Zoom-in image of the BLG in **c**, showing small BLG pieces that are separated by atomic-force-microscope-actuated cutting. **e-g**, Schematics showing the flake transferring processes for the continuous interfacial twisting. The BLG pieces are sequentially picked up with angles relative to WSe₂ in increments of 6°, from ~ 0° to 30°. **h**, Optical image of the twisting stack, clearly showing that the BLG pieces form different twist angles relative to the WSe₂ crystal. **i**, Optical image of the finished device set D1. All the scale bars correspond to 10 μm.



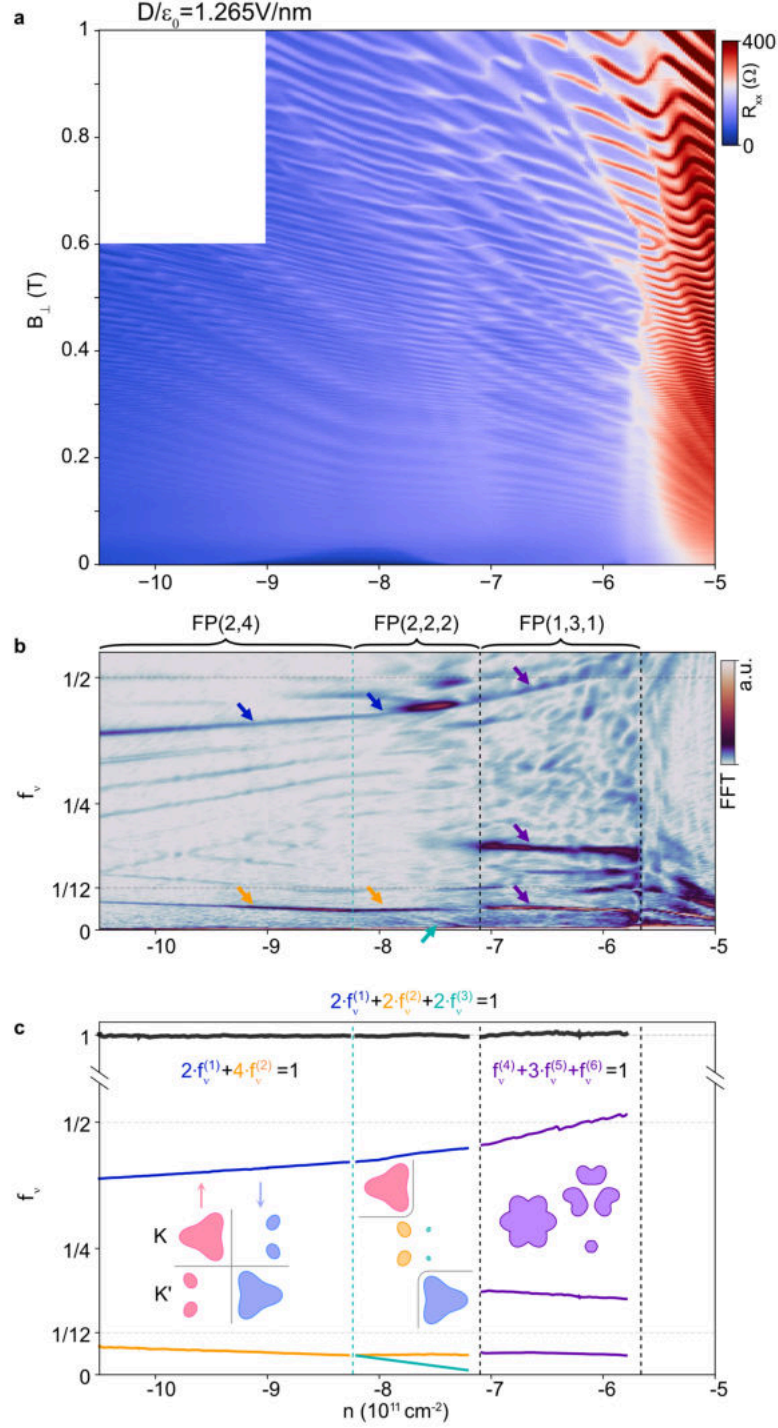
Extended Data Fig. 2 | Quantifying Ising SOC strength $|\lambda_I|$ by quantum oscillations. **a**, The same data as the one in Fig. 1h, but without the frequency normalization to show B_{split} . **b,c**, Experimental (dots) doping-dependent frequency splitting around $f_\nu = 1/4$ measured at different D fields for a large Ising device (**b**; $|\lambda_I| \approx 1.4 \text{ meV}$) and a small Ising device (**c**; $|\lambda_I| \approx 0.4 \text{ meV}$). The dashed lines are B_{split} calculated from single-particle band structure using the corresponding Ising SOC values. The gray dashed line in **b** corresponds to the frequency splitting at zero displacement field.



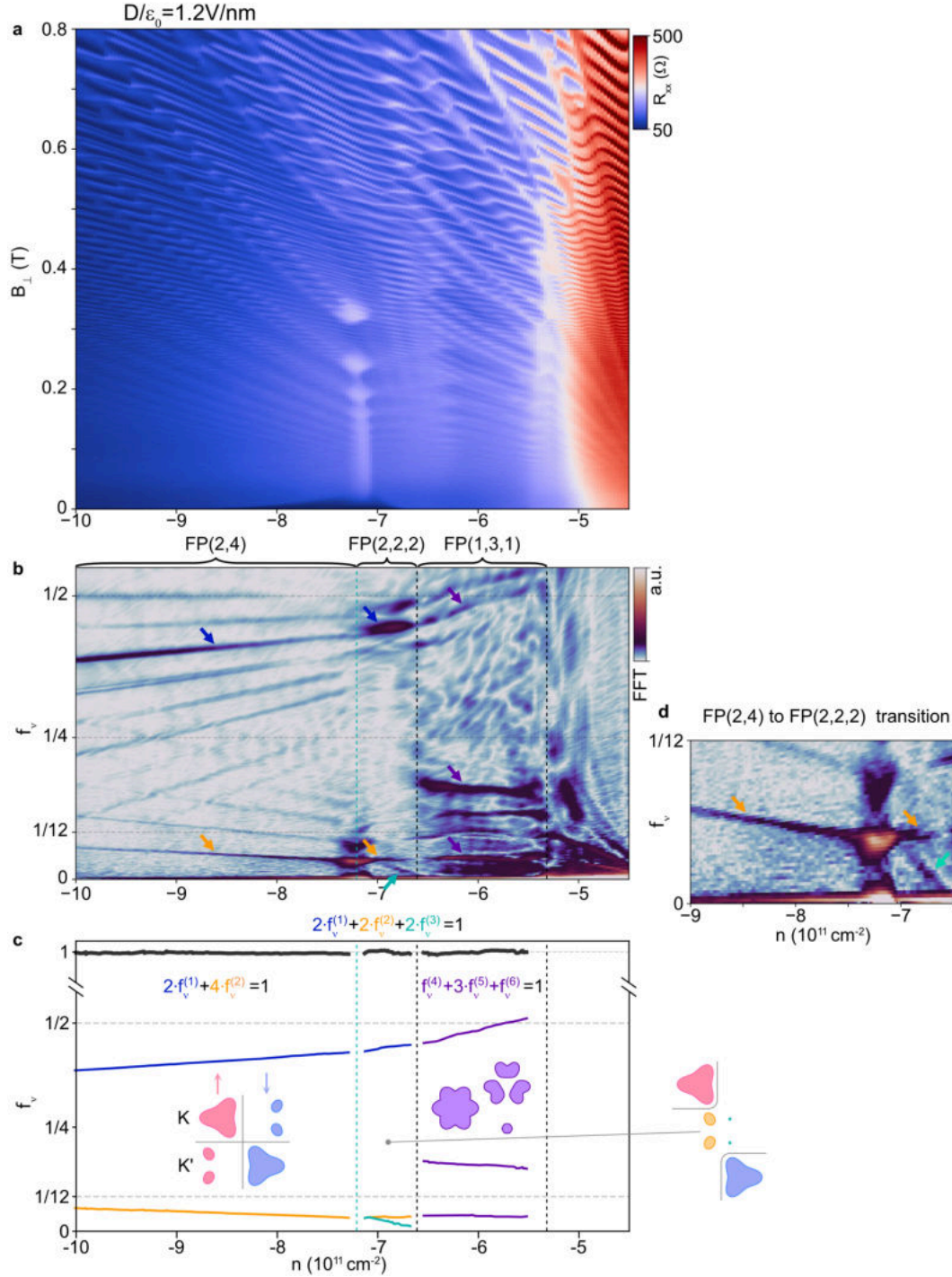
Extended Data Fig. 3 | n - D phase diagrams for devices with various Ising SOC strengths. **a-g**, R_{xx} versus doping density n and displacement field D for devices with Ising SOC strength $|\lambda_I| \approx 0 \text{ meV}$ (**a**), 0.4 meV (**b**), 0.7 meV (**c**), 0.9 meV (**d**), 1.4 meV (**e**), 1.5 meV (**f**), and 1.6 meV (**g**), respectively. See Methods and SI Fig. 4 for detailed discussion and measurement regarding the case at $|\lambda_I| \approx 0 \text{ meV}$.



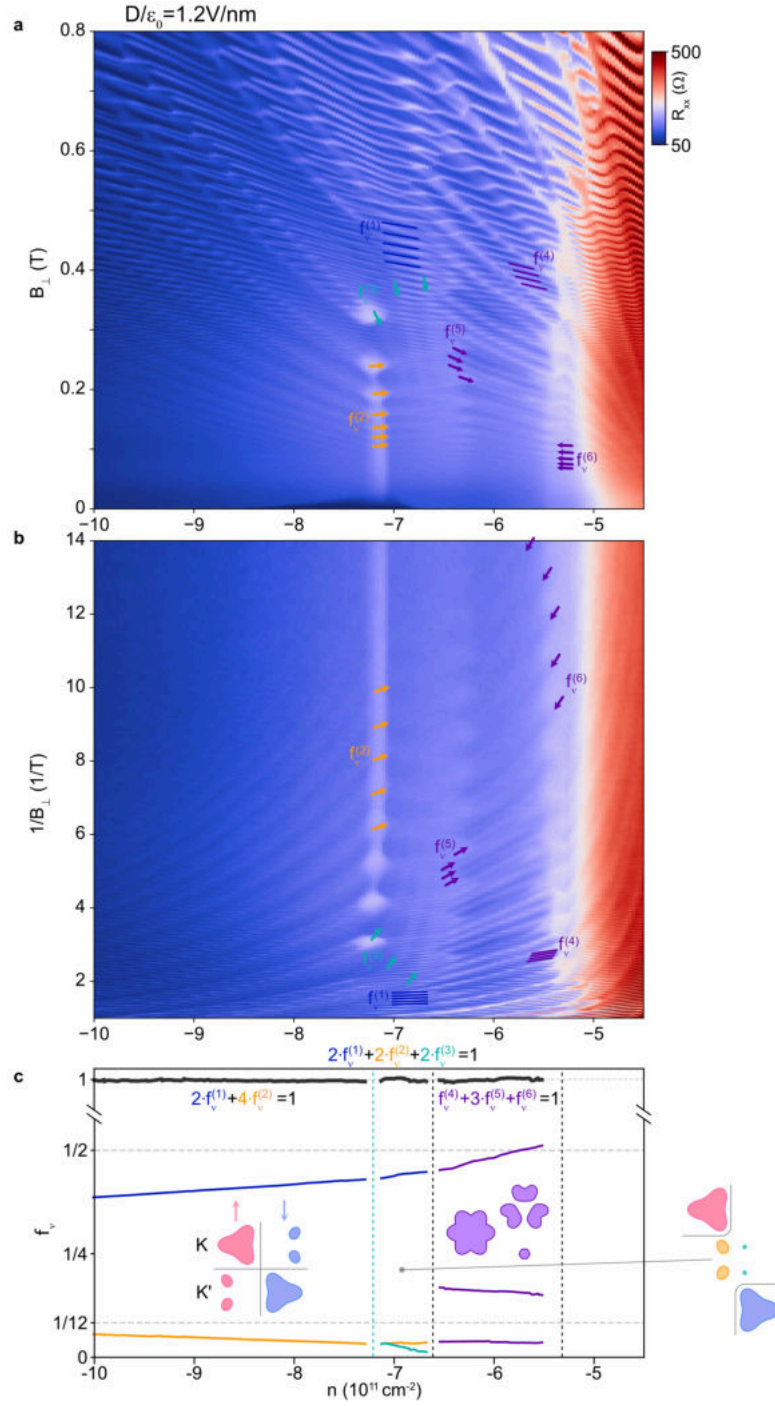
Extended Data Fig. 4 | Characterizations of the three superconducting regions SC₁, SC₂, and SC₃. **a-c**, Temperature dependence of the three superconducting domes SC₁ (**a**), SC₂ (**b**), and SC₃ (**c**), respectively. **d-f**, Critical current versus temperature at the corresponding D and n . **g-i**, Critical current disappearing with B_{\perp} at the same D and n as in **d-f**.



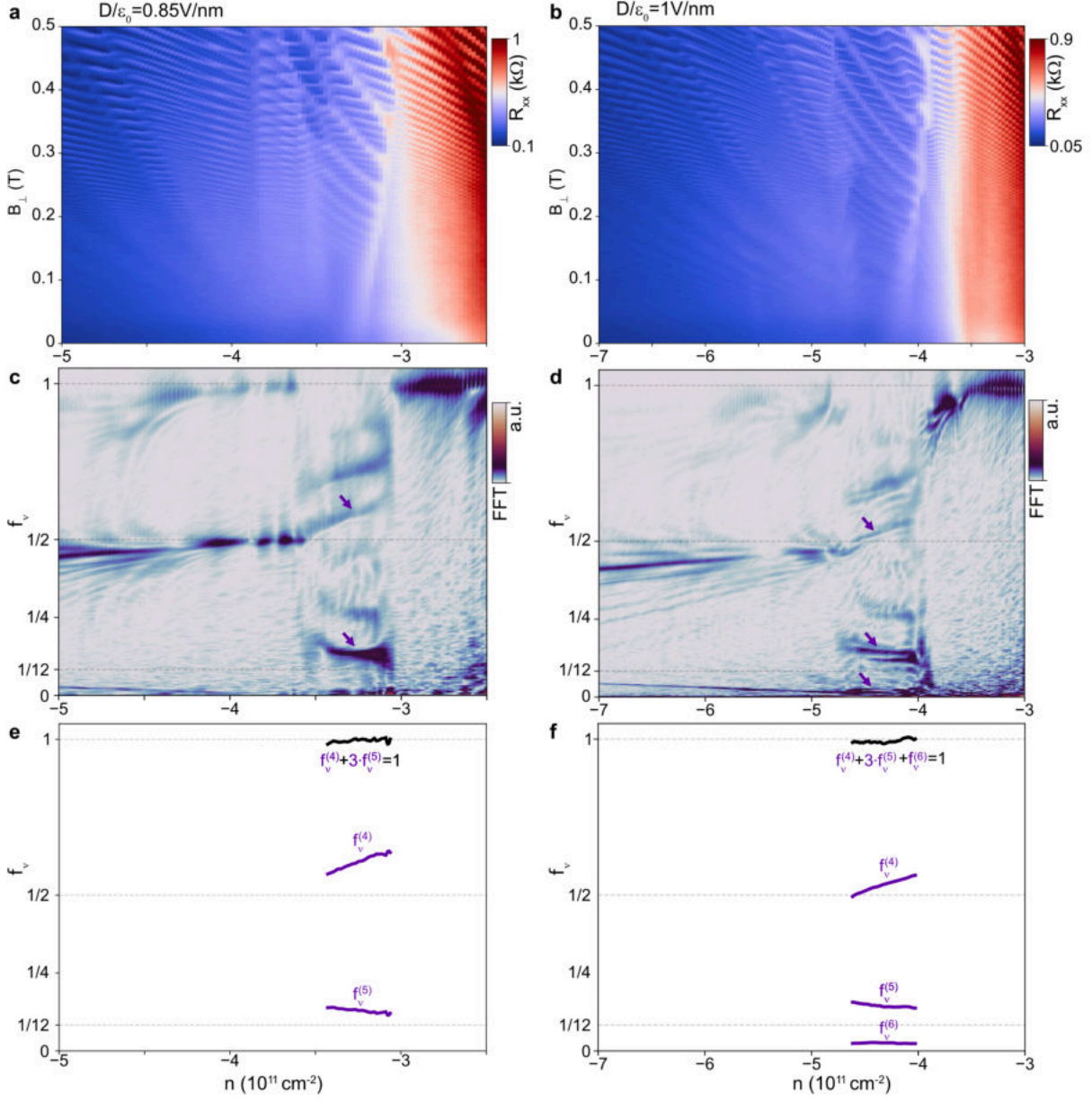
Extended Data Fig. 5 | Quantum oscillations and FFT measured at $D/\epsilon_0 = 1.265 \text{ V/nm}$. **a**, R_{xx} versus out-of-plane magnetic field B_{\perp} and doping density n measured at $D/\epsilon_0 = 1.265 \text{ V/nm}$ for a device with $|\lambda_I| \approx 1.5 \text{ meV}$. **b**, Frequency-normalized Fourier transform of $R_{xx}(1/B_{\perp})$ (using data within $0.05 < B_{\perp} < 0.8 \text{ T}$ to resolve $f_{\nu}^{(3)}$) over the same doping density range as in **a**. **c**, Intensity peaks in f_{ν} from **b**.



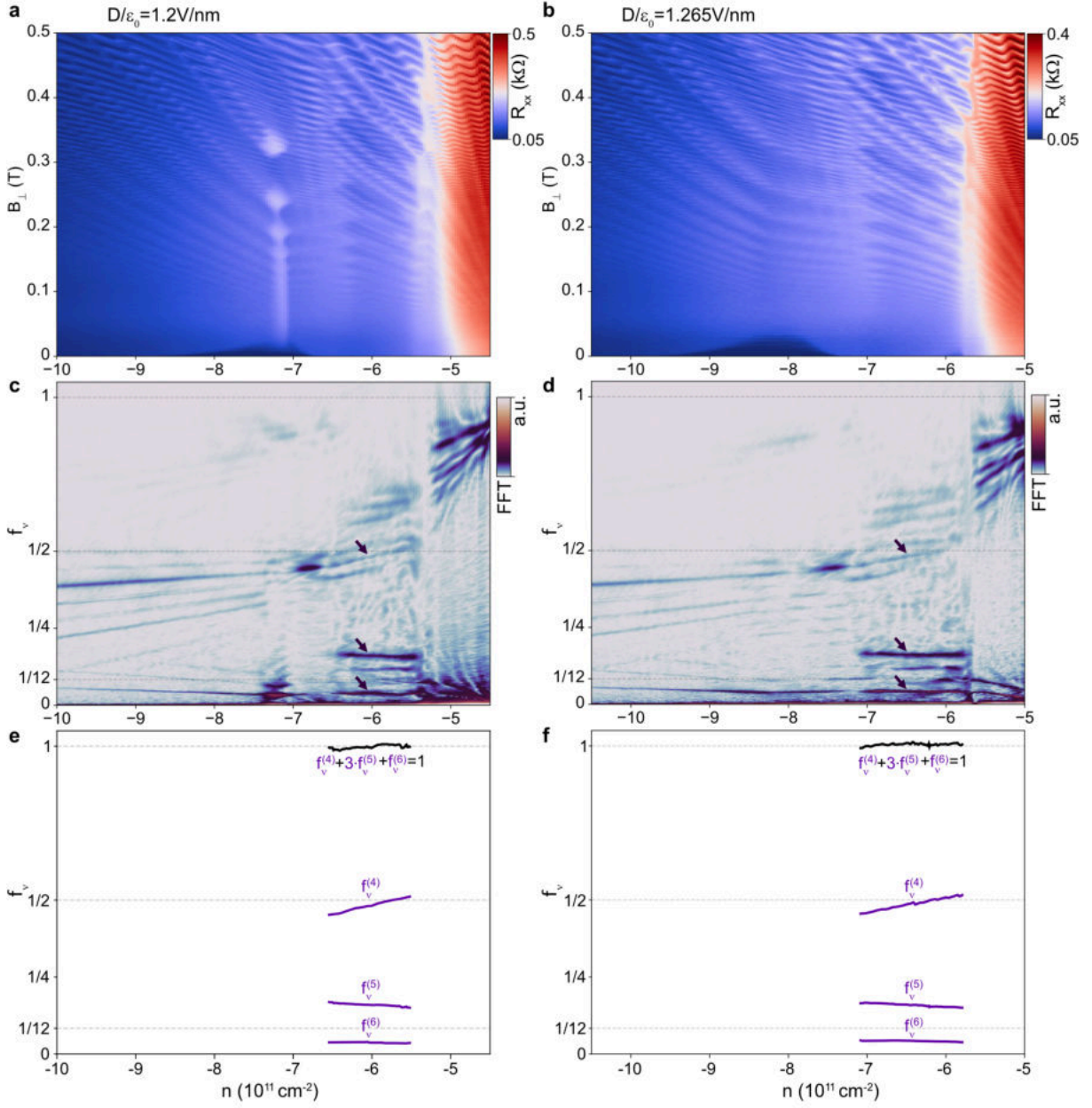
Extended Data Fig. 6 | Quantum oscillations and FFT measured at $D/\epsilon_0 = 1.2 \text{ V/nm}$. **a**, R_{xx} versus out-of-plane magnetic field B_{\perp} and doping density n measured at $D/\epsilon_0 = 1.2 \text{ V/nm}$ for a device with $|\lambda_I| \approx 1.5 \text{ meV}$. **b**, Frequency-normalized Fourier transform of $R_{xx}(1/B_{\perp})$ (using data within $0.05 < B_{\perp} < 0.8 \text{ T}$ to resolve $f_{\nu}^{(3)}$) over the same density range as in **a**. **c**, Intensity peaks in f_{ν} from **b**. **d**, zoom-in image at low frequencies from **b**.



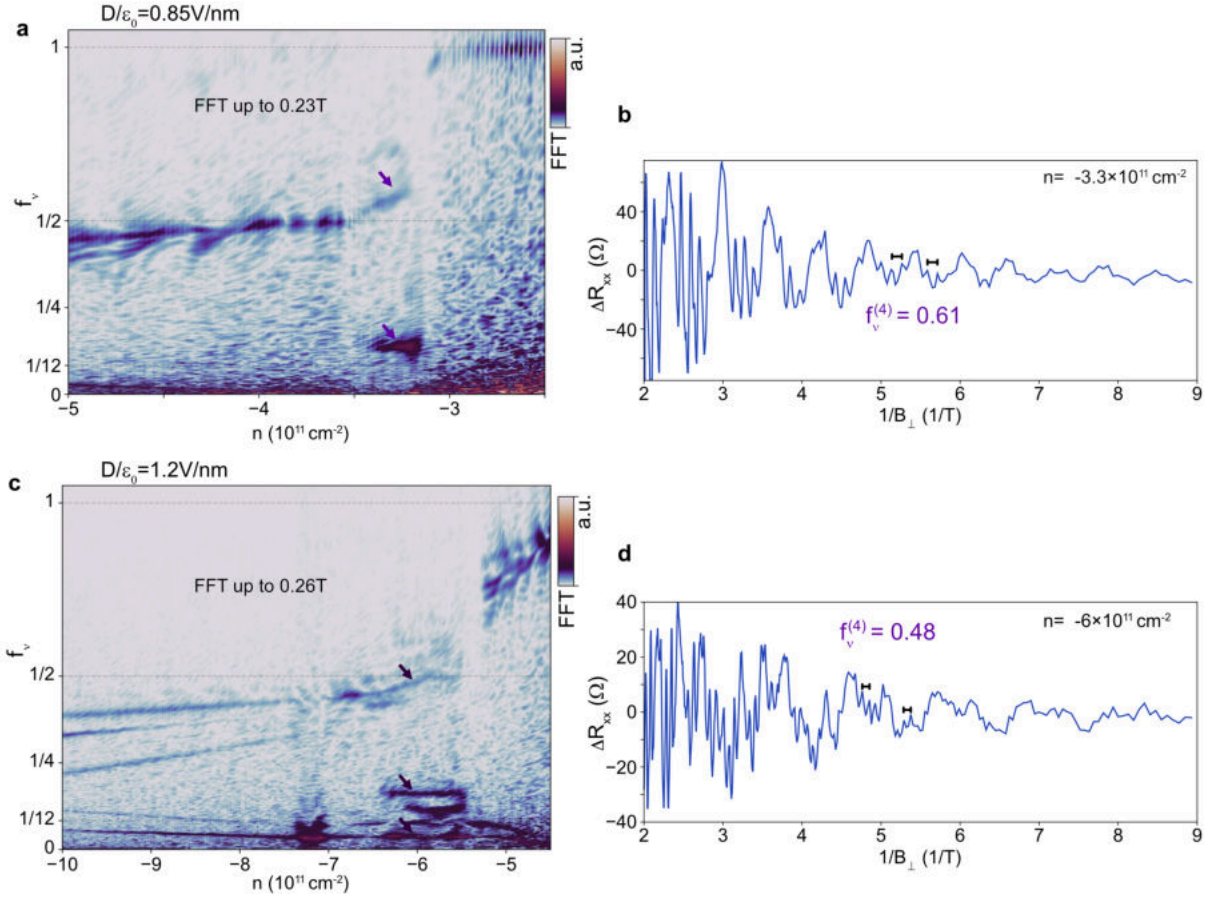
Extended Data Fig. 7 | Identifying FP(2, 2, 2) and FP(1, 3, 1) frequencies from the raw data. **a**, R_{xx} versus out-of-plane magnetic field B_{\perp} and doping density n measured at $D/\epsilon_0 = 1.2 \text{ V/nm}$ for a device with $|\lambda_I| \approx 1.5 \text{ meV}$. **b**, The same data as in **a**, but plotted as a function of $1/B_{\perp}$. The corresponding frequencies are marked by colored arrows and lines. **c**, Intensity peaks in f_{ν} extracted from the FFT data.



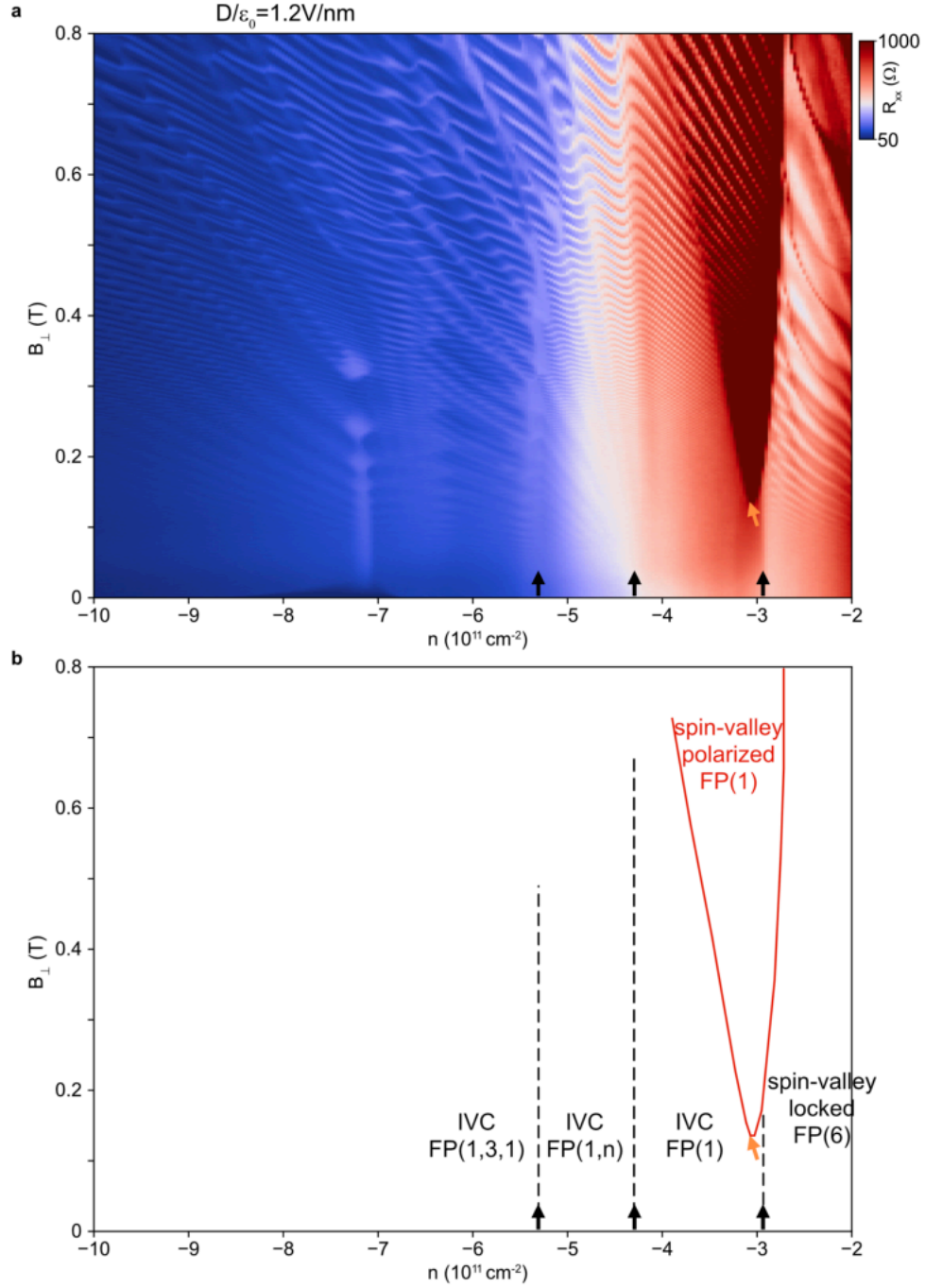
Extended Data Fig. 8 | FP(1,3) and FP(1,3,1) at $D/\epsilon_0 = 0.85 \text{ V/nm}$ and 1 V/nm , respectively. **a,b, R_{xx} versus out-of-plane magnetic field B_{\perp} and doping density n measured at $D/\epsilon_0 = 0.85 \text{ V/nm}$ (**a**) and 1 V/nm (**b**), respectively. **c,d**, Frequency-normalized Fourier transform of $R_{xx}(1/B_{\perp})$ (using data within $0.05 < B_{\perp} < 0.45 \text{ T}$) at $D/\epsilon_0 = 0.85 \text{ V/nm}$ (**c**) and 1 V/nm (**d**), respectively. **e,f**, Intensity peaks in f_{ν} extracted from the FFT data in **c** and **d**.**



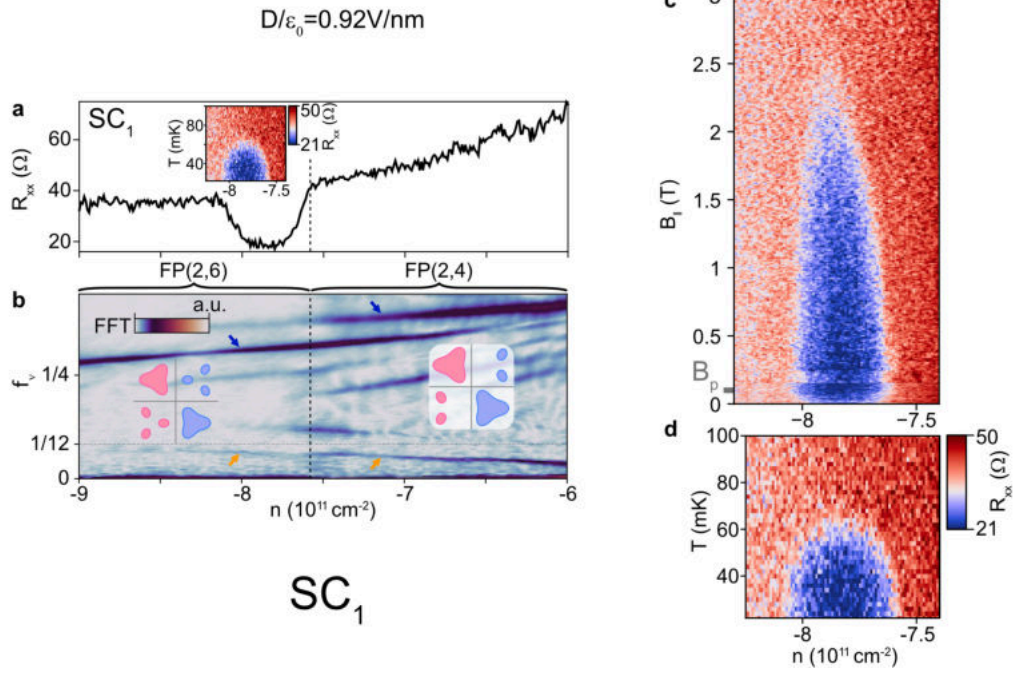
Extended Data Fig. 9 | FP(1, 3, 1) at $D/\epsilon_0 = 1.2 \text{ V/nm}$ and 1.265 V/nm . **a,b,** R_{xx} versus out-of-plane magnetic field B_{\perp} and doping density n measured at $D/\epsilon_0 = 1.2 \text{ V/nm}$ (**a**) and 1.265 V/nm (**b**), respectively. **c,d,** Frequency-normalized Fourier transform of $R_{xx}(1/B_{\perp})$ (using data within $0.05 < B_{\perp} < 0.45 \text{ T}$) at $D/\epsilon_0 = 1.2 \text{ V/nm}$ (**c**) and 1.265 V/nm (**d**), respectively. **e,f,** Intensity peaks in f_{ν} extracted from the FFT data in **c** and **d**.



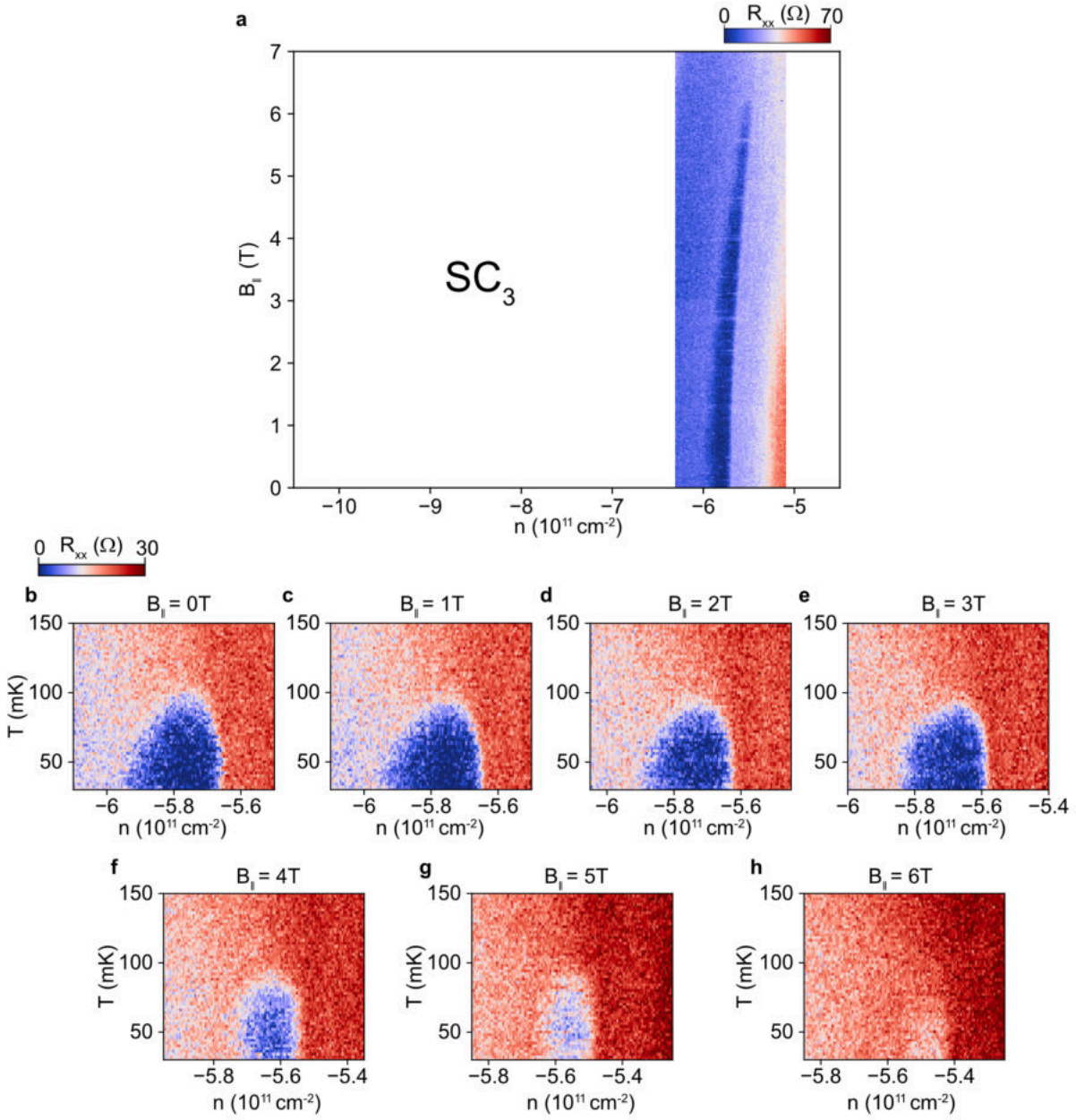
Extended Data Fig. 10 | FFT of FP(1, 3) and FP(1, 3, 1) with data at lower magnetic field. **a,c**, Frequency-normalized Fourier transform of $R_{xx}(1/B_{\perp})$ at $D/\epsilon_0 = 0.85 \text{ V/nm}$ (**a**) and 1.2 V/nm (**c**), respectively. The R_{xx} data are used up to 0.23 T and 0.26 T respectively. **b,d**, R_{xx} variation ΔR_{xx} as a function $1/B_{\perp}$ measured at $n = -3.3 \times 10^{11} \text{ cm}^{-2}$, $D/\epsilon_0 = 0.85 \text{ V/nm}$ (**b**) and $n = -6 \times 10^{11} \text{ cm}^{-2}$, $D/\epsilon_0 = 1.2 \text{ V/nm}$ (**d**), respectively.



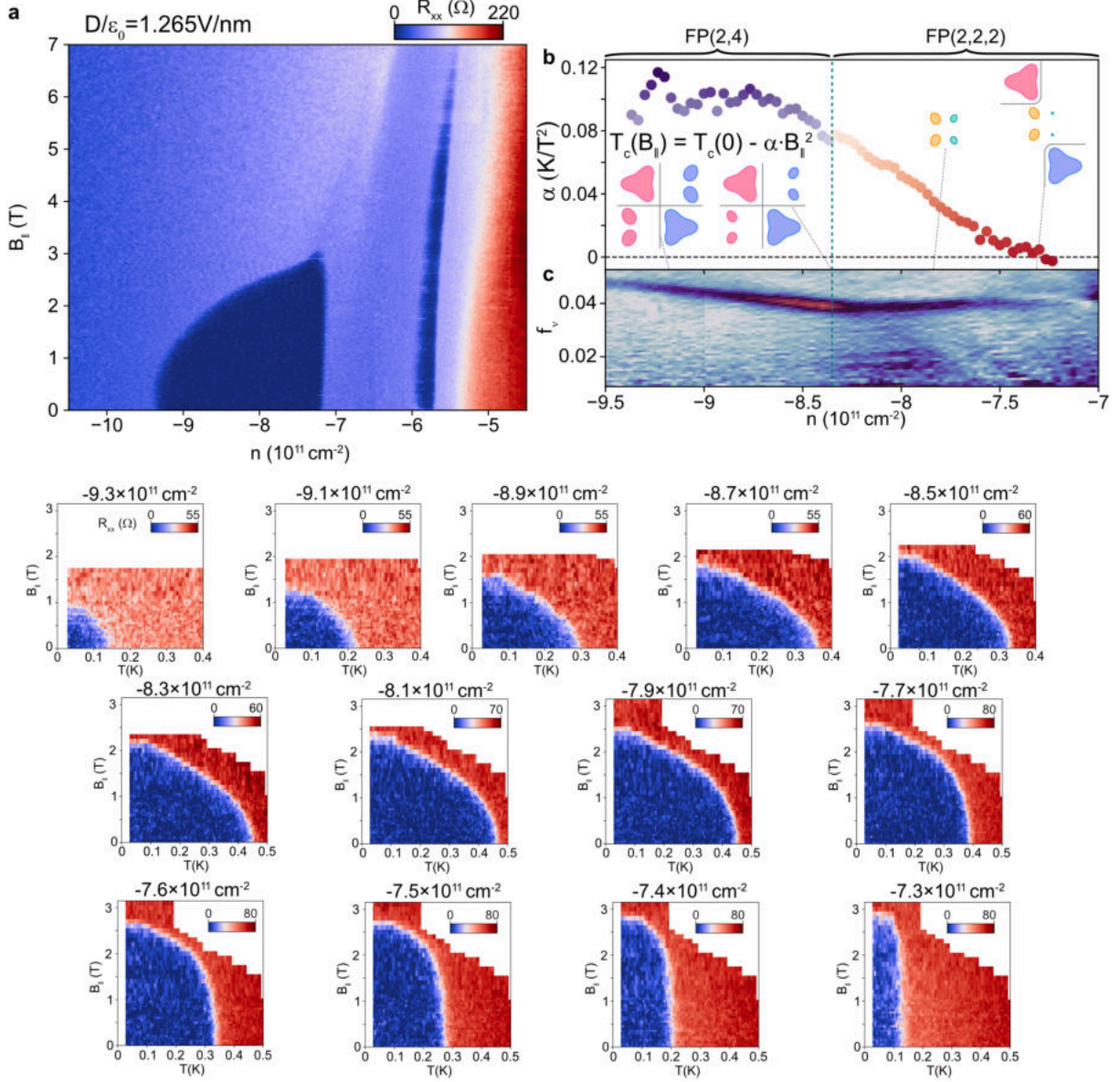
Extended Data Fig. 11 | Evolution of phase boundaries as a function of B_{\perp} . **a**, R_{xx} versus out-of-plane magnetic field B_{\perp} and doping density n measured at $D/\epsilon_0 = 1.2 \text{ V/nm}$ for a device with $|\lambda_I| \approx 1.5 \text{ meV}$. Phase boundaries are marked out in **b**. The black arrows and dashed lines mark the phase boundaries that are not sensitive to B_{\perp} , suggestive of inter-valley coherence with little or no net orbital moments. The red line draws the phase boundary of the spin-valley polarized FP(1); the boundary grows (orange arrow) with B_{\perp} due to large orbital moments.



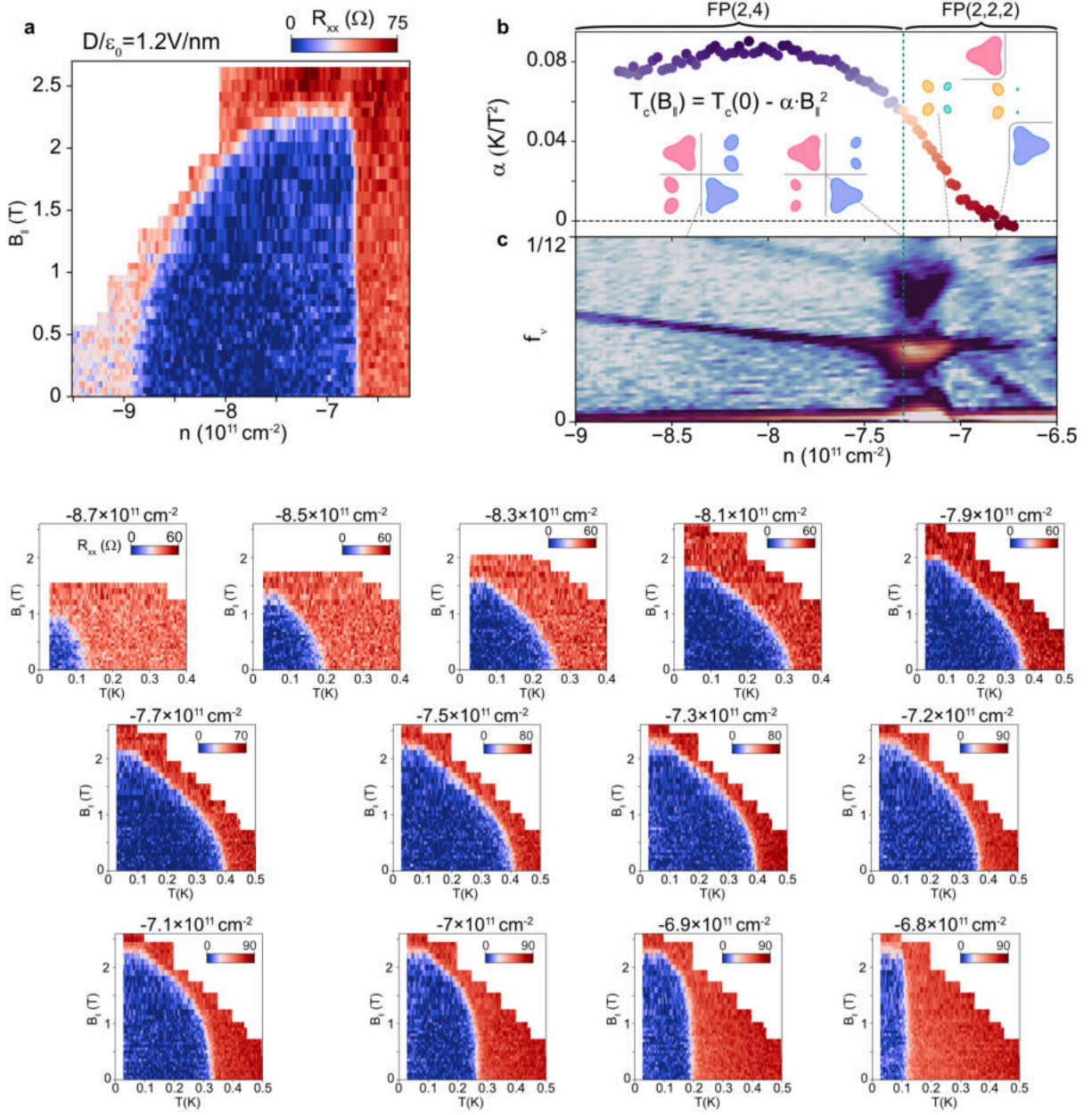
Extended Data Fig. 12 | B_{\parallel} dependence of SC_1 . **a**, R_{xx} versus n measured at $D/\epsilon_0 = 0.92 \text{ V/nm}$. Inset shows R_{xx} versus n and temperature for the superconducting dome SC_1 . **b**, Frequency-normalized FFT of $R_{xx}(1/B_{\perp})$ over the same doping range as in **a**. **c,d**, n -dependent R_{xx} versus in-plane magnetic field (**c**) or versus temperature (**d**), showing the disappearance of SC_1 . The grey bar marks the Pauli limit B_p .



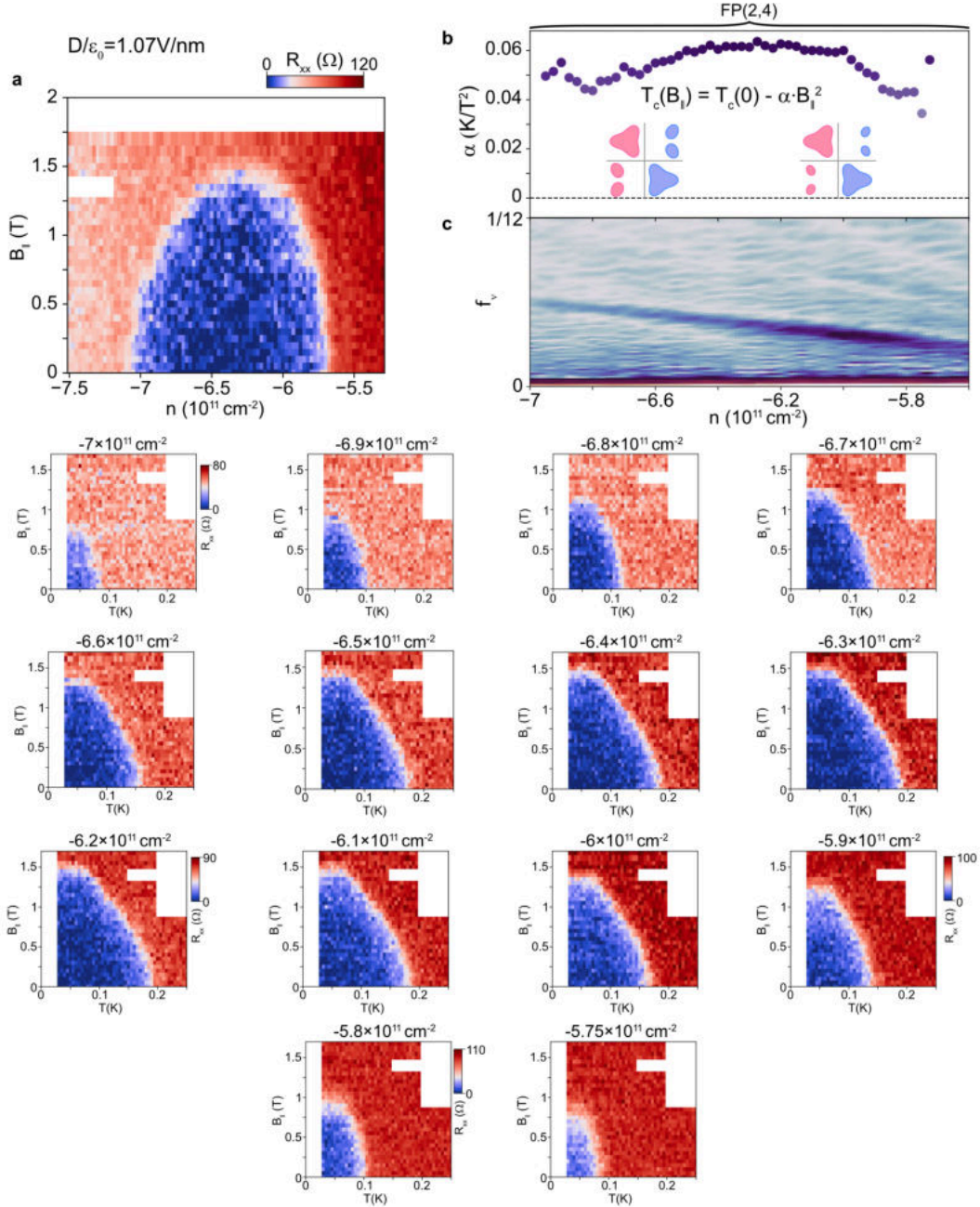
Extended Data Fig. 13 | B_{\parallel} dependence of SC_3 . **a**, R_{xx} versus doping density n and in-plane magnetic field B_{\parallel} showing the evolution of SC_3 . **b-h**, R_{xx} versus doping density n and temperature measured from $B_{\parallel} = 0 \text{ T}$ (**b**) to 6 T (**h**), 1 T increment step.



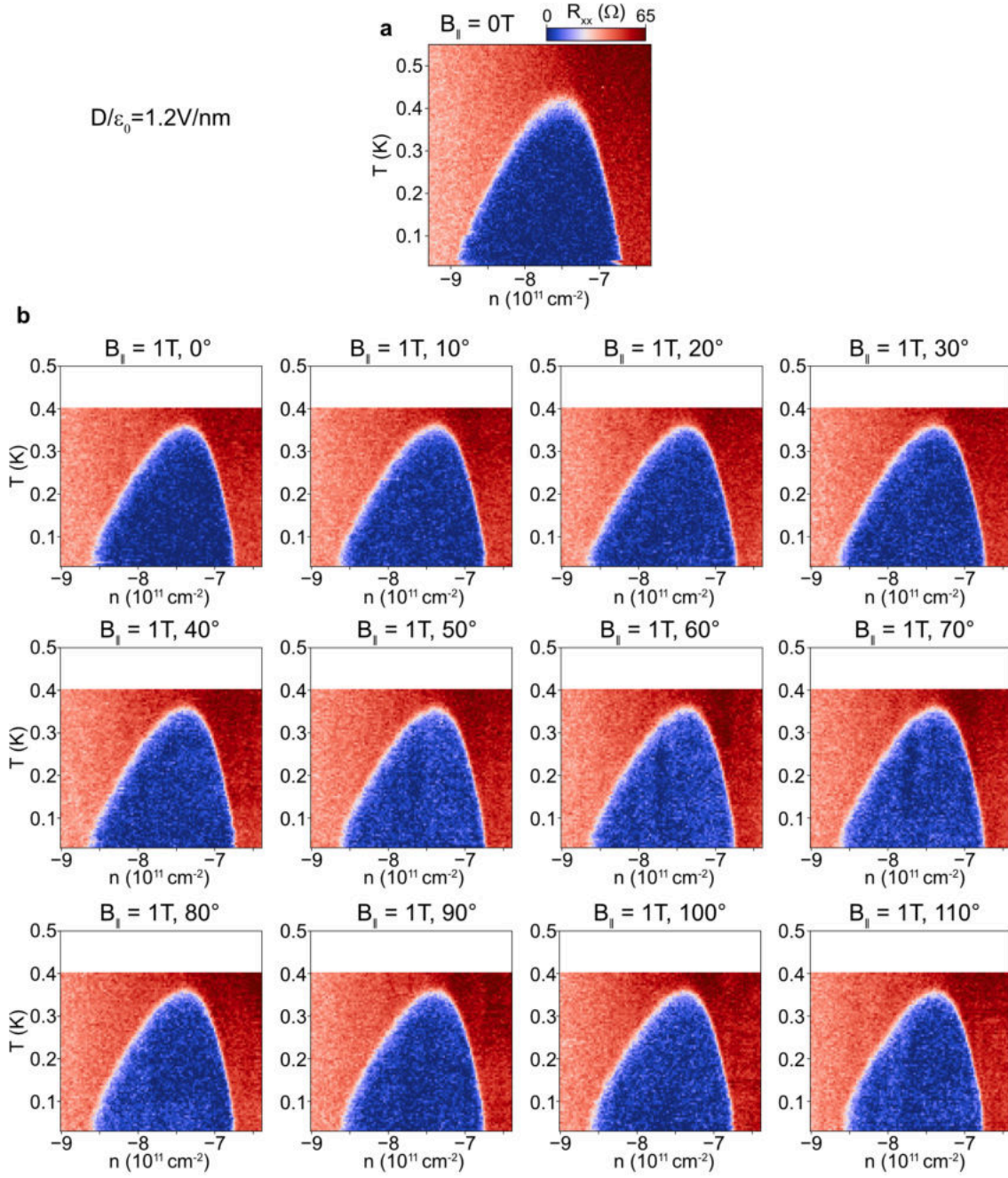
Extended Data Fig. 14 | B_{\parallel} dependence of SC_2 at $D/\epsilon_0 = 1.265 \text{ V/nm}$. **a**, R_{xx} versus doping and B_{\parallel} focusing around SC_2 at $D/\epsilon_0 = 1.265 \text{ V/nm}$. **b**, Fitting coefficient α versus doping density n for SC_2 at the same D . **c**, Frequency-normalized Fourier transform of $R_{xx}(1/B_{\perp})$ over the same doping range as in **b**, focusing around low frequencies representing the two types of trigonal-warping pockets. Bottom panels show R_{xx} versus temperature and B_{\parallel} at different doping for $D/\epsilon_0 = 1.265 \text{ V/nm}$.



Extended Data Fig. 15 | B_{\parallel} dependence of SC_2 at $D/\epsilon_0 = 1.2 \text{ V/nm}$. **a**, R_{xx} versus doping and B_{\parallel} focusing around SC_2 at $D/\epsilon_0 = 1.2 \text{ V/nm}$. **b**, Fitting coefficient α versus doping density n for SC_2 at the same D . **c**, Frequency-normalized Fourier transform of $R_{xx}(1/B_{\perp})$ over the same doping range as in **b**, focusing around low frequencies representing the two types of trigonal-warpping pockets. Bottom panels show R_{xx} versus temperature and B_{\parallel} at different doping for $D/\epsilon_0 = 1.2 \text{ V/nm}$.



Extended Data Fig. 16 | B_{\parallel} dependence of SC₂ at $D/\epsilon_0 = 1.07 \text{ V/nm}$. **a**, R_{xx} versus doping and B_{\parallel} focusing around SC₂ at $D/\epsilon_0 = 1.07 \text{ V/nm}$. **b**, Fitting coefficient α versus doping density n for SC₂ at the same D . **c**, Frequency-normalized Fourier transform of $R_{xx}(1/B_{\perp})$ over the same doping range as in **b**, focusing around low frequencies representing the single type of trigonal-warping pockets without nematic redistribution of holes. Bottom panels show R_{xx} versus temperature and B_{\parallel} at different doping at $D/\epsilon_0 = 1.07 \text{ V/nm}$. At this D field, SC₂ doesn't onset from FP(2, 2, 2). The rapidly changing α with diminished values are accordingly absent.

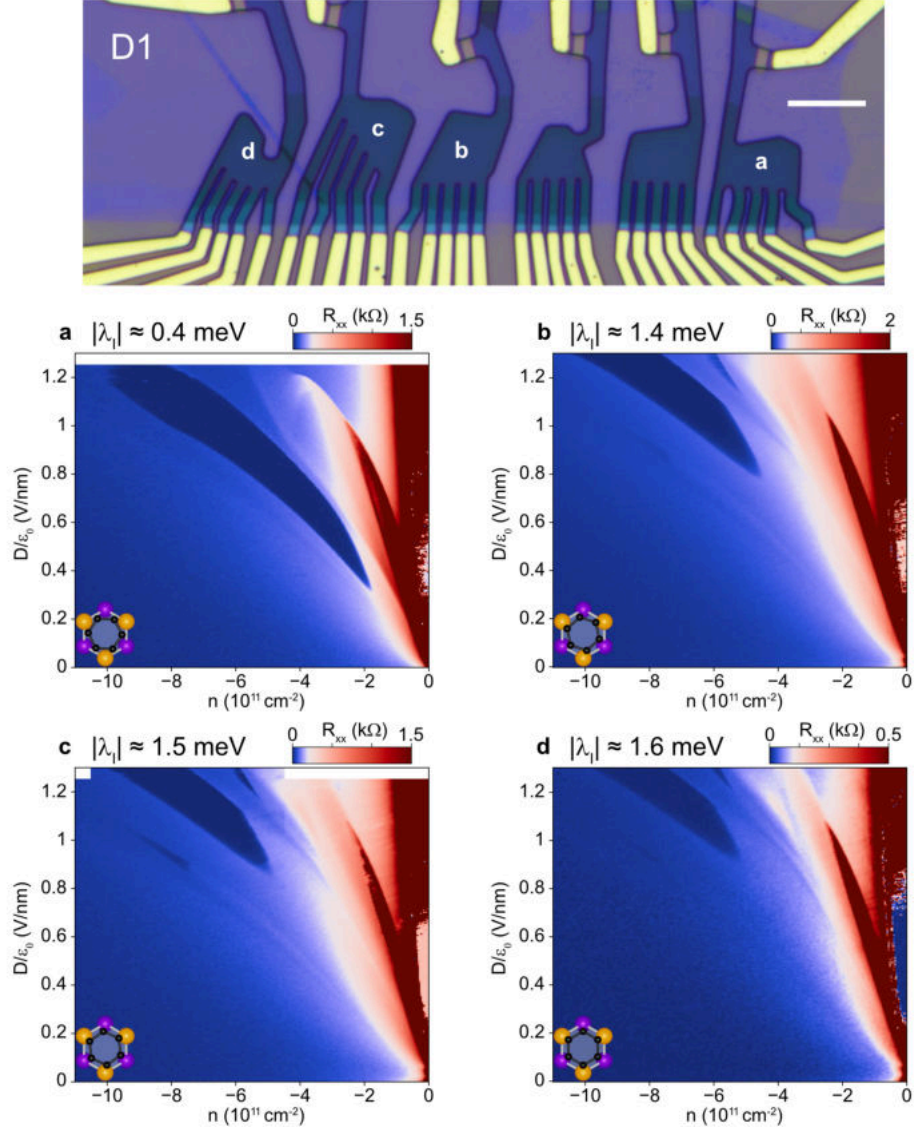


Extended Data Fig. 17 | Isotropic B_{\parallel} dependence of SC_2 . **a**, R_{xx} versus n and temperature showing SC_2 at $D/\epsilon_0 = 1.2 \text{ V/nm}$. **b**, R_{xx} versus n and temperature showing SC_2 , measured with an in-plane magnetic field $B_{\parallel} = 1 \text{ T}$, at different in-plane angles. The depairing of SC_2 is isotropic along different B_{\parallel} directions.

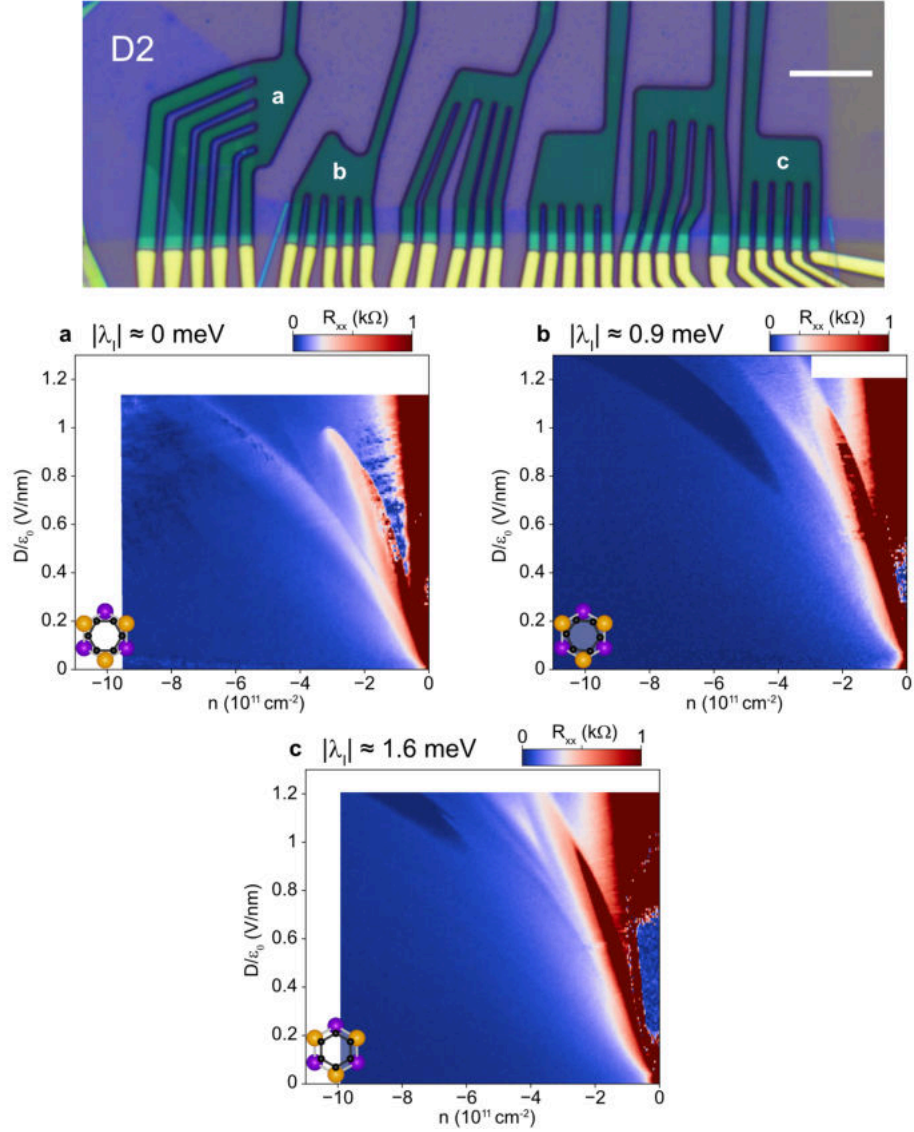
Supplementary Information:

Twist-Programmable Superconductivity in Spin-Orbit Coupled Bilayer Graphene

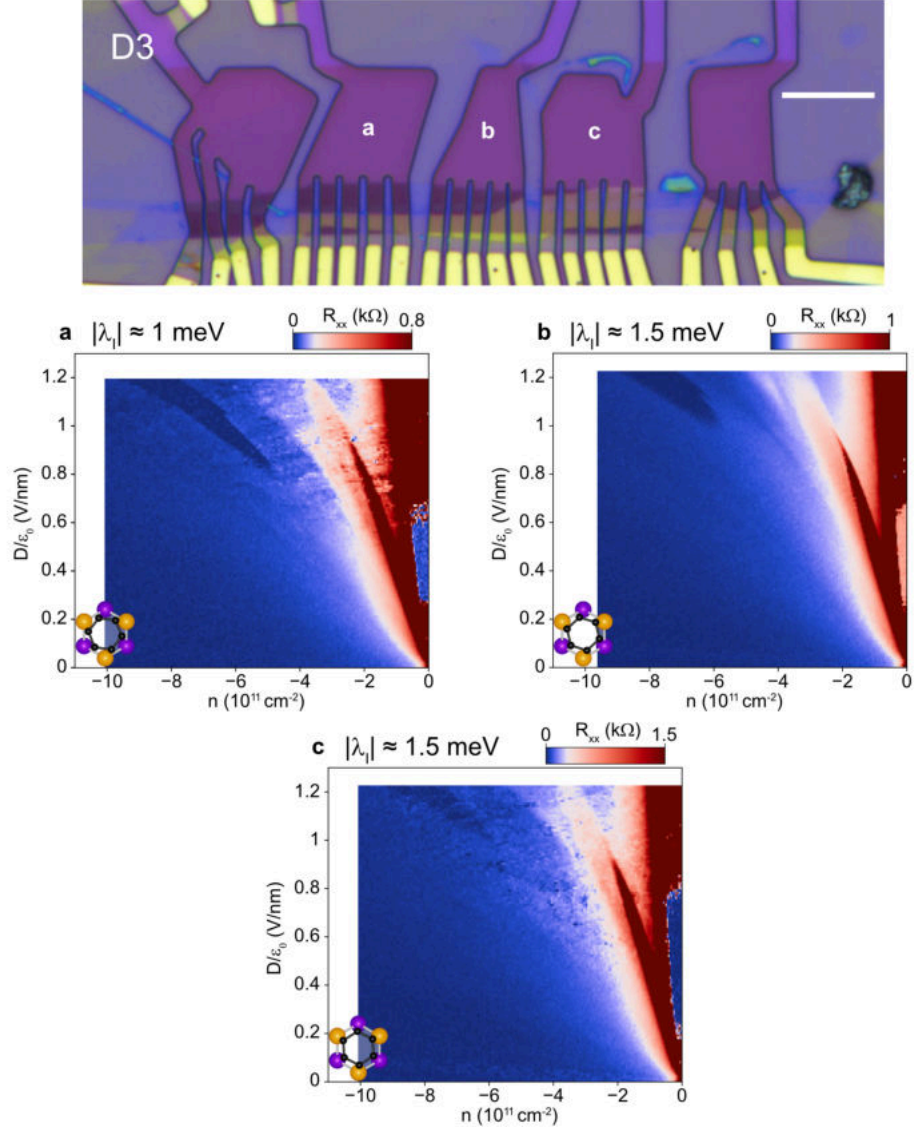
Yiran Zhang, Gal Shavit, Huiyang Ma, Youngjoon Han, Chi Wang Siu, Ankan Mukherjee, Kenji Watanabe, Takashi Taniguchi, David Hsieh, Cyprian Lewandowski, Felix von Oppen, Yuval Oreg, and Stevan Nadj-Perge



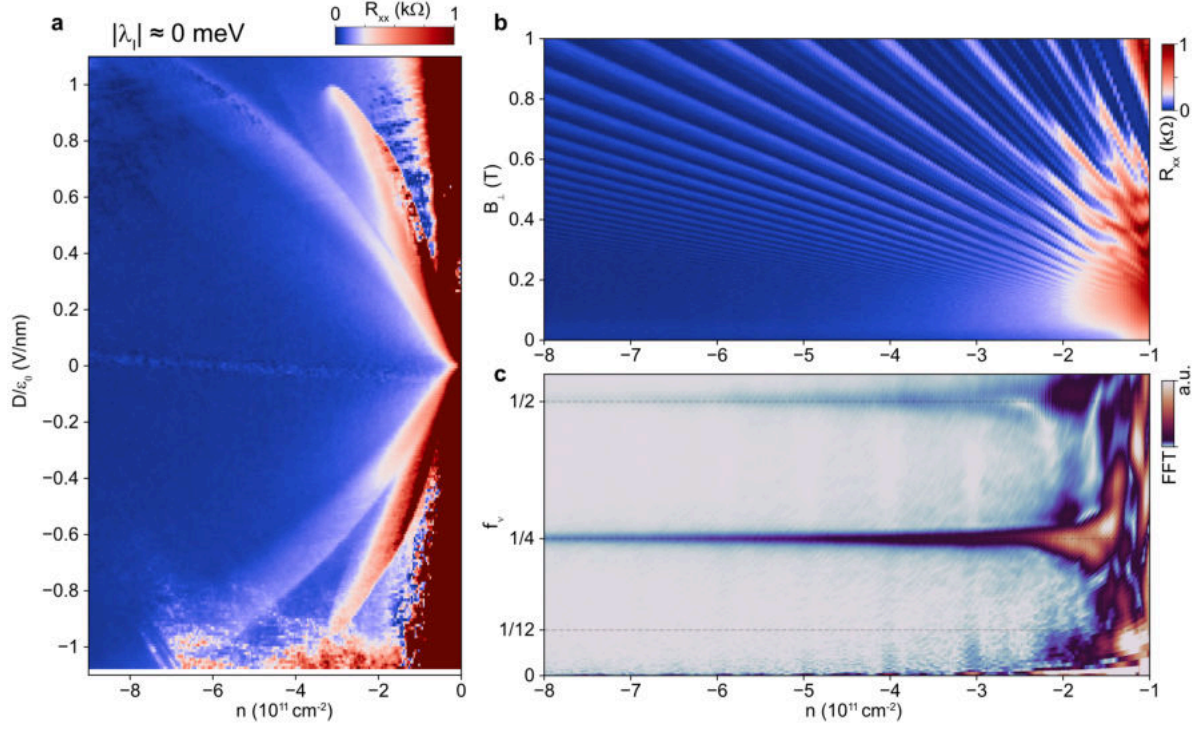
Supplementary Information Fig. 1 | n - D phase diagrams for the device set D1. **a–d**, R_{xx} versus doping density n and displacement field D for the device set D1 with Ising strength $|\lambda_I| \approx 0.4 \text{ meV}$ (**a**), 1.4 meV (**b**), 1.5 meV (**c**), and 1.6 meV (**d**), respectively. The devices are marked by the corresponding labels in the optical image. Scale bar corresponds to $10 \mu\text{m}$.



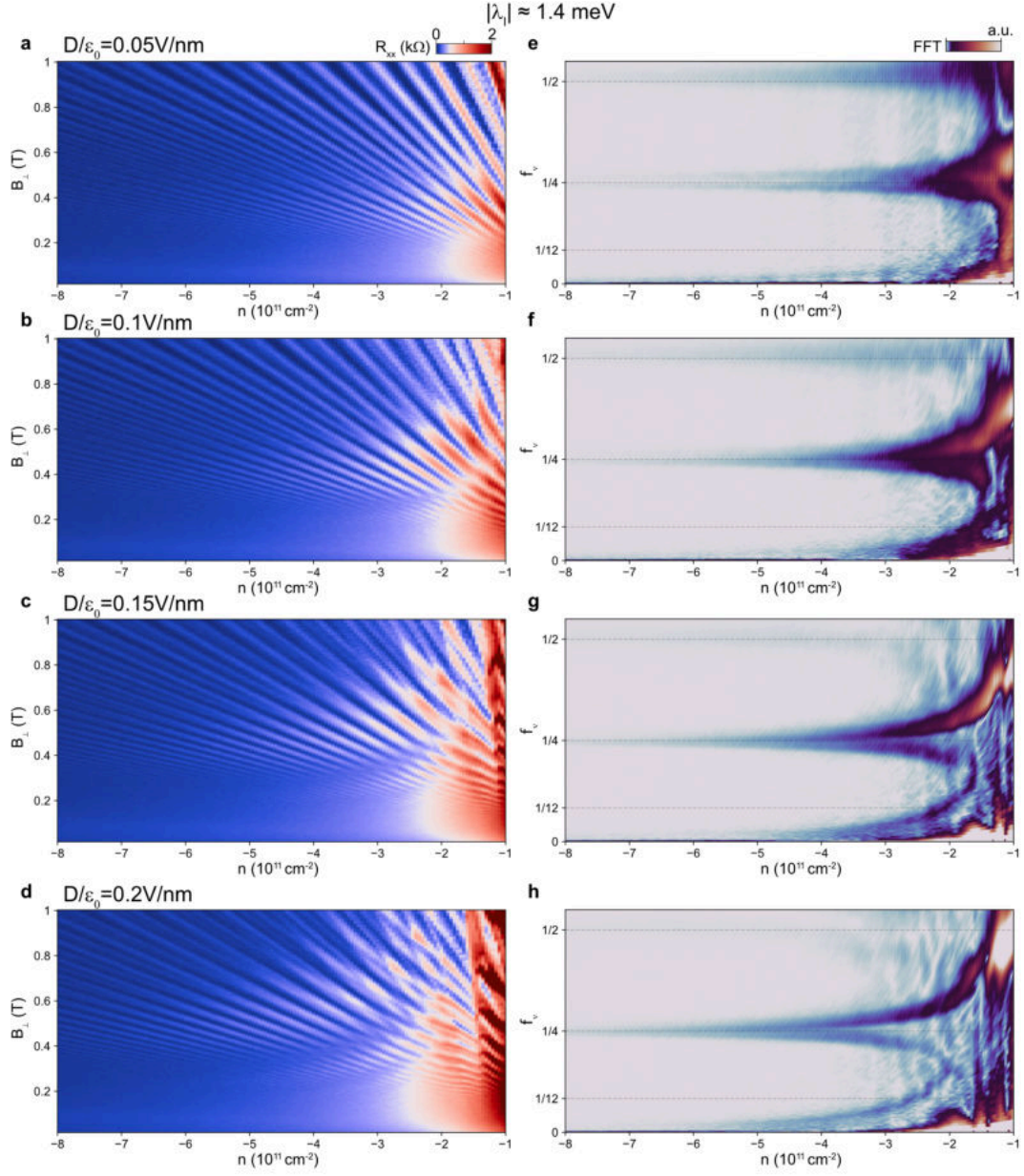
Supplementary Information Fig. 2 | n - D phase diagrams for the device set D2. **a–c**, R_{xx} versus doping density n and displacement field D for the device set D2 with Ising strength $|\lambda_I| \approx 0$ meV (**a**), 0.9 meV (**b**), and 1.6 meV (**c**), respectively. The devices are marked by the corresponding labels in the optical image. Scale bar corresponds to $10\mu\text{m}$.



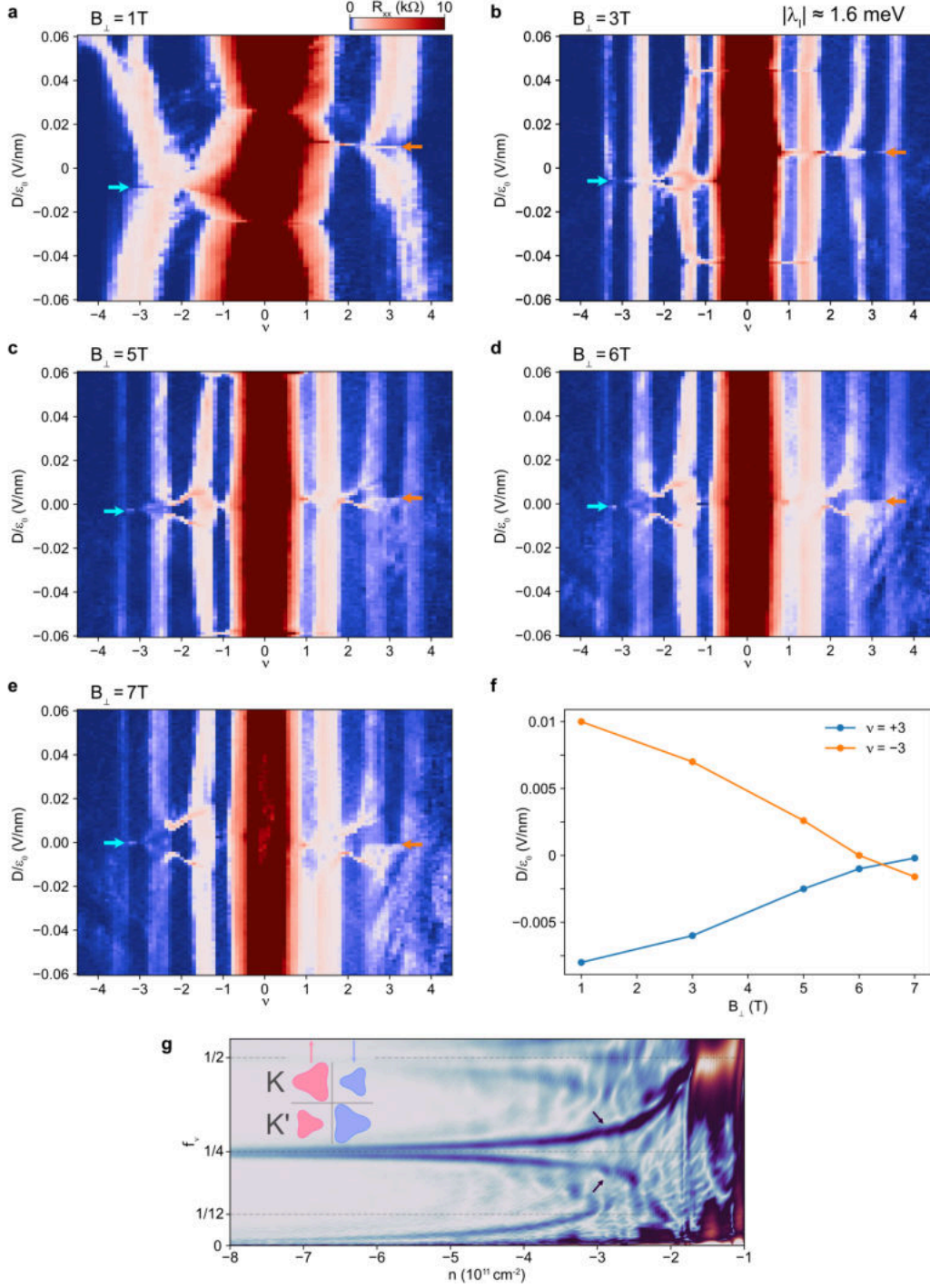
Supplementary Information Fig. 3 | n - D phase diagrams for the device set D3. **a–c**, R_{xx} versus doping density n and displacement field D for the device set D3 with Ising strength $|\lambda_I| \approx 1$ meV (**a**), 1.5 meV (**b**), and 1.5 meV (**c**), respectively. The devices are marked by the corresponding labels in the optical image. Scale bar corresponds to $10\mu\text{m}$.



Supplementary Information Fig. 4 | Phase diagram for a minimal Ising device. **a**, R_{xx} versus doping density n and displacement field D for the first device in the device set D2, with an Ising SOC strength $|\lambda_I| \approx 0 \text{ meV}$. **b**, R_{xx} versus B_{\perp} and doping n measured at $D/\epsilon_0 = 0.2 \text{ V/nm}$. **c**, FFT of $R_{xx}(1/B_{\perp})$ versus n and f_v , where f_v denotes the quantum oscillation frequency normalized to the Luttinger volume.



Supplementary Information Fig. 5 | Quantum oscillations for Ising extraction at low D fields. **a–d**, R_{xx} versus out-of-plane magnetic field B_{\perp} and doping density n measured from $D/\epsilon_0 = 0.05$ V/nm to 0.2 V/nm for a device with $|\lambda_I| \approx 1.4$ meV. **e–h**, The corresponding normalized FFT analysis.



Supplementary Information Fig. 6 | Comparing Landau level crossing and quantum oscillations for Ising SOC value. **a–e**, R_{xx} versus $\nu = 2\pi\ell_B^2 n$ (ℓ_B is the Landau magnetic length) and D field at $B_{\perp} = 1\text{ T}$, 3 T , 6 T , 6 T , and 7 T , respectively. **f**, B_{\perp} -dependent transitions against D . The Ising SOC is calculated from the crossing point of the $\nu = \pm 3$ lines. **g**, FFT of $R_{xx}(1/B_{\perp})$ versus n and f_{ν} for a device with $|\lambda_I| \approx 1.6\text{ meV}$ measured at $D/\epsilon_0 = 0.2\text{ V/nm}$.

1 Comparing SC₁, SC₂, and SC₃ with the previous work in BLG

We first summarize the experimental trends in our manuscript: (i) SC₁ and SC₃ are only observed in the devices with large Ising SOC; (ii) SC₂ features the largest phase space: with larger Ising SOC, SC₂ onsets at higher D fields and has higher T_c . Compared with the previous work on BLG/WSe₂, the BLG/WSe₂ device in Ref. 17 features an Ising SOC $|\lambda_I| \approx 0.7$ meV, the onset D field of which is roughly $D/\epsilon_0 = 0.5$ V/nm and the optimal T_c is roughly 300 mK. The observation is aligned with our phase diagram of SC₂: an intermediate $|\lambda_I|$ gives an intermediate optimal T_c ; SC₂ onsets at an intermediate D field.

For the case of intrinsic BLG⁴, equivalent to zero $|\lambda_I|$, superconductivity doesn't show up at zero magnetic field. Given the experimental trend in our manuscript (Fig. 2f), SC₂ with small enough Ising will have a critical temperature approaching zero. SI Fig. 4a shows the n - D phase diagram measured from a device with negligible Ising SOC. Despite the presence of WSe₂, Ising SOC is minimal due to the angle alignment. The n - D phase diagram is overall symmetric over the sign of D , consistent with the assignment that Ising is negligible in this device¹⁷. For the negligible Ising case, there is no superconductivity at the lowest accessible electron temperature ~ 30 mK. The result is consistent with the Ising trend (Fig. 2e,f) and is also consistent with the case of intrinsic BLG⁴ where Ising SOC is zero.

Both in-plane magnetic field and Ising SOC favor the formation of superconductivity in BLG. However, it is likely that in-plane magnetic field favors a spin-polarized normal state, while Ising SOC favors a spin-valley locked normal state (with the complication of Hund's coupling). Thus, the resulting superconductivity could be quite different.

2 Continuum model of BLG and quantifying Ising SOC

The low-energy continuum model largely follows the parameters from Ref. 17 and is commonly used to describe BLG³⁴. A perpendicular displacement field D generates a potential difference $u = -d_\perp D/\epsilon_{\text{BLG}}$ between the top and bottom layers. Here $d_\perp = 0.33$ nm is the interlayer distance and $\epsilon_{\text{BLG}} \sim 4.3$ is the relative permittivity of bilayer graphene. A continuum approximation of the band structure returns a Hamiltonian of the form

$$H_0 = \sum_{\xi=\pm} \sum_{\mathbf{k}} \psi_{\xi}^{\dagger}(\mathbf{k}) h_{0,\xi}(\mathbf{k}) \psi_{\xi}(\mathbf{k}), \quad h_{0,\xi}(\mathbf{k}) = \begin{pmatrix} u/2 & v_0 \Pi^{\dagger} & -v_4 \Pi^{\dagger} & -v_3 \Pi \\ v_0 \Pi & \Delta' + u/2 & \gamma_1 & -v_4 \Pi^{\dagger} \\ -v_4 \Pi & \gamma_1 & \Delta' - u/2 & v_0 \Pi^{\dagger} \\ -v_3 \Pi^{\dagger} & -v_4 \Pi & v_0 \Pi & -u/2 \end{pmatrix} \quad (4)$$

where $\Pi = (\xi k_x + i k_y)$ and $v_i \equiv \frac{\sqrt{3}a}{2} \gamma_i$. Here, $\xi = \pm 1$ indicates the valley that has been expanded about: $\mathbf{K}, \mathbf{K}' = (\xi 4\pi/3a, 0)$ with $a = 0.246$ nm the lattice constant of monolayer graphene. The 4×4 matrix $h_{\xi}(\mathbf{k})$ is expressed in the sublattice/layer basis corresponding to creation/annihilation operators of the form $\psi_{\xi}(\mathbf{k}) = (\psi_{\xi,A1}(\mathbf{k}), \psi_{\xi,B1}(\mathbf{k}), \psi_{\xi,A2}(\mathbf{k}), \psi_{\xi,B2}(\mathbf{k}))^T$, where A/B indicate the

sublattice, 1, 2 indicate the layer, and the momentum \mathbf{k} is measured relative to \mathbf{K}_ξ (indices denoting the spin degrees of freedom have been suppressed). It will sometimes be convenient to express the Hamiltonian in terms of the spinors $\psi(\mathbf{k}) = (\psi_+(\mathbf{k}), \psi_-(\mathbf{k}))^T$.

The common values quoted for the five parameters entering the continuum model in Eq. (4) are $\gamma_0 = 2.61$ eV (intralayer nearest-neighbor tunneling), $\gamma_1 = 361$ meV (leading interlayer tunneling), $\gamma_3 = 283$ meV (also known as trigonal warping term), $\gamma_4 = 138$ meV, and $\Delta' = 15$ meV (potential difference between dimer and non-dimer sites)⁵⁴.

WSe₂ adjacent to BLG induces SOC via virtual tunnelling^{11,14,55}:

$$H_{\text{SOC}} = \sum_{\xi=\pm} \sum_{\mathbf{k}} \psi_\xi^\dagger(\mathbf{k}) h_{\text{SOC},\xi} \psi_\xi(\mathbf{k}), \quad h_{\text{SOC},\xi}(\mathbf{k}) = \mathcal{P}_1 \left[\frac{\lambda_I}{2} \xi s^z + \frac{\lambda_R}{2} (\xi \sigma^x s^y - \sigma^y s^x) \right], \quad (5)$$

where the Pauli matrices σ^i and s^i , $i = x, y, z$, respectively act on sublattice and spin degrees of freedom. The operator \mathcal{P}_1 projects onto the top graphene sheet, i.e., only the sites A1 and B1: $\mathcal{P}_1 = \text{diag}(\mathbb{1}_{2 \times 2}, \mathbb{0}_{2 \times 2})$ in the layer/sublattice basis used to express $h_{0,\xi}(\mathbf{k})$ in (4). The parameters λ_I and λ_R quantify the strength of the Ising and Rashba SOC.

Turning on a displacement field D , a gap opens at charge neutrality and the van Hove singularities move apart in energy. The low-energy states near \mathbf{K} and \mathbf{K}' become strongly layer- and sublattice-polarized. That is, the low-energy wavefunctions near charge neutrality and under a large D field are strongly localized on the “non-dimer sites” of BLG. The layer- and sublattice polarization of the low-energy wavefunctions near the \mathbf{K} , \mathbf{K}' points has important consequences for SOC induced by the transition metal dichalcogenide (TMD). Rashba SOC does not act effectively in the low-energy theory because it is off-diagonal in the sublattice degree of freedom. It therefore induces a splitting only at second order in degenerate perturbation theory, with $\lambda_R^{\text{eff}} \sim (\lambda_R v_0 k)^2 / (\gamma_1^2 u)$ with u the interlayer potential⁵⁶ (see also SI, section 2 and SI Fig. 10). By contrast, the Ising SOC acts effectively in the subspace of sublattice- and layer-polarized wavefunctions.

With the parameters for continuum model and SOC, density of states within each valley can thus be calculated. The band structure returns population within the four spin-valley flavors for a given doping density. Accordingly, the splitting of quantum oscillation frequencies is obtained. Ising SOC corresponds to the best fit to the doping-dependent FFT splitting at different D (Extended Data Fig. 2).

3 Importance of interband superconductivity in BLG

Much of the experimental observations in BLG proximitized by WSe₂ may be understood in the context of multiband superconductivity. Here, the bands correspond to the majority and minority bands are split by the Ising spin-orbit coupling (ISOC), possibly further enhanced by electron-

electron interactions. It is the coupling between these two sectors (majority and minority bands) in the Cooper channel, i.e., pair scattering between the bands, that is crucial to interpreting the experimental results.

The delayed onset (in terms of higher displacement fields) of superconductivity in the main dome when the spin-orbit coupling is increased is elucidated in Sec. 6. When the density of states (DOS) of both bands is high near the Fermi level, screening of the bare Coulomb repulsion becomes much more efficient, enabling superconductivity mediated by some retarded attraction. As the bands are further split by the ISOC, *the band-concurrent high DOS region is pushed to higher displacement fields*. This is illustrated in SI Fig. 7.

The large variance in the behavior of the different superconducting region when an in-plane magnetic field is introduced, as manifested in varying Pauli-limit-violation ratios, is discussed in Sec. 7. We consider the effect of a Zeeman term in *gradually decoupling the majority and minor bands in the Cooper channel*. Analysing the energetics of spin magnetization in the presence of both ISOC and Hund's coupling, we illustrate how the main superconducting dome, where the imbalance between majority and minority carriers is the greatest, becomes most vulnerable to this effect. We further demonstrate the experimental trends are well understood within our modeling. We stress that the Zeeman coupling is not assumed to have any pair-breaking role, the effect we consider is purely due to “shifting” interaction strength from the intraband part of the coupling matrix to the interband part. In Sec. 8, we consider a more direct depairing model and contrast with the results of the proposed mechanism here.

Finally, we note that in our analysis we do not specify or rely on what is the pairing glue which mediates superconductivity. We remain agnostic with regards to its origin, as well as its intra-band/interband nature, which do not modify our conclusions.

4 Variational Hartree-Fock

We begin by calculating the the non-interacting band structure of biased Bernal-stacked bilayer graphene. Expanded around the valley K/K' points in momentum space, the Hamiltonian is ³⁴

$$H_{BLG} = \sum_{\mathbf{k}, \tau, s} c_{\tau s \mathbf{k}}^\dagger h_\tau(\mathbf{k}) c_{\tau s \mathbf{k}}, \quad (6)$$

with $c_{\tau s \mathbf{k}} = (A_{1, \tau s \mathbf{k}}, B_{1, \tau s \mathbf{k}}, A_{2, \tau s \mathbf{k}}, B_{2, \tau s \mathbf{k}})^T$, where $X_{i, \tau s \mathbf{k}}$ annihilates an electron on sub-lattice X in layer i , with spin s , and momentum \mathbf{k} near the valley τ . The matrix h_τ is given by

$$h_\tau(\mathbf{k}) = \begin{pmatrix} \frac{U}{2} & v_0 \Pi_\tau^* & -v_4 \Pi_\tau^* & -v_3 \Pi_\tau \\ v_0 \Pi_\tau & \frac{U}{2} + \Delta' & \gamma_1 & -v_4 \Pi_\tau^* \\ -v_4 \Pi_\tau & \gamma_1 & -\frac{U}{2} + \Delta' & v_0 \Pi_\tau^* \\ -v_3 \Pi_\tau^* & -v_4 \Pi_\tau & v_0 \Pi_\tau & -\frac{U}{2} \end{pmatrix}, \quad (7)$$

with $\Pi_\tau = \tau k_x + i k_y$, and the parameters $v_i = \frac{\sqrt{3}}{2} a \gamma_i$, $a = 0.246$ nm, $\gamma_0 = 2.61$ eV, $\gamma_1 = 361$ meV, $\gamma_3 = 283$ meV, $\gamma_4 = 138$ meV, and $\Delta' = 15$ meV⁵⁴. The interlayer potential difference U is approximately $U \approx -dD/\epsilon$, where the interlayer distance is $d \approx 0.33$ nm, $\epsilon \approx 4.3$, and D is the displacement field. We diagonalize H_{BLG} at each momentum, and extract the dispersion relation of the lowest-lying valence band, which we denote by $\epsilon_{\tau,\mathbf{k}}$.

Our analysis proceeds with a phenomenological description of the underlying physics of electrons in this band in the spirit of Ref. 57, described by the 4-spinor $\Psi_{\mathbf{k}}$ of fermionic annihilation operators at momentum \mathbf{k} , with valley and spin degrees of freedom, described by Pauli matrices τ_i and s_i , respectively. We analyze the Hamiltonian,

$$H = H_0 + H_{\text{ISOC}} + H_{\text{int}}, \quad (8)$$

$$H_0 = \sum_{\mathbf{k}} \Psi_{\mathbf{k}}^\dagger \left(\epsilon_{+, \mathbf{k}} \frac{1 + \tau_z}{2} + \epsilon_{-, \mathbf{k}} \frac{1 - \tau_z}{2} \right) \Psi_{\mathbf{k}}, \quad (9)$$

$$H_{\text{ISOC}} = \sum_{\mathbf{k}} \Psi_{\mathbf{k}}^\dagger \lambda_0 \tau_z s_z \Psi_{\mathbf{k}}, \quad (10)$$

$$H_{\text{int}} = \frac{1}{\Omega} \sum_{\mathbf{q}} \left(\frac{U_C}{2} N_{\mathbf{q}} N_{-\mathbf{q}} + U_V n_{\mathbf{q}}^+ n_{-\mathbf{q}}^- + J \mathbf{S}_{\mathbf{q}}^+ \cdot \mathbf{S}_{-\mathbf{q}}^- \right), \quad (11)$$

where $N_{\mathbf{q}} = \sum_{\mathbf{k}} \Psi_{\mathbf{k}+\mathbf{q}}^\dagger \Psi_{\mathbf{k}}$, $n_{\mathbf{q}}^\pm = \sum_{\mathbf{k}} \Psi_{\mathbf{k}+\mathbf{q}}^\dagger \frac{1 \pm \tau_z}{2} \Psi_{\mathbf{k}}$, $\mathbf{S}_{\mathbf{q}}^\pm = \sum_{\mathbf{k}} \Psi_{\mathbf{k}+\mathbf{q}}^\dagger \frac{1 \pm \tau_z}{2} \mathbf{s} \Psi_{\mathbf{k}}$, and Ω is the system area. The term proportional to λ_0 is the bare Ising-type spin-orbit coupling induced in the valence band (at positive values of the electric displacement field) by the proximity to WSe₂. The structure of H_{int} is the most general form of short-range interactions which respect the symmetry of the system: time-reversal, $SU(2)$ spin symmetry (in the absence of magnetic fields or spin-orbit coupling), and the $U(1)$ charge and (approximate) valley symmetries. The interaction term proportional to U_C is a structure-less density-density interaction, which is entirely $SU(4)$ symmetric in valley-spin space, and is considered to be dominant as compared to the other two terms. The term proportional to U_V accounts for possible differences between intravalley and intervalley density-density interactions and will be set to zero throughout this work, as it is non-essential for correctly capturing the phenomenology we aim to study. Finally, J is the intervalley Hund's coupling between electron spins in opposite valleys.

Although the Ising spin-orbit coupling term H_{ISOC} explicitly breaks the flavor symmetry of the system, i.e., not all spin-valley flavors are populated equally even in the absence of interactions, the presence of non-negligible interactions in H_{int} may significantly alter the non-interacting picture. We employ a variational Hartree-Fock procedure to resolve the different flavor-resolved fillings. Our analysis thus proceeds as follows. At a given chemical potential μ , the grand-potential $\Phi = \langle H - \mu N_0 \rangle_{\text{H.F.}}$ is minimized, where $\langle \rangle_{\text{H.F.}}$ denotes the expectation value calculated using the variational wavefunction,

$$|\Psi\rangle_{\text{H.F.}} = \prod_{\tau,s} \left(\prod_{\substack{\mathbf{k} \\ \epsilon_{\mathbf{k}} > \mu_{\tau,s}}} \sum_{s'} \mathcal{U}(\tau\theta)_{ss'} \psi_{\mathbf{k},\tau,s'} \right) |\text{CN}\rangle, \quad (12)$$

where $\psi_{\tau,s,\mathbf{k}}$ annihilates an electron in valley τ and spin s in the valence band at momentum \mathbf{k} with energy $\epsilon_{\mathbf{k}}$, $|\text{CN}\rangle$ is the flavor-symmetric charge-neutral Fermi-sea, and $\mu_{\tau,s} \leq 0$ are the four variational parameters corresponding to the four spin-valley flavors. The possibility of canting in the different valleys is captured by the matrix $\mathcal{U}(\theta) = \begin{pmatrix} \cos \frac{\theta}{2} & \sin \frac{\theta}{2} \\ -\sin \frac{\theta}{2} & \cos \frac{\theta}{2} \end{pmatrix}$. Notice that full canting, i.e., alignment of the majority and minority bands according to their spin polarization corresponds to $\theta = \pi/2$, whereas spin-valley locking corresponds to $\theta = 0$ (no canting).

Obtaining the different μ_i , we calculate the flavor resolved densities $\nu_i = -\frac{1}{\Omega} \sum_{\mu_i < \epsilon_{\mathbf{k}} < 0} \mathbf{k}$, i.e., (minus) the number of \mathbf{k} points in the valence band whose energies are larger than μ_i . The total density is thus $n = \sum_i \nu_i$. The resultant Hartree-Fock Hamiltonian (up to additional constant contributions) can thus be written as

$$H_{\text{HF}} = \sum_{\tau s \mathbf{k}} \psi_{\tau s \mathbf{k}}^\dagger (\epsilon_{\tau \mathbf{k}} - \mu_{\tau s}) \psi_{\tau s \mathbf{k}}. \quad (13)$$

5 Multiband superconductivity framework

The starting point we consider for analyzing superconductivity in this work is an electronic system with two bands, with each band being two-fold degenerate (in the present case due to spin). We are interested in Cooper-channel interactions, and restrict ourselves to a superconducting gap with trivial symmetry. In that case, the usual mean-field ansatz for the order parameter assumes a vector form due to the multiband nature of the problem,

$$\Delta = \begin{pmatrix} \Delta_1 \\ \Delta_2 \end{pmatrix} = \begin{pmatrix} g & g_x \\ g_x & g \end{pmatrix} \left\langle \begin{pmatrix} \frac{1}{\Omega} \sum_{\mathbf{k}} \psi_{-\mathbf{k}1+} \psi_{\mathbf{k}1-} \\ \frac{1}{\Omega} \sum_{\mathbf{k}} \psi_{-\mathbf{k}2+} \psi_{\mathbf{k}2-} \end{pmatrix} \right\rangle \equiv \hat{g}_{\text{initial}} \left\langle \begin{pmatrix} \frac{1}{\Omega} \sum_{\mathbf{k}} \psi_{-\mathbf{k}1+} \psi_{\mathbf{k}1-} \\ \frac{1}{\Omega} \sum_{\mathbf{k}} \psi_{-\mathbf{k}2+} \psi_{\mathbf{k}2-} \end{pmatrix} \right\rangle, \quad (14)$$

where Ω is the system volume, $\psi_{\mathbf{k},n,p}$ annihilates an electron with momentum \mathbf{k} , in band $n = 1, 2$, and internal flavor $p = \pm$. We assume \hat{g}_{initial} is a matrix of repulsive interactions, originating from the intrinsic (presumably Thomas-Fermi screened) Coulomb interaction. For reasons which are clarified below, we take the intraband repulsion g to be the same in both bands, though a generalization is straightforward within our analysis.

Given the form of Δ , the mean-field BCS Hamiltonian takes the form

$$H_{\text{BCS}} = \sum_{\mathbf{k},n,p} \xi_{\mathbf{k}np} \psi_{\mathbf{k}np}^\dagger \psi_{\mathbf{k}np} + \sum_{\mathbf{k}} (\Delta_1^* \psi_{-\mathbf{k}1+} \psi_{\mathbf{k}1-} + \Delta_2^* \psi_{-\mathbf{k}2+} \psi_{\mathbf{k}2-} + \text{h.c.}) + \Omega \Delta^\dagger (\hat{g}_{\text{initial}})^{-1} \Delta, \quad (15)$$

and ξ_{knp} represents the normal-state energy of the n, p band relative to the Fermi energy.

Our analysis will generally consist of three steps, detailed below.

Tolmachev-Anderson-Morel step We introduce an energy scale ω^* , below which some retarded interaction is activated. Clearly, this approach, following Tolmachev³⁰, and Morel and Anderson³¹, is another significant simplification of what should generally be an energy-dependent interaction in the Cooper channel, yet it is sufficient to illustrate all our key results. In the path-integral formalism, we integrate out the electrons with energy greater than ω^* ⁵⁸, obtaining the renormalized interaction matrix,

$$\hat{g}_{\text{TAM}}(\omega^*) = \left[(\hat{g}_{\text{initial}})^{-1} + \begin{pmatrix} \ell_1 & \\ & \ell_2 \end{pmatrix} \right]^{-1}, \quad (16)$$

where we have defined

$$\ell_n = \left\{ \int_{\omega^*}^{\infty} + \int_{-\infty}^{-\omega^*} \right\} d\xi \frac{\mathcal{N}_n(\xi)}{|\xi|}, \quad (17)$$

where $\mathcal{N}_n(\xi)$ is the DOS of the n -band at a distance ξ away from the Fermi level. We may explicitly write the elements of this matrix,

$$\hat{g}_{\text{TAM}}(\omega^*) = \begin{pmatrix} \frac{g + \ell_2(g^2 - g_x^2)}{1 + g(\ell_1 + \ell_2) + (g^2 - g_x^2)\ell_1\ell_2} & \frac{g_x}{1 + g(\ell_1 + \ell_2) + (g^2 - g_x^2)\ell_1\ell_2} \\ \frac{g_x}{1 + g(\ell_1 + \ell_2) + (g^2 - g_x^2)\ell_1\ell_2} & \frac{g + \ell_1(g^2 - g_x^2)}{1 + g(\ell_1 + \ell_2) + (g^2 - g_x^2)\ell_1\ell_2} \end{pmatrix} \equiv \begin{pmatrix} u_1 & u_x \\ u_x & u_2 \end{pmatrix}. \quad (18)$$

For the sake of illustration, consider two limiting cases. If the different bands are decoupled, $g_x = 0$, we find

$$\hat{g}_{\text{TAM}}(\omega^*) = \begin{pmatrix} \frac{g}{1 + g\ell_1} & \\ & \frac{g}{1 + g\ell_2} \end{pmatrix}, \quad (19)$$

which is of course two instances of the single band result. Conversely, when the interband interaction is just as strong as the intraband one, $g_x = g$,

$$\hat{g}_{\text{TAM}}(\omega^*) = \frac{1}{1 + g(\ell_1 + \ell_2)} \hat{g}_{\text{initial}}, \quad (20)$$

i.e., the DOS from *both bands* contributes to the renormalization and suppression of the repulsion – a first hint at the inter-band interactions importance.

Retarded interaction We now introduce the retarded interaction in the Cooper channel. Generally, one may consider two possible scenarios. In the first, the interaction corresponds to an *intraband attraction*, so we define

$$\hat{g} = \hat{g}_{\text{TAM}}(\omega^*) - \begin{pmatrix} g_{\text{intra}} & \\ & g_{\text{intra}} \end{pmatrix}. \quad (21)$$

This is the conventional scenario, to which we refer throughout our calculations. In the second scenario, the retarded interaction scatters Cooper pairs between the bands, and it is necessary to consider *interband repulsion*, i.e.,

$$\hat{g} = \hat{g}_{\text{TAM}}(\omega^*) + \begin{pmatrix} & g_{\text{inter}} \\ g_{\text{inter}} & \end{pmatrix}. \quad (22)$$

We note that in the case of intraband interaction, one must have attraction to have any hope of finding a BCS instability, yet for interband interactions this is not the case. However, as we will demonstrate, *interband repulsion is actually more favorable to superconductivity*. This is because it adds on top of the interband renormalized repulsion u_x , instead of working against it.

Finding T_c Having recovered the interaction matrix \hat{g} , we turn to calculate the susceptibility matrix as a function of temperature,

$$\hat{\chi}(T) = \hat{g}^{-1} + \begin{pmatrix} \mathcal{D}_1(T) & \\ & \mathcal{D}_2(T) \end{pmatrix}, \quad (23)$$

where the electrons inside the ω^* shell contribute the factors (diverging at $T \rightarrow 0$),

$$\mathcal{D}_n(T) = \int_{-\omega^*}^{\omega^*} d\xi \mathcal{N}_n(\xi) \frac{\tanh \frac{\xi}{2T}}{\xi}. \quad (24)$$

The superconducting instability is identified by the singularity of the inverse-susceptibility matrix, i.e.,

$$\det [\hat{\chi}^{-1}(T_c)] = 0. \quad (25)$$

This is a transcendental equation for T_c , which generally has two solutions, of which one must choose the higher T_c , as it marks the superconducting transition.

We may explicitly derive the form of this self-consistent equation for T_c in the two cases discussed above:

1. Intraband attraction –

$$u_x^2 \mathcal{D}_1 \mathcal{D}_2 = [1 - (g_{\text{intra}} - u_1) \mathcal{D}_1] [1 - (g_{\text{intra}} - u_2) \mathcal{D}_2]. \quad (26)$$

2. Interband repulsion –

$$(u_x + g_{\text{inter}})^2 \mathcal{D}_1 \mathcal{D}_2 = [1 + u_1 \mathcal{D}_1] [1 + u_2 \mathcal{D}_2]. \quad (27)$$

The four-fold degenerate case may be of some interest (though irrelevant here considering the experimental data). If $\mathcal{D}_1 = \mathcal{D}_2 \equiv \mathcal{D}$, and $u_1 = u_2 \equiv u$, the equation for T_c looks the same for both cases above, and reads

$$(g_{\text{attraction}} - u + u_x) \mathcal{D} = 1. \quad (28)$$

It is now made even clearer, that in either case the interband interaction u_x always “assists” the retarded pairing glue. It is actually even simpler in the fully degenerate case $\ell_1 = \ell_2 \equiv \ell$,

$$\left(g_{\text{attraction}} - \frac{g - g_x}{1 + (g - g_x) \ell} \right) \mathcal{D} = 1, \quad (29)$$

so T_c is determined by the difference between the bare intraband and intraband repulsion, renormalized by the TAM mechanism.

6 Superconductivity onset dependence on Ising spin-orbit coupling

We consider the main superconducting region across the different devices, referred to as “SC₂”. Consistently, it has been shown by Fermiology measurements that the parent normal-state is mostly two-fold degenerate. In the non-interacting limit, the state is comprised of two spin-valley-locked sectors, the so-called majority and minority bands, split by an energy $\sim 2\lambda_0$. Interactions tend to modify the energy separation, and possibly induce canting, which render the spin-valley locking only approximate.

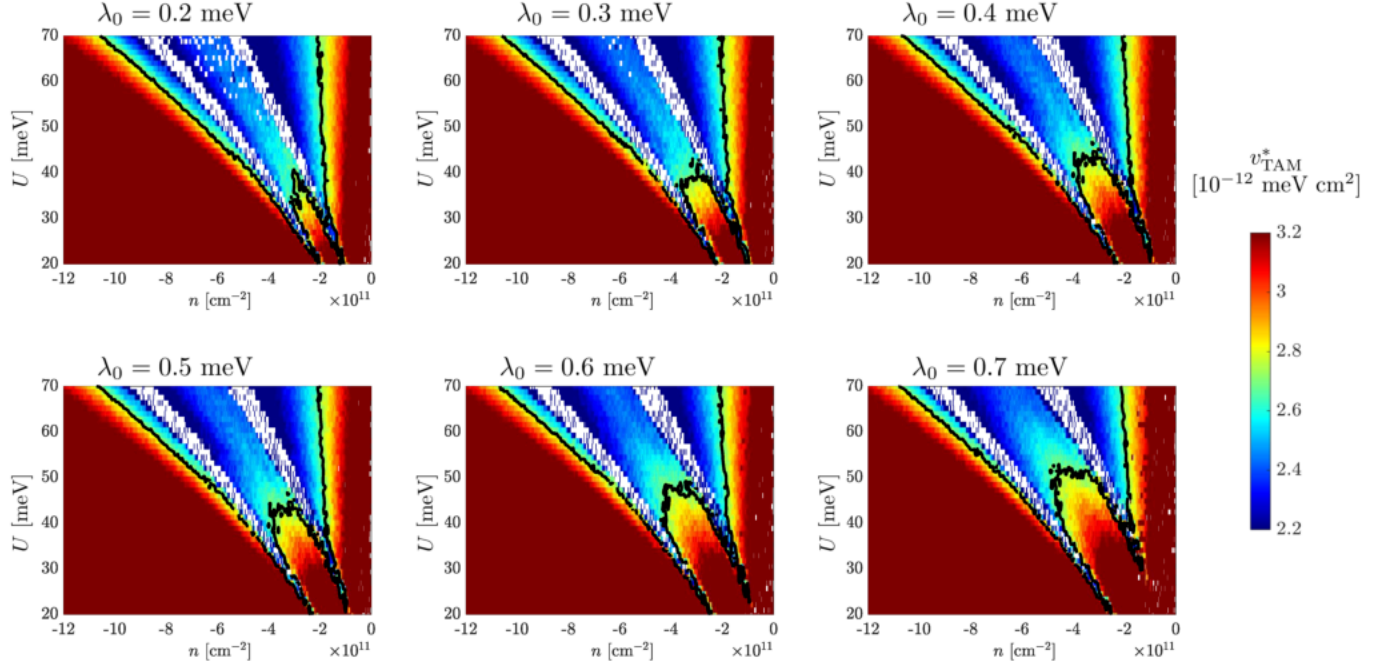
As the Ising spin-orbit increases and the bands become more separated (interactions only enhance this trend), the high-DOS regions in the two bands move further away from each other, as well. Consequently, it becomes exceedingly difficult to stabilize a regime where the DOS in the vicinity of the Fermi energy is high *in both bands*. A higher displacement field effectively enhances the high DOS region at energies just below the van Hove singularity, and thus make this simultaneous-high-DOS regime possible again.

As an illustration of this phenomenon, let us consider the effective Tolmachev-Anderson-Morel pseudo-potential

$$\mu_{\text{multi}}^* = \sqrt{\det \hat{g}_{\text{TAM}}(\omega^*)} = \sqrt{\det \left[(\hat{g}_{\text{initial}})^{-1} + \begin{pmatrix} \ell_1 & \\ & \ell_2 \end{pmatrix} \right]^{-1}}. \quad (30)$$

The interaction μ_{multi}^* can easily be verified to give the familiar TAM pseudo-potential in the single band case. Investigating this interaction is motivated by the fact that a superconducting transition is associated with a singularity of the \hat{g} matrix emerging at some energy scale. We point out that this singularity cannot occur without retardation, unless $|g_x| > g$ (this encompasses both attractive interactions $g < 0$, and cases where interband scattering dominates).

We plot the interaction strength μ_{multi}^* across the phase diagram for different values of the induced ISOC λ_0 in SI Fig. 7. Focusing our attention to within the blank white regions (those indicate



Supplementary Information Fig. 7 | ISOC dependence of the residual Coulomb repulsion μ_{multi}^* . Different panels correspond to calculations of Eq. (30) in the presence of different ISOC values, indicated on top of each panel. The first and last panels correspond to Fig. 2l in the main text. Note that the Ising splitting referred to in the main text is $\lambda_I = 2\lambda_0$, where λ_0 enters the model via Eq. (10). For emphasis, the black contour line marks the value $\mu_{\text{multi}}^* = 2.7 \times 10^{-12} \text{ meV cm}^2$. The blank white regions mark areas where the system develops valley-polarization, and superconductivity is thus suppressed. Here, we use the Thomas-Fermi screening approximation, where $g \approx \mathcal{N}_{\text{tot.}}(E_F)$, the total Fermi-level DOS, and $g_x = 0.5g$. Other parameters used in this plot: $\omega^* = 0.35 \text{ meV}$, $U_C = 1.4 \text{ eV nm}^2$, $J = U_V = 0.2 \text{ eV nm}^2$.

where two-fold degeneracy is broken within our simplified analysis), we discover the sought-after trend. Namely, the border of low μ_{multi}^* , and thus superconductivity threshold, moves to higher displacement fields when the ISOC is gradually enhanced. Again, this is due to the interband part of the interaction being most efficient when the DOS near the Fermi level is high in both bands at the same time.

7 Effect of Zeeman magnetic field

Let us discuss how Zeeman coupling of the in-plane magnetic field eventually impacts superconductivity itself.

Intravalley vs. Intervalley interactions Suppose the system we consider is characterized by two interaction scales: low-momentum scattering V_0 , and intervalley scattering V_Q . Originating

in Coulomb repulsion, which scales as $1/q$ (q is the magnitude of momentum scattered), one might assume $V_0 \gg V_Q$. This assumption relies on the Fermi momentum, $k_F \sim \sqrt{n/4} \sim 0.05 \text{ nm}^{-1}$, being much smaller than the intervalley momentum scale, $Q \approx 17 \text{ nm}^{-1}$. However, as was similarly argued in Refs. 57, 59, 60, k_F is not the relevant momentum here, as significant Thomas-Fermi screening takes place. The Thomas-Fermi momentum, $q_{TF} = 2\pi e^2 \mathcal{N}(\bar{\mu}) / \epsilon_r$ is of order $\mathcal{O}(10 \text{ nm}^{-1})$ (considering $\epsilon_r = 4$ for hBN and the relevant density ranges). It is thus entirely possible that V_0 and V_Q are comparable in strength, and both are of the order of magnitude of the inverse DOS at the Fermi level (as the Thomas-Fermi approximation suggests).

Considering the two bands or sectors are separated by spin-valley locking (mostly due to the induced Ising spin-orbit coupling), one identifies

$$g = V_0, \quad g_x = V_Q, \quad (31)$$

where we have assumed the scattering interactions preserve spin. However, if everything is kept the same, but now a canting angle $\theta \in [0, \frac{\pi}{2}]$ is introduced, such that $\theta = 0$ corresponds to the spin-valley locked phase, and $\theta = \pi/2$ corresponds to two sectors with completely opposite spin polarization within the plane, one finds

$$g = V_0 + V_Q \sin^2 \theta, \quad g_x = V_Q (1 - \sin^2 \theta). \quad (32)$$

Notice that for complete polarization g_x vanishes – this process now flips two spins and cannot be facilitated by the Coulomb interactions. Through this relation, and the self-consistent equation for superconducting T_c , *superconductivity becomes directly impacted by the canting angle*. Importantly, no pair-breaking within the different sectors occurs, and the Zeeman effect (which we will now demonstrate) only acts as a knob on the Cooper channel interaction strength.

Canting due to Zeeman in the presence of interactions Consider the mean-field free energy of a two-fold symmetric phase, with order parameter δn , in the presence of short-range repulsion U_C , ferromagnetic Hund's coupling J , and in-plane Zeeman energy V_Z ,

$$\begin{aligned} F(\delta n, \phi; n) = & 2E_{\text{kin}}\left(\frac{n + \delta n}{4}; \frac{n}{4}\right) + 2E_{\text{kin}}\left(\frac{n - \delta n}{4}; \frac{n}{4}\right) - \frac{U_C}{8}\delta n^2 \\ & - \lambda_0 s_z \tau_z - J \mathbf{S}_+ \cdot \mathbf{S}_- - V_Z S_x, \end{aligned} \quad (33)$$

where $E_{\text{kin}}(n_1; n_2)$ is the kinetic energy associated with maintaining the density n_1 instead of the paramagnetic density n_2 . In terms of the sector imbalance δn and canting angle θ , the magnetic part of the free energy is

$$\frac{F_{\text{mag}}}{\delta n} = -\lambda_0 \cos \theta + \frac{J\delta n}{4} \cos 2\theta - V_Z \sin \theta. \quad (34)$$

Let us approximate the dependence on δn and the canting angle θ as being roughly separable. In that case, we may minimize F_{mag} with respect to θ independently, arriving at the following transcendental equation for extracting θ ,

$$\lambda_0 \tan \theta - J\delta n \sin \theta = V_Z. \quad (35)$$

Notice that for $V_Z = 0$, one obtains $\theta = \cos^{-1} \frac{\min\{\lambda_0, J\delta n\}}{J\delta n}$, and one obtains full spin polarization ($\theta = \pi/2$) in the absence of spin-orbit coupling, as expected. Importantly, Eq. (35) clearly indicates the role of the majority-minority imbalance δn in determining the canting angle, as well as its susceptibility to a Zeeman term.

Comparison of different superconducting regions The mechanism described in detail above sheds light on the differing behaviors of various superconducting domes when subjected to an in-plane magnetic field.

The particularly relevant regions, considering the flavor occupation picture revealed by quantum oscillations, are SC_1 and the higher-hole-density part of SC_2 (the main dome). These two superconductors fit nicely within our framework of interband superconductivity, as they are comprised of two bands, minority and majority, each doubly degenerate. However, they have one important differentiating feature: the relevant interband polarization δn is significantly larger for SC_2 . The difference can already be gleaned from the experimental data, see Fig. 3c of the main text, where the quantum-oscillations feature corresponding to the majority band drops abruptly in the SC_1 region. This indicates a much smaller δn . The difference in δn is also readily apparent in our variational Hartree-Fock calculation, SI Fig. 8a, where it can be traced to the different DOS in the appropriate filling range.

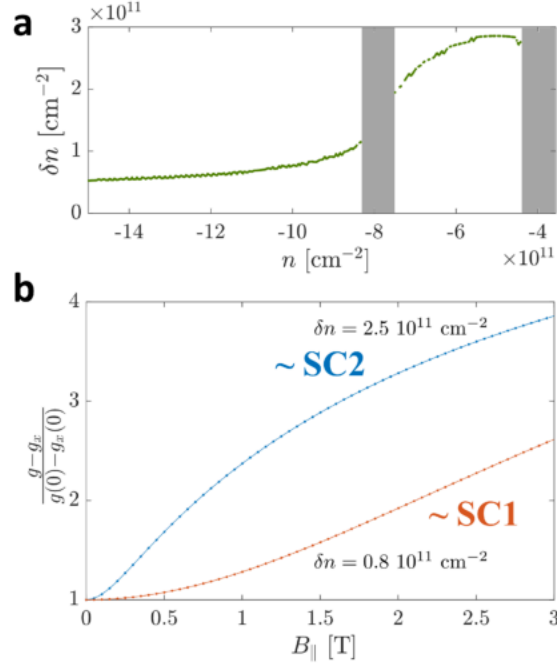
As such, we would expect [given Eqs. (35) and (32)] SC_2 to be much more sensitive to the in-plane field as compared to SC_1 . In SI Fig. 8b, we compare the relative strength of intraband and interband interactions as a function of magnetic field, for two representative values of δn . The canting angle is extracted via Eq. (35). As expected, the interactions corresponding to SC_2 are much more sensitive to the in-plane field. This is in complete agreement with the experimental data, as the Pauli-limit violation ratio (PVR) for SC_1 is ~ 18 , whereas for SC_2 it is noticeably lower, $PVR \sim 4$.

Remarkably, the trend in T_c in this part of SC_2 is well captured by our model calculations. For a large portion of this region, the critical temperature at small magnetic fields largely follows the relation

$$T_c(B_{\parallel}) - T_c(0) \approx -\alpha B_{\parallel}^2. \quad (36)$$

For example, in the data presented in Fig. 4 in the main text, the experimental value remains roughly constant in the left (lower density) part of the SC_2 dome, with $\alpha \approx 0.08$ Kelvin/Tesla². Our calculations, taking into account the magnetic field effects discussed in this section, are in good agreement both with the B_{\parallel}^2 trend, and with the numerical value of the prefactor α . This is demonstrated in SI Fig. 9, where the T_c behavior follows almost perfectly the behavior in Eq. (36) with the approximate experimental value.

To perform these calculations, we take as phenomenological input the shape of the Fermi surfaces observed in quantum oscillations. For the majority bands we take density per flavor in the range



Supplementary Information Fig. 8 | Understanding the discrepancy of in-plane magnetic field sensitivity between SC₁ and SC₂. **a**, Majority-minority band population imbalance δn as a function of density. Here we used $D = 0.8$ V/nm, and $\lambda_0 = 0.6$ meV. Gray rectangles mark regions where the two-fold degeneracy is broken within our variational Hartree-Fock analysis. The parameters we use to extract the normal state properties are identical to those in SI Fig. 7. **b**, Relative difference between the intraband (g) and interband g_x interactions as a function of magnetic field. We plot the trend for two representative values of δn (indicated in the panel), appropriate for the SC₁ (orange) and SC₂ regions. It is clear that repulsion grows more rapidly with magnetic field in the SC₂ region, alluding to the enhanced sensitivity of the corresponding superconductor. Here, $V_0 = 3.1$ eV nm², $V_Q = 2.2$ eV nm².

$[-3.35, -2.85] 10^{11} \text{ cm}^{-2}$, and for the minority bands $[-1.31, -1.2] 10^{11} \text{ cm}^{-2}$. Moreover, to account for the fact that the minority bands consist of two small pockets (instead of the expected three due to trigonal warping), we introduce a nematic order parameter which breaks the C_3 symmetry,

$$h_\tau(\mathbf{k}) \rightarrow h_\tau(\mathbf{k}) + \begin{pmatrix} & \Delta_{\text{nem}} \\ \Delta_{\text{nem}} & \end{pmatrix}, \quad (37)$$

and we used $\Delta_{\text{nem}} = -15 \text{ meV}$ to match the experimental observation in the desired density range. Other parameters used: $\omega^* = 0.8 \text{ meV}$, $V_0 = 3.1 \text{ eV nm}^2$, $V_Q = 2.2 \text{ eV nm}^2$, $J = 0.1 \text{ eV nm}^2$, $g_{\text{attraction}} = 0.41 \text{ eV nm}^2$, $U = 76 \text{ meV}$, $\lambda_0 = 0.6 \text{ meV}$.

Conversely, there is a marked change in behavior of SC_2 when moving closer to the charge neutrality point. Namely, T_c becomes much less sensitive to magnetic fields and the magnitude of the corresponding α prefactor becomes much smaller. Again, the quantum oscillation data provides us with important information. The data is consistent with flavor polarization developing within the minority bands themselves. Such polarization can be characterized by an order parameter $\delta n_{\text{minority}}$, such that in the absence of polarization $\delta n_{\text{minority}} = 0$, and when only one flavor (of the two minority ones) is occupied $\delta n_{\text{minority}} = n_{\text{minority}}$. Under the reasonable assumption of zero-momentum Cooper pairing, and considering the fact that the newly polarized flavors correspond to opposite valleys, one expects the minority bands to gradually decouple from the Cooper channel as this polarization increases.

To concretely illustrate this effect, we extract the appropriate Fermi energies in the minority sector, which correspond to a given $\delta n_{\text{minority}}$,

$$2 \int_0^{E_+} d\epsilon \mathcal{N}_2(\epsilon) = n_{\text{minority}} + \delta n_{\text{minority}}, \quad 2 \int_0^{E_-} d\epsilon \mathcal{N}_2(\epsilon) = n_{\text{minority}} - \delta n_{\text{minority}}. \quad (38)$$

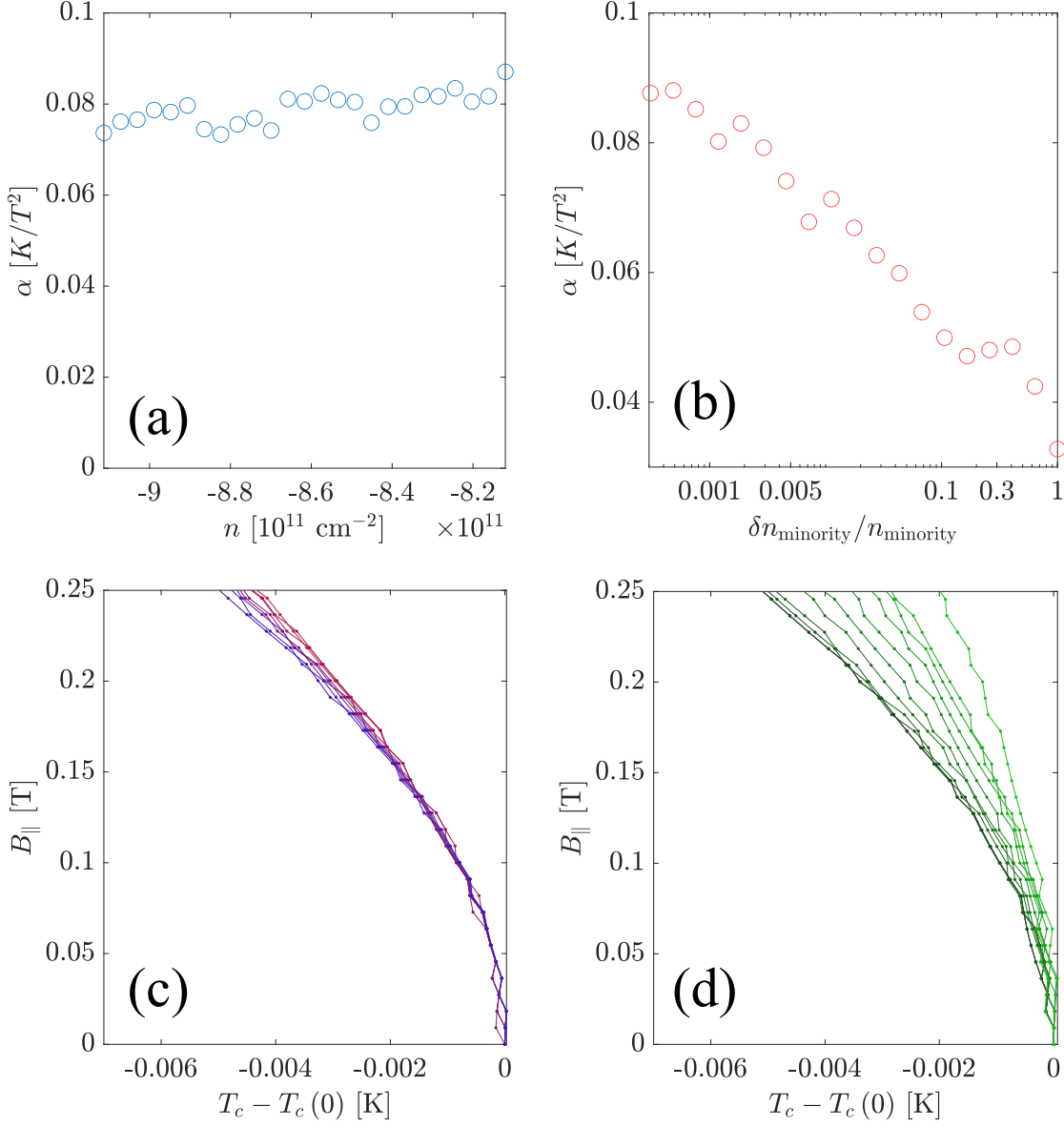
Taking $E_0 = E_\pm$ ($\delta n_{\text{minority}} = 0$), we define $\xi_\pm = E_\pm - E_0$. Thus, in the presence of this secondary polarization the appropriate Cooper integrals in the minority sector are altered,

$$\ell_2 = \left\{ \int_{\max\{\omega^*, \xi_+\}}^\infty + \int_{-\infty}^{\min\{-\omega^*, \xi_-\}} \right\} d\xi \frac{\mathcal{N}_2(\xi)}{|\xi|}, \quad (39)$$

$$\mathcal{D}_2 = \left\{ \int_{\xi_+}^{\max\{\omega^*, \xi_+\}} + \int_{\min\{-\omega^*, \xi_-\}}^{\xi_-} \right\} d\xi \mathcal{N}_2(\xi) \frac{\tanh \frac{\xi}{2T}}{\xi}. \quad (40)$$

We have implicitly assumed here that the relevant temperature regime, i.e., the vicinity of T_c , is much smaller than ξ_\pm/k_B . Notice that in the absence of polarization $\xi_+ = \xi_- = 0$, and we recover the previous expressions.

As we show in SI Fig. 9, we indeed recover the experimental trend. The underlying reason is that the magnetic field behavior we consider relates solely to the interband interactions in the Cooper



Supplementary Information Fig. 9 | In-plane field dependence of superconductivity in the SC₂ dome. **a**, The coefficient α extracted for a range of densities corresponding to the lower density region of SC₂, featuring an approximately constant coefficient. **b**, At the highest density of panel **a**, we introduce a polarization within the minority sector. The polarization gradually decouples the minority band from the Cooper channel, making the superconductor less sensitive to the magnetic field. **c,d**, Representative plots used to extract the fit parameter α in panels **a,b**, respectively. Details regarding the methodology and precise parameters used in the calculations can be found in the text of Sec. 7.

channel between majority and minority bands. Once one of these sectors stops “pulling its own weight”, eventually only an effective single-band (only majority) superconductor remains, and the magnetic field may only impact it through other effects we do not consider, e.g., an orbital effect (See also discussion of Sec. 8).

In this context, it is worth mentioning that in the normal state of SC_3 the quantum oscillation data is consistent with single band superconductivity, with significant time-reversal symmetry breaking in at least one of the sectors. As a result, our analysis would suggest reduced sensitivity to the $B_{||}$ for the same reason we just discussed. Remarkably, it appears indeed that SC_3 is the superconducting pocket which is most robust in the presence of the magnetic field, and has by far the largest Pauli limit violation in the measured devices.

In summary, the behavior of the different superconducting pockets as a response to an in-plane magnetic field strongly suggests that *interband interactions in the Cooper channel play a crucial role in BLG superconductivity*. Recognizing this prominent role, we may comment on the disparity between superconductivity in BLG with or without WSe_2 . Namely, in the former superconductivity is much stronger and more robust than the latter. In the two-fold polarized regime (majority and minority sectors are well separated in energy), the system is spin-polarized without WSe_2 due to intervalley Hund’s coupling. Thus, interband interactions are entirely absent in the Cooper channel due to spin conservation. Introduction of Ising spin orbit coupling “re-shuffles” the polarization cascade, and favors spin-valley locking as the two-fold phase even at moderate values of the induced spin orbit coupling. This “shifts” interaction strength from the intraband part of the coupling matrix to the interband part, Eq. (32). As we have demonstrated above, such a shift towards stronger interband interactions may have a *great positive impact on superconductivity*.

8 Analysis of SOC, orbital and Zeeman depairing mechanisms

We now discuss SOC, orbital, and Zeeman depairing mechanisms in Ising superconductors. We follow the treatment first developed in Ref. 48 to compute the response to a Zeeman field of non-centrosymmetric superconductors with Rashba SOC, later generalized in Refs. 49, 50 to systems with a coexistence of Ising and Rashba SOC. Parts of the discussion present in this supplement mirror our earlier analysis of Ref. 17. The analysis of this section complements the previous section, intending to provide contrast and further strengthen the interpretation above. Namely, the trends observed in the experiment as a function of in-plane magnetic field likely points to the prominence of majority-minority interband interactions.

We assume that as a result of flavor symmetry-breaking transition (cascade), the carriers in the parent states of SC_1 , SC_2 , and SC_3 occupy the relevant number of trigonal-warping pockets as discussed in the main text. Each trigonal-warping pocket we model as two electronic bands centered around trigonal-warping loci T that respectively originate from the K and K' valleys. We also assume that the selected pockets in the two valleys are time-reversed partners of each other to

allow for the formation of zero-momentum pairing naturally.

As mentioned in the text, we stress that the quantum oscillation data do not directly reveal nematicity but rather only inform about the number and relative sizes of Fermi pockets. If the Fermi pockets are not the trigonal warping pockets but rather some other Fermi pockets resulting from the interaction-driven reconstruction of the electronic spectrum, then the following modeling could still apply, provided that time reversal symmetry \mathcal{T} , which relates the two remaining small pockets is preserved. The specific relation between the effective Ising, Rashba, and orbital coupling, however, in such a case, would not be related to the microscopic parameters of the continuum model that we will derive in the following subsection.

Effective Hamiltonian in the trigonal warping pockets Here we derive an effective low-energy 2×2 Hamiltonian describing two SOC split bands at each trigonal warping loci. This Hamiltonian serves as a starting point for the following analysis as it allows us to connect microscopic model parameters (Ising, Rashba, Orbital, displacement field) with the low-energy theory. The purpose of this exercise is to provide analytic intuition about what energy and momentum scales in the problem control the depairing. Moreover, this procedure allows us to reduce the number of fitting parameters to just Rashba coupling as Ising SOC is determined experimentally, and orbital coupling is a property of the system.

The starting point of our analysis is the valley-dependent ($\tau = \pm 1$) Hamiltonian in spin, layer, and sublattice basis:

$$h_{full,\tau} = h_{0,\tau} + h_{I,\tau} + h_{R,\tau} + h_{orb,\tau} + h_Z, \quad (41)$$

where $h_{0,\tau} = s_0 \otimes h_\tau$ with h_τ given by Eq. (7) (we set $\Delta' = 0$ for simplicity) and describes the non-interacting Hamiltonian of bilayer graphene in the absence of SOC and magnetic field. We use the shorthand notation, s_0, s_x, s_y, s_z , for Pauli matrices in the spin space. The other entries in the above expression correspond to Ising SOC ($h_{I,\tau}$), Rashba SOC ($h_{R,\tau}$), orbital coupling ($h_{orb,\tau}$),

and Zeeman energy (h_Z). They are given by:

$$h_{I,\tau} = \frac{1}{2}\tau\lambda_I \left[s_z \otimes \begin{pmatrix} 1 & 0 & 0 & 0 \\ 0 & 1 & 0 & 0 \\ 0 & 0 & 0 & 0 \\ 0 & 0 & 0 & 0 \end{pmatrix} \right] \quad (42)$$

$$h_{R,\tau} = \frac{1}{2}\lambda_R \left[\tau s_y \otimes \begin{pmatrix} 0 & 1 & 0 & 0 \\ 1 & 0 & 0 & 0 \\ 0 & 0 & 0 & 0 \\ 0 & 0 & 0 & 0 \end{pmatrix} - s_x \otimes \begin{pmatrix} 0 & -i & 0 & 0 \\ i & 0 & 0 & 0 \\ 0 & 0 & 0 & 0 \\ 0 & 0 & 0 & 0 \end{pmatrix} \right] \quad (43)$$

$$h_Z = \mu_B B \left[(\cos \theta_B s_x + \sin \theta_B s_y) \otimes \begin{pmatrix} 1 & 0 & 0 & 0 \\ 0 & 1 & 0 & 0 \\ 0 & 0 & 1 & 0 \\ 0 & 0 & 0 & 1 \end{pmatrix} \right] \quad (44)$$

$$h_{orb,\tau} = \lambda_{orb} \left[\tau \sin \theta_B s_0 \otimes \begin{pmatrix} 0 & -1 & 0 & 0 \\ -1 & 0 & 0 & 0 \\ 0 & 0 & 0 & 1 \\ 0 & 0 & 1 & 0 \end{pmatrix} + \cos \theta_B \otimes \begin{pmatrix} 0 & -i & 0 & 0 \\ i & 0 & 0 & 0 \\ 0 & 0 & 0 & i \\ 0 & 0 & -i & 0 \end{pmatrix} \right] \quad (45)$$

In the above expressions, we explicitly write the sublattice and layer structure of the matrices to highlight that the Ising and Rashba SOC are induced only on one layer, which is in proximity to the TMD. The angle θ_B determines the direction of the in-plane magnetic field B with $\theta_B = 0$ corresponding to the x-direction in the continuum model. The orbital coupling enters via minimal coupling (See Ref. 61 for derivation). Its magnitude (See also Ref. 17):

$$\lambda_{orb} = \frac{v_0 e d}{2\hbar} = \frac{\sqrt{3}\gamma_0 a_0 e d}{4\hbar} \approx 0.14 \frac{\text{meV}}{\text{Tesla}}. \quad (46)$$

yields a stronger coupling than the spin Zeeman term h_Z with the Bohr magneton $\mu_B \sim 0.06$ meV/Tesla hinting at the role of orbital coupling in depairing. In the above Hamiltonian, in principle, all parameters are known or determined via experiment except λ_R .

We now follow the standard perturbation theory approach discussed, for example, in Ref. 34, 56 to arrive at a low-energy theory description of the trigonal warping pockets. The difference in our analysis compared to that of Ref. 34, 56 is that we keep both the trigonal warping term, v_3 , which is necessary to account for the three pockets as well as the displacement field U necessary to polarize charges to one side. Details and further discussion of the calculation are provided in Ref. 62. Carrying out the analysis, we arrive at an effective Hamiltonian $h_{eff,\tau}$ in each trigonal warping pocket (in the spin up and down basis):

$$h_{eff,\tau} = \tilde{h}_{0,\tau} + \tilde{h}_{I,\tau} + \tilde{h}_{R,\tau} + \tilde{h}_{orb,\tau} + \tilde{h}_Z, \quad (47)$$

where the individual terms are:

$$\tilde{h}_{0,\tau} \approx \epsilon^0(\mathbf{p})s_0 \quad (48)$$

$$\tilde{h}_{I,\tau} \approx \frac{1}{2}\tau\lambda_I s_z \quad (49)$$

$$\tilde{h}_{orb,\tau} \approx g_{orb}(\mathbf{p})s_0 \quad (50)$$

$$\tilde{h}_{R,\tau} \approx \frac{1}{2}(g_{R,x}(\mathbf{p})s_y - g_{R,y}(\mathbf{p})s_x) \quad (51)$$

$$\tilde{h}_Z \approx \mu_B B (\cos \theta_B s_x + \sin \theta_B s_y) . \quad (52)$$

Here we expanded around a trigonal warping center located along the x -axis focusing on leading order terms where $\gamma_0(v)$ and γ_1 were the large energy scales in the problem (Analogously to Ref. [34, 56](#)). The dispersion of other pockets can be analogously derived by the rotating location of the T . Momentum \mathbf{p} is measured with respect to the trigonal warping pocket center $T = T\hat{x}$:

$$T = \frac{\sqrt{\gamma_1^2 v_3^2 + 4U^2 v^2} + 3\gamma_1 v_3}{4v^2} \quad (53)$$

The parameters γ_1, v_3, v are the continuum model parameters defined in Eq. (7). U is the applied displacement field in units of energy difference across layers. As the displacement field grows, the trigonal warping centers move away from the K, K' points with Uv comparable to $\gamma_1 v_3$ for the relevant U for the experiment.

In the above equation the effective orbital coupling scale g_{orb} is

$$g_{orb} \approx \lambda_{orb} \frac{Uv(p_y \cos \theta_B - (\tau T + p_x) \sin \theta_B)}{\gamma_1^2} . \quad (54)$$

We see that as U increases, the role of orbital coupling becomes more pronounced. We also see that the effective orbital coupling has two characteristic momentum scales: (i) one sensitive to the filling of the small pockets (i.e., momentum \mathbf{p} dependent) and (ii) one set by the location of the trigonal warping pocket T . Depending on the orientation of the magnetic field (θ_B), the effective orbital coupling can change drastically, hinting at a potential sensitivity to in-plane field orientation.

Lastly the effective Rashba couplings $g_{R,x}(\mathbf{p})$ and $g_{R,y}(\mathbf{p})$ are given by:

$$g_{R,x}(\mathbf{p}) \approx \lambda_R \frac{p_y v (14\gamma_1 T v_3 + U^2)}{4\gamma_1^2 U} \quad (55)$$

$$g_{R,y}(\mathbf{p}) \approx \lambda_R \left[\frac{\tau T U v}{4\gamma_1^2} + \frac{p_x v (10\gamma_1 T v_3 + 3U^2)}{4\gamma_1^2 U} \right] . \quad (56)$$

Just as in the case of the effective orbital coupling, we find that there are two contributions to the effective Rashba coupling: (i) one set by the location of the trigonal warping pocket T and (ii) one

controlled by the doping of each pocket and hence momentum p_x, p_y . Physically, the two origins of the terms make sense: (i) controls the winding of the Rashba spin texture around the K, K' points, and (ii) controls the winding of the Rashba spin texture around the trigonal warping center. In the above expression, we focused on the leading order terms for typical numerical values (See Ref. 62 for further discussion).

Crucially, from the above result, we find that the effective Ising in each trigonal pocket is, to leading order, unmodified from the microscopic Ising value by the projection to each pocket. However, the effective orbital and Rashba contributions are different. Both orbital and Rashba contributions feature dependence on two characteristic momenta: (i) momentum location of the trigonal warping pocket from the K, K' (which is displacement field (U) dependent) and (ii) a momentum p measured with respect to each pocket center. Both terms are significant in determining the magnitude of the effective orbital and Rashba parameters.

Depairing analysis for $\lambda_I \ll E_F$ We now proceed to analyze the depairing mechanisms using the practical model of Eq. (47) as the normal state Hamiltonian. As mentioned before, we will follow the treatment first developed in Ref. 48 to compute the response to a Zeeman field of non-centrosymmetric superconductors with Rashba SOC, later generalized in Refs. 49, 50 to systems with a coexistence of Ising and Rashba SOC. The approach mirrors that carried out by us in Ref. 17, however here we focus on analytical understanding of the $T_C \rightarrow T_{C,0}$ limit (here $T_{C,0}$ is the depairing temperature in the absence of in-plane field). We will also use the results of the previous subsection to constrain the estimates with realistic microscopic parameters.

To connect to the previous work of Ref. 17, we further rewrite the normal-state Hamiltonian as

$$h_{eff,\tau}(\mathbf{p}) = \xi(\mathbf{p}) + \frac{1}{2}\tau\lambda_I s^z + \frac{1}{2}(\mathbf{s} \times \mathbf{g}_R(\mathbf{p})) \cdot \mathbf{z} + \mathbf{b} \cdot \mathbf{s} + (\mathbf{b} \times \mathbf{g}_{orb}(\mathbf{p})) \cdot \mathbf{z}, \quad (57)$$

On the right side $\xi(\mathbf{k})$ is the spin-orbit-free normal state band structure, which we linearize near the Fermi surface as $\xi(\mathbf{k}) \approx v_F(p - p_F)$ (p_F denotes the Fermi momentum measured from the center \mathbf{T} of the pocket). The next two terms incorporate Ising and Rashba SOC. Although the Rashba SOC, when projected to the trigonal warping pocket, is not isotropic with respect to the pocket center (as the pocket is not isotropic either), see Eq. (51), for simplicity of the analysis, we will approximate the Rashba as

$$\mathbf{g}_R(\mathbf{p}) \approx g_{R,0} + g_{R,1}(p_y, p_x) \quad g_{R,0} = \lambda_R \frac{\tau T U v}{4\gamma_1^2} \quad g_{R,1} = \lambda_R \frac{v(10\gamma_1 T v_3 + 3U^2)}{4\gamma_1^2 U}. \quad (58)$$

By comparison with Eq.(51), this overestimates the Rashba coupling, but for the purpose of this analysis, it is sufficient. For the orbital coupling, we focus on the in-plane field oriented along x -axis (we leave the discussion of in-plane direction dependence to the next section), giving

$$\mathbf{g}_{orb}(\mathbf{p}) = \lambda_{orb} \frac{U v p_y}{\gamma_1^2} (0, 1) \quad (59)$$

The term $\mathbf{b} \cdot \mathbf{s}$ is simply the Zeeman energy, which for an in-plane magnetic field B along x -axis takes the form $\mathbf{b} = (\mu_B B, 0, 0)$ with μ_B the Bohr magneton. We pause here to highlight that unlike the analysis of Ref. 17, here, in principle, there is only one undermined parameter λ_R with the remainder of the Hamiltonian known.

To analyze depairing, we then consider a local (momentum-independent) spin-singlet pairing term that gives rise to superconductivity with a critical temperature T_c^0 at zero magnetic field. In the presence of an in-plane magnetic field B , the superconductivity is weakened through a combination of spin and orbital effects, with $T_c < T_c^0$ given by the solution of a self-consistent gap equation linearized near the second-order transition at T_c where the pairing amplitude $\Delta \rightarrow 0$,^{48–50,63,64}

$$\ln \left(\frac{T_c}{T_c^0} \right) = \frac{T_c}{2} \sum_{\omega_n} \left(\left\langle \int d\xi_p \text{Tr} \{ s_y G_{0,\tau}(\mathbf{p}, i\omega_n) s_y G_{0,-\tau}^*(-\mathbf{k}, i\omega_n) \} \right\rangle_{\text{FS}} - \frac{\pi}{|\omega_n|} \right). \quad (60)$$

Here \sum_{ω_n} denotes a summation over Matsubara frequencies $i\omega_n$, $\langle \cdots \rangle_{\text{FS}}$ denotes a Fermi surface average and $\text{Tr}\{\cdots\}$ is a trace over spin Pauli matrices, and $G_{0,\tau}(\mathbf{p}, i\omega_n)$ is the normal-state Green's function given of the Hamiltonian from Eq.(57). The above equation can be further simplified (as done previously and in literature^{48–50}) to yield a non-linear equation connecting critical depairing magnetic field with the relevant temperature T_C . The pairing glue strength is parametrized here by the $T_{C,0}$ - the temperature without a magnetic field. We also note that in arriving at the above equation, we used the condition that chemical potential E_F is larger than any SOC scale. Thus, we also allow for an interband pairing in the above expression, however the pairing glue is not renormalized as discussed in the mechanism from the previous section. In the next subsection, we focus on the other limit of $E_F \ll \lambda_I$.

To make an explicit connection to the experimental fitting of $T_C = T_{C,0} - \alpha B^2$, we focus on the $T_C \rightarrow T_{C,0}$ limit of Eq.(60). In such cases, we can arrive at (See Ref. 62 for further discussion and details of the derivation) at a microscopic expression for α

$$\alpha = \alpha_0 + \alpha_{orb} \quad (61)$$

$$\alpha_0 \approx T_{C,0} \mu_B^2 \frac{2\lambda_I^2 + \tilde{g}_R^2}{(\lambda_I^2 + \tilde{g}_R^2)^2} \Phi(\rho) + \frac{\alpha_C \mu_B^2}{2k_B^2 T_{c0}} \frac{\tilde{g}_R^2}{\lambda_I^2 + \tilde{g}_R^2} \quad (62)$$

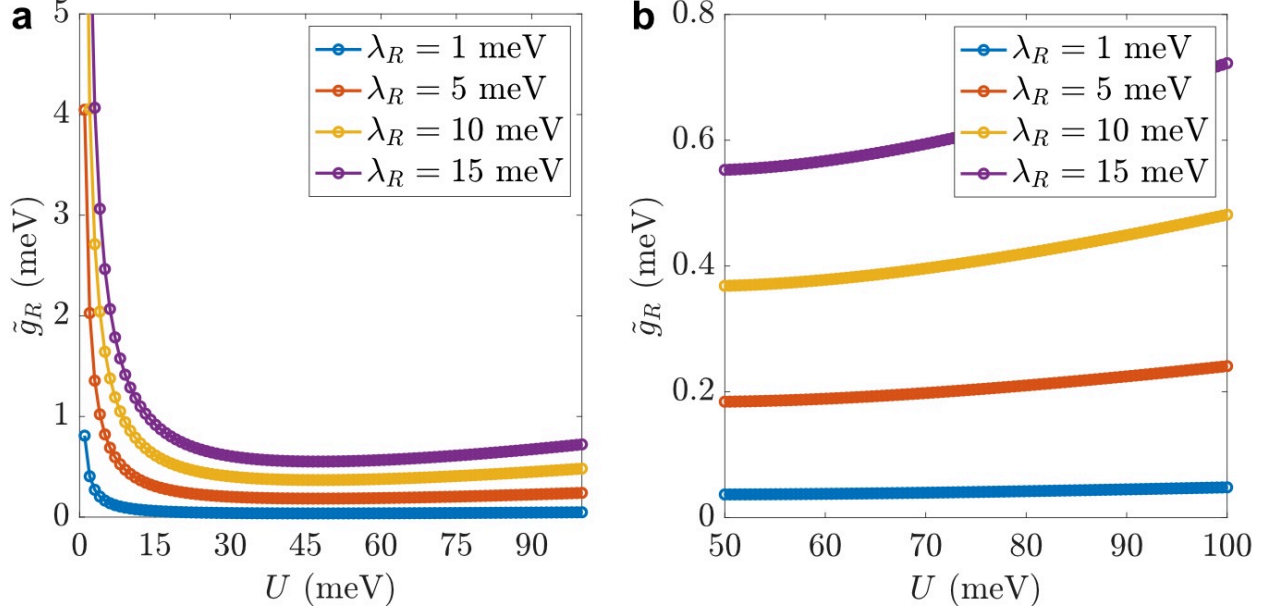
$$\alpha_{orb} \approx \alpha_C \frac{\tilde{g}_{orb}^2}{k_B^2 T_{c0}}, \quad \alpha_C = \frac{\Psi''(1/2)}{8\pi^2} \quad (63)$$

where we separated α into two parts orbital independent (α_0) and orbital dependent part (α_{orb}). Here, the effective Fermi surface averaged Rashba and orbital couplings are given by:

$$\tilde{g}_{orb} \approx \lambda_{orb} \frac{U v p_F}{\gamma_1^2}, \quad \tilde{g}_R \approx \lambda_R \frac{\tau T U v}{4\gamma_1^2} + \lambda_R \frac{v (10\gamma_1 T v_3 + 3U^2)}{4\gamma_1^2 U} p_F. \quad (64)$$

The special functions are defined as

$$\Phi(\rho) \equiv \frac{1}{2} \text{Re} \left[\Psi \left(\frac{1+i\rho}{2} \right) - \Psi \left(\frac{1}{2} \right) \right], \quad \rho = \frac{\sqrt{\lambda_I^2 + \tilde{g}_R^2}}{\pi k_B T_{C,0}} \quad (65)$$

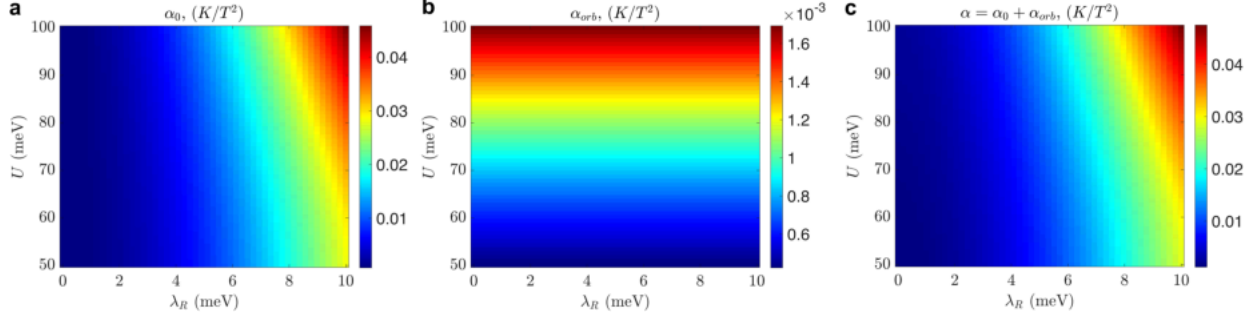


Supplementary Information Fig. 10 | Effective Rashba SOC in the trigonal warping pockets. **a,b,** The effective Rashba SOC in the trigonal warping pockets (see Eq. 64 and the related derivations).

and $\Psi(z)$, $\Psi''(z)$ is the DiGamma function and its second order derivative.

We briefly comment on the evolution of the effective Rashba coupling in SI Fig. 10. We find that for moderate values ($U > 15$ meV) of interlayer potential difference U , the microscopic Rashba induced by WSe₂ becomes strongly suppressed. To relate the value of U above which the effective Rashba is suppressed, we can refer to optical measurements of the BLG band gap, see Ref. 65. $U \sim 15$ meV corresponds to $D/\epsilon_0 \sim 0.2$ V/nm. This is in agreement with our experimental results where we find minimal effect of Rashba splitting at $D/\epsilon_0 \gtrsim 0.2$ V/nm.

Let us now analyze the consequences of the result in Eq.(61). As expected, when Ising SOC increases, α decreases, in line with the expected Ising superconductor behavior (i.e., superconductor becomes more resilient to depairing). Rashba SOC and orbital coupling contribute to depairing, with the contributions being additive. SI Fig. 11a-c shows plots of the two parts of the α coefficient separately (SI Fig. 11a,b) and combined (SI Fig. 11c) as a function of layer potential U and microscopic λ_R for $p_F \sim \sqrt{n/4} \sim 0.05$ nm⁻¹ at $T_{C,0} \approx 100$ mK and $\lambda_I = 1.5$ meV. We find that no realistic value of $\lambda_R < 10$ meV reproduces the experimental values of $\alpha \sim 0.1$ K/T² seen in SC₂ (we are about an order of magnitude too small). This conclusion also holds if the direction of the B_{\parallel} were rotated to increase the orbital coupling, c.f. Eq.(54). For the SC₁ case however where the superconductor is more robust to depairing with the experimental $\alpha \lesssim 0.01$ K/T² the theoretically predicted α is in agreement for reasonable $\lambda_R < 2$ meV values.



Supplementary Information Fig. 11 | Coefficient α in $T_C = T_{C,0} - \alpha B^2$ in the $E_F \gg \lambda_I$ limit. Dependence of the coefficients α_0 (a), α_{orb} (b), and $\alpha = \alpha_0 + \alpha_{orb}$ (c) from Eq.(61) on layer potential U and Rashba coupling λ_R . Here we use $p_F \sim \sqrt{n}/4 \sim 0.05 \text{ nm}^{-1}$ at $T_{C,0} \approx 100 \text{ mK}$ and $\lambda_I = 1.5 \text{ meV}$.

To phrase it differently, using realistic microscopic SOC and orbital coupling values is insufficient to account for the suppression of superconductivity with an in-plane field in the SC_2 phase. This apparent robustness is a consequence of approximating the intra and interband pairing as having constant magnitude. As argued in Sec. 7, however, the interband and intraband interactions are modified in the presence of a magnetic field due to canting effects, thus reducing the robustness to the in-plane field and increasing α .

Depairing analysis for $\lambda_I \gg E_F$ In the analysis of the previous section, we were working in the conventional limit used for the Ising superconductors of E_F being the largest energy scale in the problem. As a result, the microscopic dispersion dependence ξ_p effectively dropped out of the calculation. However, given that in the large U limit, the trigonal warping pockets become flat promoting interactions, it is also insightful to consider the other limit of $\lambda_I \gg E_F$. In this limit, we will focus solely on an intraband pairing between the small trigonal warping pockets (the minority carriers) in each valley, as the interband pairing should be subleading.

We begin by writing the linearized intraband gap equation for the pairing temperature

$$\frac{2}{g} = \int \frac{d^2 \mathbf{p}}{(2\pi)^2} \frac{\tanh\left(\frac{\epsilon_{\tau, \mathbf{p}}}{2k_B T_C}\right) + \tanh\left(\frac{\epsilon_{-\tau, -\mathbf{p}}}{2k_B T_C}\right)}{\epsilon_{\tau, \mathbf{p}} + \epsilon_{-\tau, -\mathbf{p}}}, \quad (66)$$

where $\epsilon_{\tau, \mathbf{p}} = \epsilon_{\tau, \mathbf{p}}^0 + s_{\tau, \mathbf{p}}$ is the dispersion of carriers. Here $\epsilon_{\tau, \mathbf{p}}^0$ is the dispersion of the carriers in the absence of SOC and magnetic field (See Eq.(47)) and the $s_{\tau, \mathbf{p}}$ is the SOC, orbital and Zeeman field dependent part. Crucially $\epsilon_{\tau, \mathbf{p}}^0 = \epsilon_{-\tau, -\mathbf{p}}^0$, but $s_{\tau, \mathbf{p}} \neq s_{-\tau, -\mathbf{p}}$ giving rise to depairing.

To eliminate the pairing constant g we can use the analogous $T_{C,0}$ expression

$$\frac{2}{g} = \int \frac{d^2 \mathbf{p}}{(2\pi)^2} \frac{\tanh\left(\frac{\tilde{\epsilon}_{\tau, \mathbf{p}}}{2k_B T_{C,0}}\right) + \tanh\left(\frac{\tilde{\epsilon}_{-\tau, -\mathbf{p}}}{2k_B T_{C,0}}\right)}{\tilde{\epsilon}_{\tau, \mathbf{p}} + \tilde{\epsilon}_{-\tau, -\mathbf{p}}}, \quad (67)$$

where $\tilde{\epsilon}_{-\tau,-\mathbf{p}}$ is the dispersion $\epsilon_{\tau,\mathbf{p}} = \epsilon_{\tau,\mathbf{p}}^0 + s_{\tau,\mathbf{p}}$ evaluated at $B \rightarrow 0$. Using Eq.(66) and Eq.(67), eliminated g and expanding near $T_C \rightarrow T_{C,0}$ we arrive at the desired form

$$T_C = T_{C,0} - \alpha B^2, \quad (68)$$

where

$$\alpha \approx T_{C,0} \frac{F}{G}, \quad G \approx \int \frac{d^2\mathbf{p}}{(2\pi)^2} \frac{1}{2k_B T_{C,0}} \text{sech}^2 \left(\frac{2\epsilon_{+,\mathbf{p}}^0 + \lambda_I}{4k_B T_{C,0}} \right) \quad (69)$$

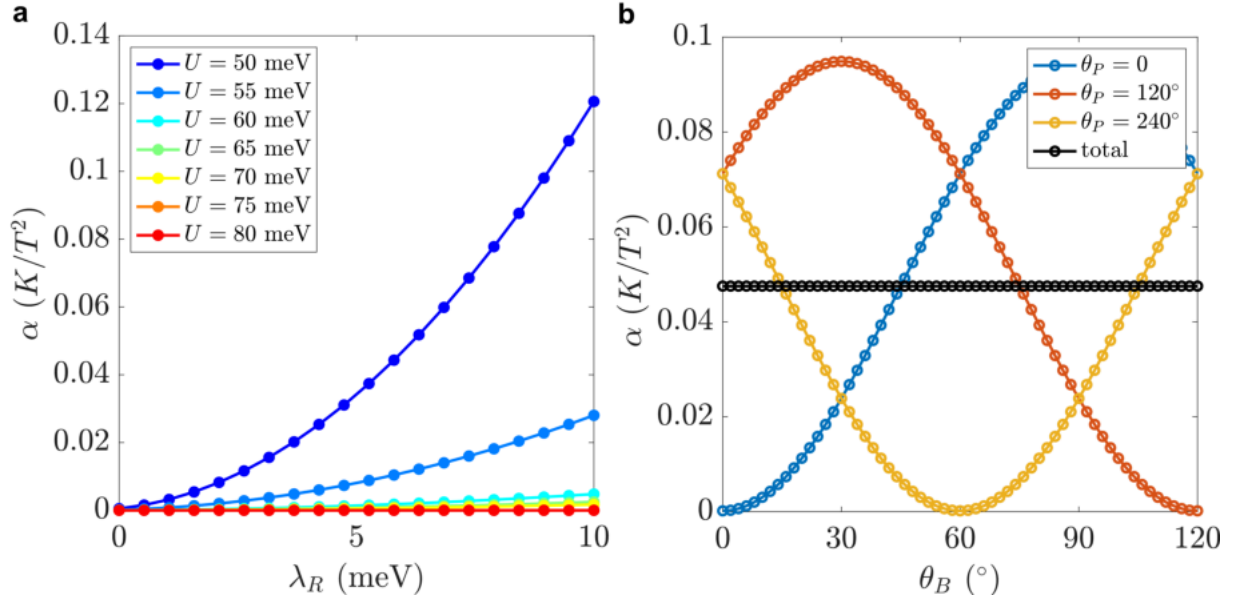
and the function F is given by a series expansion of

$$F \approx \frac{1}{B^2} \int \frac{d^2\mathbf{p}}{(2\pi)^2} \frac{\tanh\left(\frac{\tilde{\epsilon}_{\tau,\mathbf{p}}}{2k_B T_{C,0}}\right) + \tanh\left(\frac{\tilde{\epsilon}_{-\tau,-\mathbf{p}}}{2k_B T_{C,0}}\right)}{\tilde{\epsilon}_{\tau,\mathbf{p}} + \tilde{\epsilon}_{-\tau,-\mathbf{p}}} - \frac{\tanh\left(\frac{\epsilon_{\tau,\mathbf{p}}}{2k_B T_{C,0}}\right) + \tanh\left(\frac{\epsilon_{-\tau,-\mathbf{p}}}{2k_B T_{C,0}}\right)}{\epsilon_{\tau,\mathbf{p}} + \epsilon_{-\tau,-\mathbf{p}}} \quad (70)$$

in powers of magnetic field B , the leading order of which is independent of B as required. The perturbation can be evaluated in a closed form; however, the resulting expression is not particularly transparent.

Let us now analyze the consequences of the result in Eq.(69) mirroring the analysis of the previous section. SI Fig. 12a shows a plot of numerically determined α coefficient from Eq.(69) as a function of layer potential U and microscopic λ_R for $p_F \sim \sqrt{n/4} \sim 0.05 \text{ nm}^{-1}$ at $T_{C,0} \approx 100 \text{ mK}$ and $\lambda_I = 1.5 \text{ meV}$. We again see that no realistic value of $\lambda_R \lesssim 10 \text{ meV}$ reproduces the experimental values of $\alpha \sim 0.1 \text{ K}/T^2$ seen in SC_2 for large U values. This again supports our conclusions of the previous depairing analysis and points towards the mechanism of Sec.7 as controlling the resilience to the magnetic field of the SC_2 .

In SI Fig. 12b, we fix $\lambda_R = 2 \text{ meV}$ and $U = 65 \text{ meV}$ and vary the orientation of in-plane magnetic field θ_B . The three curves ($\theta_B = 0, 120^\circ, 240^\circ$) correspond to the expected depairing if only one of the three trigonal warping pockets is occupied. When all three pockets are occupied (as in SC_1), there is no dependence on an in-plane B field direction in line with results of Ref. 18. While the precise value of α is controlled by $T_{C,0}, \lambda_R$ and U , we notice that if only one pocket were occupied, then one expects a significant variation in T_C as a function of in-plane B field direction. This contrasts the experiment; see Extended Data Fig. 17, thus suggesting that perhaps a strict “flocking” model is not applicable and the Fermi surface could reconstruct itself in response to the applied B field to minimize depairing - a proposal that can be verified in future self-consistent HF works that allow for nematicity.



Supplementary Information Fig. 12 | Coefficient α in $T_C = T_{C,0} - \alpha B^2$ in the $\lambda_I \gg E_F$ limit. **a**, Dependence of the coefficient α from Eq.(69) for various potentials U and Rashba coupling λ_R . Here we use $p_F \sim \sqrt{n/4} \sim 0.05 \text{ nm}^{-1}$ at $T_{C,0} \approx 100 \text{ mK}$ and $\lambda_I = 1.5 \text{ meV}$. **b**, Dependence of α on an in-plane B field direction θ_B . Here $U = 65 \text{ meV}$, $\lambda_R = 2 \text{ meV}$. $\theta_P = 0, 120^\circ, 240^\circ$ label the three trigonal warping pockets. See also the discussion in the text.